March 2017

Topography measurements using an airborne Ka-band FMCW Interferometric Synthetic Aperture Radar

Kan Fu
University of Massachusetts - Amherst

TOPOGRAPHY MEASUREMENTS USING AN AIRBORNE KA-BAND FMCW INTERFEROMETRIC SYNTHETIC APERTURE RADAR

A Dissertation Presented

by

KAN FU

Submitted to the Graduate School of the
University of Massachusetts Amherst in partial fulfillment
of the requirements for the degree of

DOCTOR OF PHILOSOPHY

February 2017

Electrical and Computer Engineering

TOPOGRAPHY MEASUREMENTS USING AN AIRBORNE KA-BAND FMCW INTERFEROMETRIC SYNTHETIC APERTURE RADAR

A Dissertation Presented

by

KAN FU

Approved as to style and content by:

Paul Siqueira, Chair

Stephen Frasier, Member

Patrick A. Kelly, Member

Thomas L. Millette, Member

K. Sigfrid Yngvesson, Member

Christopher V. Hollot, Department Head
Electrical and Computer Engineering

To my parents, Taiping Fu and Mulan Pan, and to my wife, Keying An, for their constant support through these years.

ACKNOWLEDGEMENTS

Firstly, I would like to give my full gratitude to my advisor Professor Paul Siqueira. Without his support and encouragement, I will not be able to have the opportunity to get into the field of microwave remote sensing. The completion of this dissertation will never happen without his professional guidance. His broad knowledge in microwave remote sensing and radar systems shows me the right direction during the research work of this dissertation.

I want to thank the members of the committee, Professor Yngvesson, Professor Frasier, Professor Kelly and Professor Millette, for their time and effort in reading the dissertation and the suggestions they gave. They are the best teachers I have met and I have learned from a lot from them.

I would like to thank my colleagues in the Microwave Remote Sensing Laboratory (MiRSL). I received a lot of help from them in the lab. It is my great pleasure to have worked with them. Dr. Edin Insanic taught me a lot in the high-frequency PCB design, even before I joined MiRSL. I would like to thank Rockwell Schrock, for his excellent work in the system integration and data collection. I am thankful to the many discussions with Xingjian Chen, on the thermal characterization and radar systems, discussions with Gerald Ruiz Carregal and Dustin Lagoy on the FMCW SAR processing. I also want to thank our Graduate Program Manager, Barbara Barnett, for her help with all the paperwork. Special thanks to our lab manager Tom Hartley, for his support for my needs of equipments.

Finally, I would like to thank my parents and my wife, for their continuous support during so many years.

ABSTRACT

TOPOGRAPHY MEASUREMENTS USING AN AIRBORNE KA-BAND FMCW INTERFEROMETRIC SYNTHETIC APERTURE RADAR

FEBRUARY 2017

KAN FU

B.Sc., UNIVERSITY OF SCIENCE AND TECHNOLOGY OF CHINA

M.Sc., UNIVERSITY OF MASSACHUSETTS AMHERST

Ph.D., UNIVERSITY OF MASSACHUSETTS AMHERST

Directed by: Professor Paul Siqueira

Radar interferometry at millimeter-wave frequencies has the ability of topography measurement of different types of terrain, such as water surfaces and tree canopies. A Ka-band interferometric radar was mounted on an airborne platform, and flown over the Connecticut river region in western Massachusetts near Amherst on June 11, 2012. More than 20 Gigabytes of raw data was recorded. This dissertation outline presents the results of the data processing, which includes (1) the estimation and removal of the embedded high frequency phase error in the raw data; (2) the synthetic aperture processing; (3) the interferometric processing. The digital elevation model (DEM) has been generated based on an external DEM from MassGIS. The accuracy of the topography measurement can be affected by many factors, such as the de-correlation between channels and the residual phase error. This dissertation outline proposes to evaluate the accuracy of the topography measurement by quantifying each error source. Specifically, the performance of the phase error estimator

and the Doppler centroid estimation will be analyzed, and an algorithm which estimates the attitudes of the airborne platform will be developed.

TABLE OF CONTENTS

LIST OF TABLES

Table **Page**

LIST OF FIGURES

Figure **Page**

CHAPTER 1

INTRODUCTION

1.1 Background and Motivation

For many decades, radar has been widely used in earth science and remote sensing research as a high resolution imaging system[1],[2], which provides global coverage of the earth surfaces, such as oceans, sea ice and forests. In addition to the high resolution map of the natural surface, a three-dimensional model of the terrain given by an elevation map has found many applications in different research areas. For example, a digital elevation model (DEM) and bedrock elevation data for the polar ice is necessary for the study of ice volume change. There are different technologies to generate the terrain topography maps, such as radar altimetry [3],[4], photogrammetry [5], radar interferometry [6],[7], and many others.

Depending on the application and instrument, the radar can be installed on either an airborne or a space-borne platform. In both cases, the resolution in the along-track direction can be improved with respect to the resolution determined by antenna beamwidth through aperture synthesis, thus creating a Synthetic Aperture Radar (SAR). A SAR is a combination of a radar hardware platform and corresponding signal processing methods, and was invented first by Carl A. Wiley at Goodyear Aircraft Company, and independently by Sherwin and others at the University of Illinois' Control Systems Laboratory in the 1950's [8]. It has been widely used since then as a common tool in high resolution radar imaging and has become a standard technology in remote sensing. The first SAR satellite system was the SEASAT mission[9],[10] of NASA/JPL. It was launched on June 27, 1978. During its 106-

day lifetime, SEASAT collected more information about the oceans than had been acquired in the previous 100 years of shipboard research[11].

Different wavelengths have been used for SAR systems in a variety of applications, such as L-band, C-band and X-band, where the signal wavelengths are 24, 6 and 3 cm respectively. Generally, SAR working at longer wavelengths can penetrate through objects and collect radar backscatter echoes beneath surfaces with low dielectric contants. For instance, in forests where most visible light reflects from a forest canopy, lower frequency signals such as L-band, will penetrate and be scattered from the branches, trunks and ground. When a synthetic aperture radar is combined with interferometry it is known as InSAR.

The idea of a "synthetic interferometer radar" was proposed first by Graham in 1974 for topographic mapping [12]. Many InSAR systems have been employed either in airborne or spaceborne platforms. However, there are only a few demonstrated InSAR systems working at millimeter wave range, one such system being Ka-band (35 GHz or $\lambda = 8.6$ mm, λ is the wavelength)[13][14][15]. All the radar system in [13][14][15] are pulsed radar system.

Typically, two receiving antennas are employed to collect the radar echoes backscattered from ground objects as illustrated in Figure 1.1. In the example shown in the figure, the two receiving antennas can be two different antennas mounted on one aircraft and collect radar echoes in the same flight track. This configuration is called single-pass interferometry, as shown in Figure 1.1(b). If there is only one receiving antenna, which collects radar echoes in two time-separated flight tracks, then it is called repeat-pass interferometry, as shown in Figure 1.1(a). With just one receiving antenna, the radar data are measured as a function of range, also known as the slant range. By adding a second receiving antenna, both range and look angle of ground scatterers can be determined. Hence, through radar interferometry, the location of the scatterer relative to the radar can be accurately determined. Provided with the

position information of the radar platform with respect to a reference ground level, the location of the scatterer relative to the radar can be translated to its location relative to that reference level. This result is the topography, measured by the interferometer.

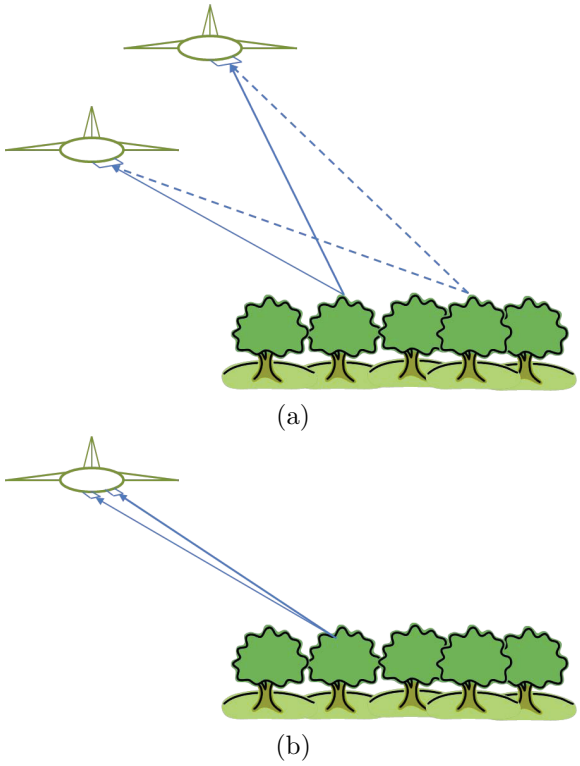

Figure 1.1: An illustration of radar interferometry: (a) Repeat-pass radar interferometry. (b) Single-pass radar interferometry.

Targeted for launching in the year of 2021, NASA's Surface Water and Ocean Topography (SWOT) mission will be a spaceborne Ka-band radar interferometer (KaRIn), illustrated in Figure 1.2[16]. The mission aims to determine ocean and surface water topography with high spatial resolution. The scientific objects of SWOT mission cover the hydrology and oceanography. It will provide a global inventory of all terrestrial water bodies whose surface area exceeds 250 meters by 250 meters (lakes, reservoirs, wetlands) and rivers whose width exceeds 100 meters (rivers), and charac-

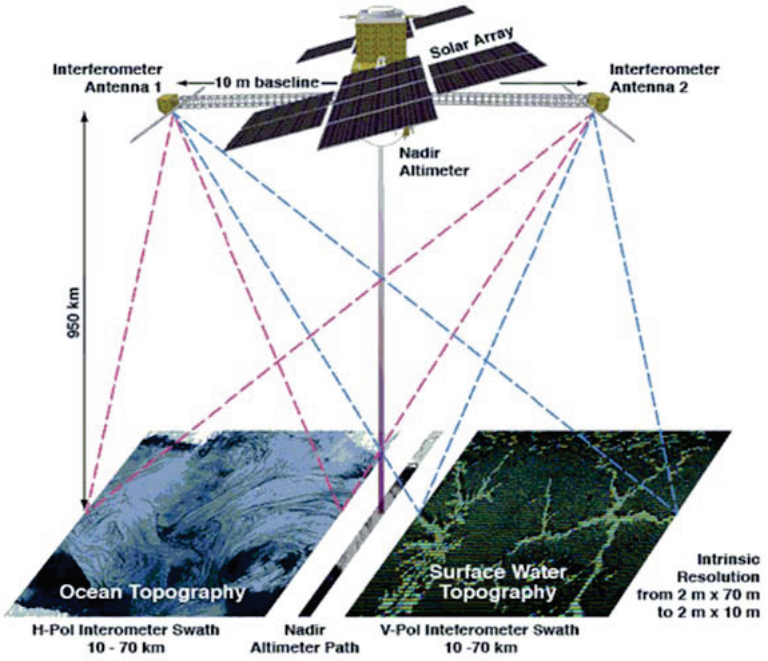

Figure 1.2: An illustration of the SWOT single-pass Ka-band radar interferometer concept.

terize the ocean mesoscale and sub-mesoscale circulation at spatial resolutions of 15 kilometers and greater[16].

Under the Advanced Component Technology (ACT) program of NASA, the University of Massachusetts was awarded a grant for the design, development and testing of a Ka-band two-channel downconverter for use in spaceborne interferometric radar applications. Additionally, a transmitter, antennas, signal generation and data acquisition units are being designed to support the application of this downconverter in the field as part of a working interferometric radar. A Ka-band InSAR system has been implemented with the radar system installed on an airplane.

The aim of this dissertation will be the terrain topographic measurement using radar interferometry. In this dissertation, it will concentrate on the signal processing and the factors which contributes to the error of the topographic measurement using the Ka-band InSAR system. Particularly the motion compensation algorithm for the

airborne radar will be investigated and the potential of the topographic measurement of a Ka-band interferometric radar platform will be evaluated.

1.2 Outline of the Dissertation

In this dissertation, the potential of terrain topography measurement of a Ka-band airborne InSAR system, which was designed and developed at the Microwave Remote Sensing Laboratory (MiRSL), will be demonstrated through the processing of SAR and InSAR data. Motion effects and phase nonlinearities will be analyzed and processed. Various maps of areas of western Massachusetts, including multi-looking SAR, digital surface map (DSM) and differential elevation map, are generated. The error sources will be evaluated for these map products. The dissertation is organized as follows.

Chapter 2 provides a brief overview of the radar techniques being used in this dissertation. It introduces the general principles of the synthetic aperture radar, the FMCW radar and the interferometric radar. Chapter 3 presents an overview of the radar system, including the antennas, RF frontend, digital baseband and the GPS and IMU subsystem. The performance of the transmitter and receiver are characterized and listed. Chapter 4 gives a detailed description of the data processing procedures. A frequency domain approach was utilized through the processing. In addition to the standard steps of signal processing, an anomaly existing in the radar raw data was successfully removed by using a phase error model. Chapter 5 investigates the motion effects and the compensation methods for an airborne radar. The angular motion effects has been analyzed and its compensation method is proposed. Chapter 6 presents the interferometric processing of the two-channel Ka-band synthetic aperture radar data. The results of differential height and digital elevation map (DEM) are presented. The conclusion and future work is presented in Chapter 7. In the

Appendix, the error sources of the topographic measurement are analyzed for different types of decorrelation.

CHAPTER 2

TECHNICAL OVERVIEW

2.1 Synthetic Aperture Radar Principle

Synthetic literally means something that is man-made, and is used here to indicate the creation of a large aperture antenna by assembling low-resolution smaller aperture observations to make a high-resolution image. For a real apertured radar, its resolution in the plane perpendicular to the radar-beam direction is determined by its antenna beamwidth and the slant range of the scatterer. The minimum 3-dB beamwidth of a real aperture antenna can be found using the Rayleigh criterion

$$\theta = 1.22\frac{\lambda}{D}, \tag{2.1}$$

which states that the beamwidth if proportional to the wavelength, λ, of the transmitted signal and D, the size of the antenna aperture. For a uniformly illuminated circular aperture, the 3-dB beamwidth is slightly less than the value given by Rayleigh criterion

$$\theta_{3dB} = 1.08\frac{\lambda}{D}. \tag{2.2}$$

For example, the Ka-band (35 GHz) antenna used in this work of this dissertation has a dimension of 0.5 meter in the azimuth direction, hence its 3-dB beamwidth θ_{3dB} in the azimuth direction given by (2.2) is 0.98°. For the data-taken, during airborne flights of this radar where the altitude is approximately 700 meters, the corresponding spatial resolution in the azimuth direction at a look angle of $\theta = 45°$, is given by $\frac{H}{cos\theta}\theta_{3dB} = 25$ meters.

Following the above example, the azimuth resolution for a real apertured radar working from a relatively high altitude, can be several hundred meters for the airborne case, and many kilometers for the spaceborne case. Although the azimuth resolution could be improved by increasing the antenna size, there are many practical constraints on antenna size due to the platform geometry. However, the radar azimuth resolution can be increased by a large factor through the process of focusing, implemented by the signal processing approach of matched filtering. The method synthesizes an antenna aperture by using the series of radar echoes received from different positions along its flight path as an effectively larger aperture. The phase of each pulse is a function of the slant range to the scatterers, hence these pulses from the single real apertured radar can be viewed as received echoes form a larger "synthetic aperture", as shown in Figure 2.1, in which R_0 is the closest approach from the radar to a scatterer P. This diagram simplifies the scenario by showing only one scatterer.

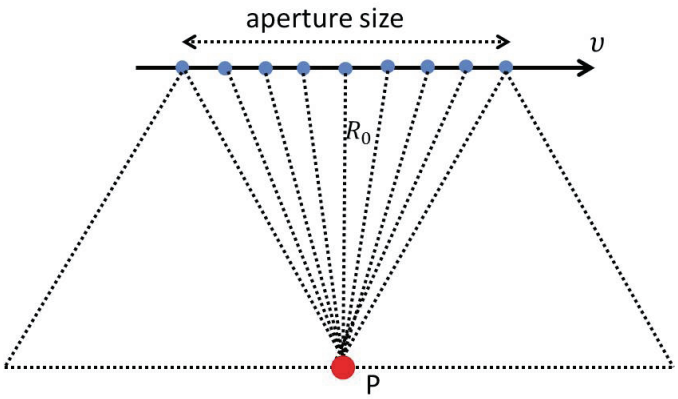

Figure 2.1: The synthetic aperture concept. Point P in red color represents a point scatterer on the ground. The radar platform is moving with a velocity of v. Green dots along the straight line are the positions where the radar transmits a pulse. All those positions from which the radar can illuminate the scatterer form a synthetic aperture. R_0 is the minimum distance between radar and the scatterer.

2.1.1 Matched Filter and Pulse Compression

It can be shown that a matched filter maximizes the output signal-to-noise ratio (SNR) when the noise is additive [17]. Further, when the noise is white, the time-domain impulse response of the matched filter is given by

$$h(t) = \alpha x^*(\tau - t), \ -\tau \leq t \leq 0, \tag{2.3}$$

where τ is the pulse width, $x(t)$ is the input signal, and α is a scalar related to the scatterer's radar reflectivity. The expression in (2.3) is a time-reversed replica of the input signal. If the input signal is frequency or phase modulated, the response of the matched filter $y(t)$ will have a narrow main-lobe whose width is inversely proportional to the input waveform bandwidth, BW, which determines the resolution. Hence, the output of the matched filter is

$$y(t) = \int_0^\tau x(s)h(t-s)ds = \int_0^\tau x(s)x^*(s-t)ds \ . \tag{2.4}$$

A common waveform for the input signal is the linear frequency modulated (LFM) pulse, which has the form

$$x(t) = e^{j(\omega_0 t + \frac{\beta}{2}t^2 + \phi_0)}, \ 0 \leq t \leq \tau \ . \tag{2.5}$$

The output of the matched filter is then obtained by substituting (2.5) into (2.4),

$$\begin{aligned} y(t) &= \int_0^\tau e^{j(\omega_0 s + \frac{\beta}{2}s^2 + \phi_0)} e^{-j(\omega_0(t-s) + \frac{\beta}{2}(t-s)^2 + \phi_0)} ds \\ &= \frac{\sin\left(\frac{\beta}{2}(t-\tau)(\tau - |t-\tau|)\right)}{\frac{\beta}{2}(t-\tau)} e^{j(t-\tau)(\omega_0 + \frac{\beta}{2}\tau)} \ . \end{aligned} \tag{2.6}$$

The normalized magnitude of $y(t)$, which is a sinc function, is plotted in Figure 2.2. The compressed pulse has a main-lobe and a number of sidelobes on either side. The

3-dB width of the main-lobe which defines the resolution is given by $\frac{1}{BW}$. For a 100 MHz bandwidth signal, the width in time is 0.01 μs.

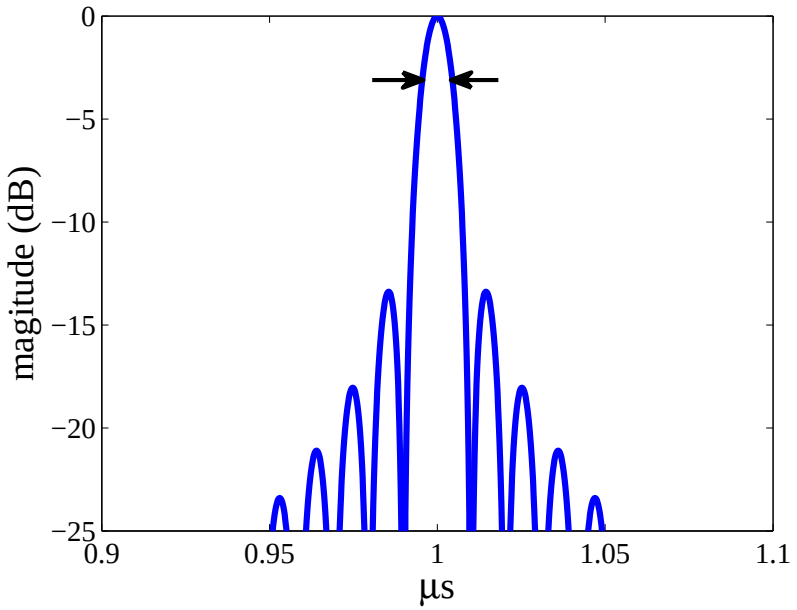

Figure 2.2: The matched filter response for a bandwidth $BW = 100\,\text{MHz}$, $\tau = 1\,\mu s$ linearly frequency modulated pulse. The main-lobe 3-dB width as indicated by the arrows is about $0.01\,\mu s$.

If we consider the signal received by the radar from a point scatterer at some distance from the radar is as depicted in Figure 2.1, a time series of observations from the radar is as if the radar transmits a simple sinusoidal signal and records the magnitude and phase of the radar echo, then moves on to the next position. The aperture size is determined by the azimuth antenna pattern. According to the radar equation, the magnitude of the radar echoes depends on radar antenna pattern and the distance from radar to the ground scatterer. If the distance between the radar and the scatterer is large, the variation of magnitudes can be ignored for simplicity, and under the assumption that the change in range affects only the signal phase and not its magnitude. Then the received signal only depends on its phase, which is proportional to the time delay between transmit and reception of each pulse, as in

$$\phi(t) = -\frac{4\pi R(t)}{\lambda}, \tag{2.7}$$

where $R(t)$ is the slant range to the scatterer as a function of time relative to the transmitting time, and is given as

$$R(t) = \sqrt{R_0^2 + v^2(t - t_0)^2}, \tag{2.8}$$

where t_0 is the closest approach time when the slant range $R(t)$ reaches its minimum, R_0, and v is the platform velocity, assumed to be a constant. Hence the phase of the received echoes as a function of time is given by

$$\phi(t) = -\frac{4\pi\sqrt{R_0^2 + v^2(t - t_0)^2}}{\lambda} \ . \tag{2.9}$$

This phase as a function of time for a target at $R_0 = 1000$ m and wavelength $\lambda = 8.6$ mm is plotted in Figure 2.3.

If the antenna beam is narrow in the sense that $vT/2 \ll R_0$, where T is the aperture time, then the expression in (2.9) can be approximated as

$$\phi(t) \simeq -\frac{4\pi R_0}{\lambda} - \frac{2\pi v^2(t - t_0)^2}{\lambda R_0}, \tag{2.10}$$

which is in a quadratic form, and is equivalent to a linear frequency modulated(LFM) waveform. This is shown in Figure 2.3. The previous results of the pulse compression with a LFM signal immediately applies. To determine the resolution, the bandwidth of this LFM waveform if found through (2.10), where the linear FM bandwidth is given by

$$B_D = 2|f(t_0 + \frac{T}{2})| = \frac{2}{2\pi}\left|\frac{d\phi(t)}{dt}\right|_{t-t_0=\frac{T}{2}} = \frac{2v^2T}{\lambda R_0}, \tag{2.11}$$

where T is the aperture time during which the scatterer is illuminated by the antenna beam. This bandwidth is also called the Doppler bandwidth since it is caused by the

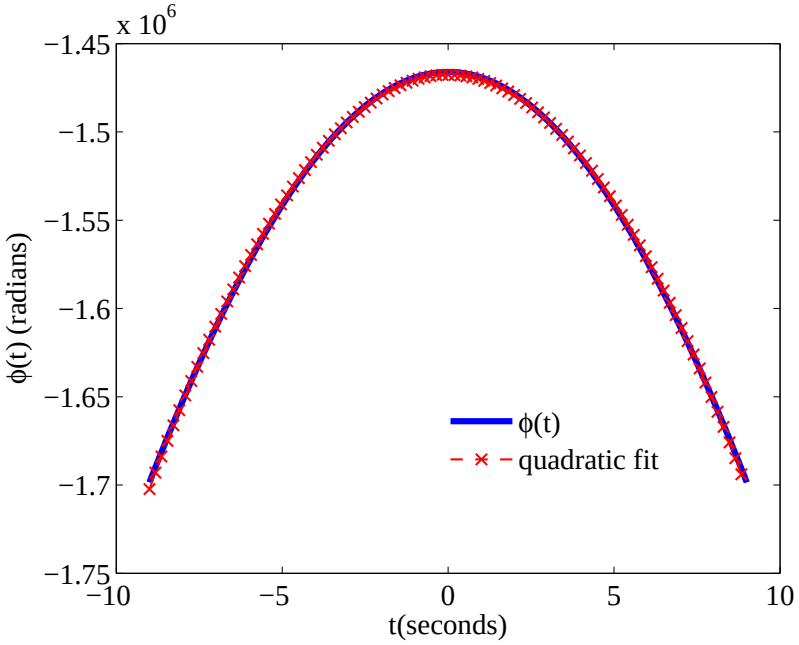

Figure 2.3: The instantaneous phase of the radar echoes as a function of time, the quadratic fit is also shown. The parameters used for this curve is $R_0 = 1000$ m, $v = 65$ m/s, and $t_0 = 0$ s.

Doppler effect. Further, from Figure 2.1, the aperture time, T, is the aperture size divided by the platform velocity, and is given by

$$T = \frac{\lambda R_0}{L_a}\frac{1}{v}, \tag{2.12}$$

in which L_a is the antenna azimuth length. Then the Doppler bandwidth can be written as,

$$B_D = \frac{2v}{L_a}, \tag{2.13}$$

The time domain resolution is then given by the inverse of Doppler bandwidth,

$$\Delta t = \frac{1}{B_D} = \frac{L_a}{2v}, \tag{2.14}$$

which, when combined with the platform velocity, gives the spatial resolution in the azimuth direction as

$$\Delta X = v\Delta t = \frac{L_a}{2}. \tag{2.15}$$

Hence, ideally the spatial resolution of a synthetic aperture radar only depends on the antenna azimuth size, and is not related to the antenna beamwidth and the range to the scatterer.

2.1.2 Squinted Case

The above results are derived for the broadside case, which means that the antenna main-beam direction resides in the plane perpendicular to the moving direction. When the antenna main-beam is not perpendicular to the platform, it is known as being a squinted geometry. The angle between the antenna main-beam and the radar moving direction is called the squint angle, as shown in Figure 2.4.

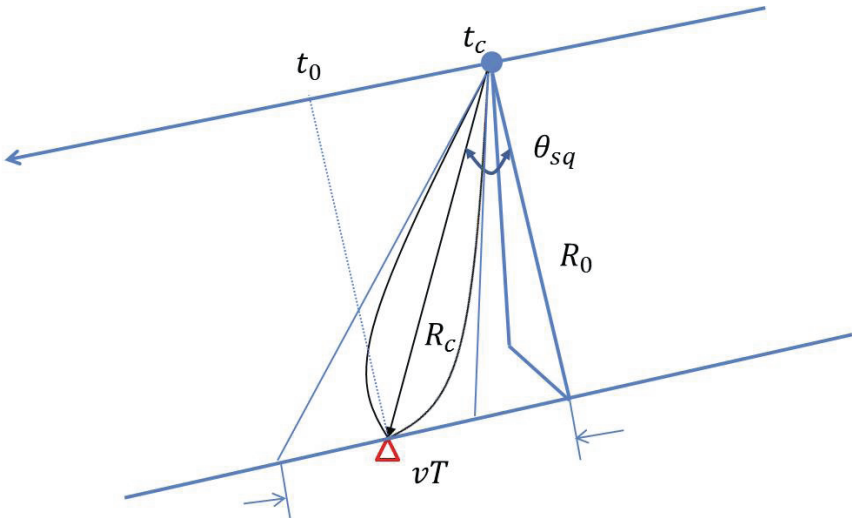

Figure 2.4: The diagram of a squinted SAR.

The squint angle is denoted as θ_{sq}. In the small squint angle case, the approximation in (2.10) is still valid. For a large θ_{sq}, a Taylor expansion is taken at the vicinity of the time when the beam center is crossing the scatterer, denoted as t_c. This gives

$$\begin{aligned}\phi(t) &= -\frac{4\pi R_0}{\lambda}\sqrt{1+\frac{v^2(t-t_c+t_{c0})^2}{R_0^2}} \\ &\approx -\frac{4\pi}{\lambda}\left(R_c+\frac{v^2 t_{c0}}{R_c}(t-t_c)+\frac{v^2 R_0^2}{2R_c^3}(t-t_c)^2\right),\end{aligned} \tag{2.16}$$

in which $t_{c0} = t_c - t_0$, and t_c is the beam center crossing time, t_0 is the zero-Doppler time. $R_c = \sqrt{R_0^2 + v^2 t_{c0}^2}$ is the slant range at t_c. Now the instantaneous frequency $f(t)$ is

$$f(t) = -\frac{2v^2}{\lambda R_c}\left(t_{c0} + (\frac{R_0}{R_c})^2(t-t_c)\right). \tag{2.17}$$

Thus the Doppler bandwidth becomes

$$\begin{aligned}B_{D,sq} &= \frac{2v^2}{\lambda R_c}\frac{R_0^2}{R_c^2}T \\ &\approx \frac{2v^2}{\lambda R_c}\frac{R_0^2}{R_c^2}\frac{\lambda R_c}{L_a \cos\theta_{sq}}\frac{1}{v} \\ &= \frac{2v}{L_a}\cos\theta_{sq}.\end{aligned} \tag{2.18}$$

Hence the Doppler bandwidth for the squinted case is decreased by a factor of $\cos\theta_{sq}$ compared to the zero-Doppler case. Accordingly, the azimuth resolution is also degraded by the same factor:

$$\Delta X_{sq} = \frac{L_a}{2\cos\theta_{sq}}. \tag{2.19}$$

Similar to the Doppler effect, the fine-resolution in the range-direction is achieved through transmitting a LFM waveform at each azimuth position. Hence the slant range resolution is proportional to the inverse of the system bandwidth

$$\delta r = \frac{c}{2BW}, \tag{2.20}$$

where c is the speed of light in free space, and BW is the bandwidth of the LFM waveform. As an example, the slant range resolution is 1.5 meters for a system with bandwidth of 100MHz.

2.1.3 Approximation Error

In the previous subsection, the instantaneous phase, ϕ_t, is approximated with a quadratic form which is valid for the narrow beam case. Thus the error can be written as

$$\begin{aligned}\phi_{err}(t) &= -\frac{4\pi}{6\lambda}\frac{3v^4R_0^2}{R_c^5}(t-t_c)^3 + \mathcal{O}((t-t_c)^4) \\ &= \frac{2\pi v^3}{\lambda R_0^2}\tan\theta_{sq}\cos^5\theta_{sq}(t-t_c)^3 + \mathcal{O}((t-t_c)^4)\,,\end{aligned} \tag{2.21}$$

where the first term is the third order term of the Taylor expansion of $\phi(t)$. The maximum phase error occurs at edge of the aperture with

$$t - t_c \leq \frac{1}{2}R_c\frac{\lambda}{L_a}\frac{1}{\cos\theta_{sq}}\frac{1}{v}, \tag{2.22}$$

where at the aperture edge, the phase error is

$$\phi_{err} = \frac{\pi\lambda^2 R_0\tan\theta_{sq}}{4L_a^3\cos\theta_{sq}}. \tag{2.23}$$

2.2 FMCW Radar

Following (2.20), the slant range resolution is inversely proportional to the system bandwidth, BW. Either a narrow pulse, a modulated signal, or the combination of both could be utilized to achieve the required range resolution. By using a modulation scheme over a long duration pulse, a radar system can have a large bandwidth and proportionally smaller range resolution. Hence, the pulse energy can be decoupled from the range resolution. Linear frequency modulation, also called a chirp signal, is widely used in pulsed radars. While having a good performance, the complexity of the hardware and pulse timing control system of the system increases. The system complexity and cost can be reduced by using modulated continuous

wave (CW) instead of pulses, which gives the linear frequency modulated continuous wave (FMCW) radar architecture, shown in Figure 2.5. The up-converting and down-converting parts are omitted for simplicity.

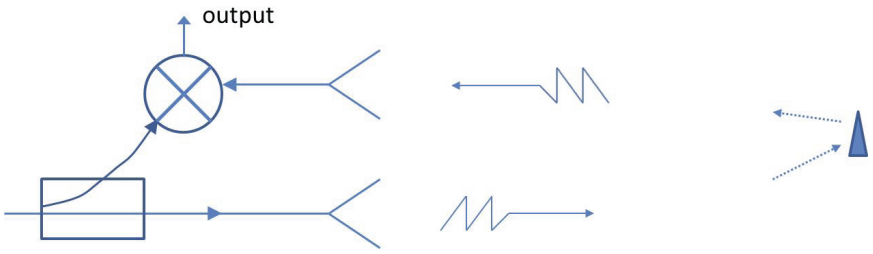

Figure 2.5: An simple illustration of FMCW radar architecture.

Since FMCW radar transmits signal continuously, there is no need for any timing control. In addition, an on-board de-chirping technique, shown in Figure 2.5, can be utilized based on its CW characteristic. This greatly simplifies the demodulation hardware and data acquisition section of the radar system. The FMCW radar has two main drawbacks. One is that it is transmitting at the same time the receiver is turned on. The other is that the platform is moving while the radar is transmitting and receiving signals, then the conventional stop-and-go approximation may not be sufficiently accurate[1]. Such would be the case if there was an appreciable phase variation due to the Doppler shift during the transmission and reception of each pulse. An extra processing step may therefore be needed to take care of this variation [18].

For FMCW radars, the transmitted signal is continuous and periodic, the mathematical expression of one cycle is given as

$$g_t(t) = cos(2\pi f_0 t + \pi\beta t^2 + \phi_0), \quad t \in [0, T]\,. \tag{2.24}$$

[1]The stop-and-go approximation assumes the radar stops at current position, transmits and receives a pulse, then moves to the next position.

Under normal operation, the radar repeatedly transmits this waveform, as shown in Figure 2.6(a) with two cycles. The instantaneous frequency is plotted in Figure 2.6(b).

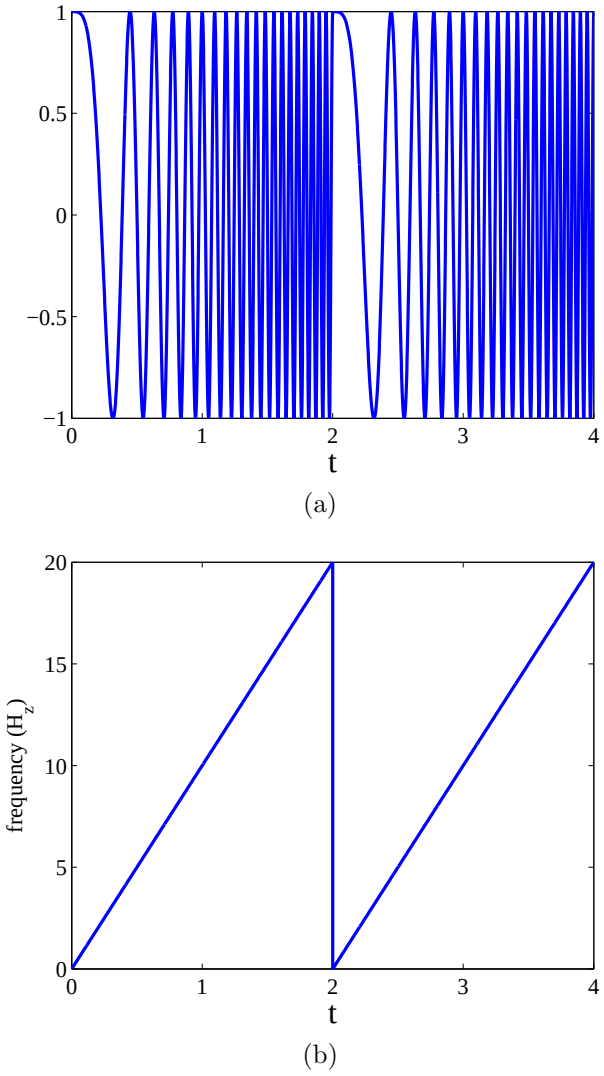

Figure 2.6: (a)The waveform of a linear chirp with two cycles. (b)The instantaneous frequency versus time.

The received radar echo of the backscatter from a point scatterer is a time shifted version of the transmitted signal, given as

$$
\begin{aligned}
g_r(t) &= g_t(t-\tau_0) \\
&= cos(2\pi f_0(t-\tau_0) + \pi\beta(t-\tau_0)^2 + \phi_0), \quad t \in [\tau_0, T+\tau_0],
\end{aligned}
\tag{2.25}
$$

in which τ_0 is the time delay between the time between transmission and reception of the radar echo.

As mentioned above, an on-board de-chirping technique is used in FMCW radars to implement the signal demodulation and fulfilling a part of the pulse compression procedure. The block diagram of the de-chirping technique is shown in Figure 2.7. The core of the de-chirping hardware is implemented by a mixer followed by a low pass filter. The effect of the mixer is that the transmitted signal serves as a local oscillator (LO) and downconverts the signal, meanwhile because of the linear frequency property and the time delay between LO and the input signal, the output will be a single-frequency signal, which is given by

$$
\begin{aligned}
s_o(t) &= \mathcal{L}_{\mathcal{P}}\{g_t(t) \times g_r(t)\}, \quad (\mathcal{L}_{\mathcal{P}} : \text{low pass filtering}) \\
&= \frac{1}{2} cos(2\pi\beta\tau_0 t + 2\pi f_0\tau_0 - \pi\beta\tau_0^2), \quad t \in [\tau_0, T].
\end{aligned}
\tag{2.26}
$$

Here only one point scatterer at the range $R = \frac{c\tau_0}{2}$ is considered. It can be seen that the output signal, $s_0(t)$, is a single-tone pulse with frequency of $\beta\tau_0$, which is proportional to the time delay, τ_0, of the radar echo and the chirp rate, β. Hence there exists a linear one-to-one mapping from slant range, R, to the frequency, f_{τ_0}, of $s_0(t)$, which is $R = \frac{cf_{\tau_0}}{2\beta}$. When there are multiple scatterers at different ranges or distributed scatterers, the output is a superposition of the single-tone signals with different frequencies and phase. Equivalently, this is an integration of the single-tone output with respect to delay τ.

The output signal is sampled sequentially by a baseband digitizer and stored in the hard drive of a computer as a time series for further processing. To complete the range compression, a matched filter is still needed for the recorded data. Designing

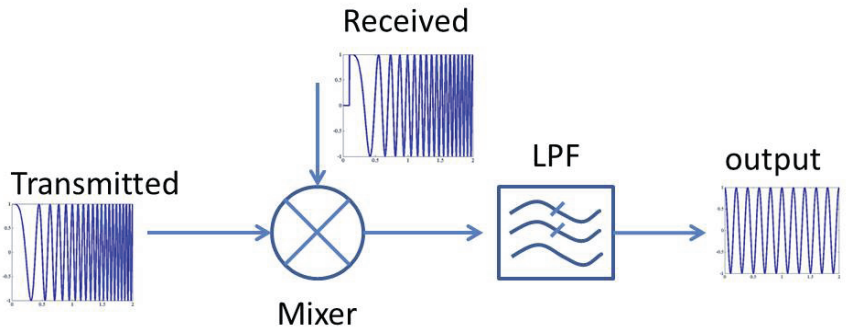

Figure 2.7: The block diagram of de-chirp on board scheme.

the matched filters using the time-reversed of the input signals implies that a filter bank implemented in either software or hardware will be necessary. Instead, a Fourier transform of the output signal can be utilized to realize the range compression. In this case, each tone in the signal is transformed to a sinc function in the frequency domain, and the label of frequency can be easily translated to the range domain with a linear relation between them. An advantage to this approach is that the FFT (Fast Fourier Transform) can be utilized to improve the efficiency of the compression.

2.2.1 Range Compression

As mentioned in the previous section, the range compression can be performed by taking a Fourier transform of the recorded pulse samples of $s_o(t)$. The result of Fourier transform for a point scatterer can be written as

$$\begin{aligned} \mathcal{S}(f;\tau_0) &= \int_{\tau}^{T} s_o(t;\tau_0) e^{-j2\pi ft} dt \\ &= \frac{1}{2}\int_{\tau}^{T} cos(2\pi\beta\tau_0 t + 2\pi f_0\tau_0 - \pi\beta\tau_0^2) e^{-j2\pi ft} dt \\ &= S_+(f;\tau_0) + S_-(f;\tau_0), \end{aligned} \tag{2.27}$$

where the spectrum $\mathcal{S}(f;\tau_0)$ is decomposed into two parts, $S_+(f;\tau_0)$ and $S_-(f;\tau_0)$, the parameter τ_0 in the parenthesis means that the derived spectrum is in the case of

a point scatterer which has a time delay of τ_0 to the radar. The expressions of $S_+(f)$ and $S_-(f)$ are

$$\begin{aligned} S_+(f;\tau_0) &= \frac{T-\tau_0}{4} e^{j(\pi(\beta\tau_0 - f)(T+\tau_0)+\phi_{\tau_0})} \mathrm{sinc}\big((T-\tau_0)(f-\beta\tau_0)\big), \qquad (2.28) \\ S_-(f;\tau_0) &= S_+^*(-f;\tau_0). \qquad (2.29) \end{aligned}$$

The sign in subscript indicates whether the peak location of the sinc$(\cdot)$ function is at the positive or the negative frequency region. In the above expressions,

$$\phi_{\tau_0} = 2\pi f_0 \tau_0 - \pi\beta\tau_0^2 \qquad (2.30)$$

and the sinc$(\cdot)$ function is defined as $\mathrm{sinc}(x) = \frac{sin(\pi x)}{\pi x}$. It shows in (2.30) that the negative part of the spectrum $S_-(f;\tau_0)$ is a conjugate reflection of its positive counterpart $S_+(f;\tau_0)$. Hence, $S_+(f;\tau_0)$ alone is sufficient to represent the original spectrum.

The next step in processing is to translate $S_+(f;\tau_0)$ from the frequency domain to a range domain profile, $S(R;\tau_0)$, using the linear mapping between frequency and range, which was shown in the previous subsection, and given by $f = \frac{2\beta R}{c}$, as in

$$\begin{aligned} S(R;\tau_0) &= S_+(f;\tau_0)|_{f=\frac{2\beta R}{c}}, \\ &= \frac{T-\tau_0}{4} e^{j\left(\pi(\beta\tau_0 - \frac{2\beta R}{c})(T+\tau_0)+\phi_{\tau_0}\right)} \qquad (2.31) \\ &\quad \cdot \mathrm{sinc}\left(\frac{2}{c}\beta(T-\tau_0)(R-\frac{c\tau_0}{2})\right). \qquad (2.32) \end{aligned}$$

By defining

$$\begin{aligned} R_0 &= \frac{c\tau_0}{2}, \\ \phi(R-R_0) &= \frac{2\pi\beta}{c}(R-\frac{c\tau_0}{2})(T+\tau_0) \end{aligned} \qquad (2.33)$$

and

$$\alpha(\tau_0) = \frac{2\beta}{c}(T-\tau_0)\ , \qquad (2.34)$$

$S(R;\tau_0)$ can be further simplified as

$$S(R;\tau_0) = \frac{T-\tau_0}{4} e^{-j(\phi(R-R_0)-\phi_{\tau_0})} \mathrm{sinc}\left(\alpha(\tau_0)(R-R_0)\right). \tag{2.35}$$

To illustrate by example, the range profile, $S(R;\tau_0)$, for a simulated scatterer located at $R_0 = 750\,\mathrm{m}$ is plotted in Figure 2.8. The range resolution, which is the minimum range between two point scatterers which can be resolved, can be calculated from the 3-dB beamwidth of main-lobe of the sinc function, as in

$$\Delta R = \frac{1}{\alpha(\tau_0)} \simeq \frac{c}{2\beta T} = \frac{c}{2BW}, \tag{2.36}$$

which is equivalent to the range resolution given by the system bandwidth.

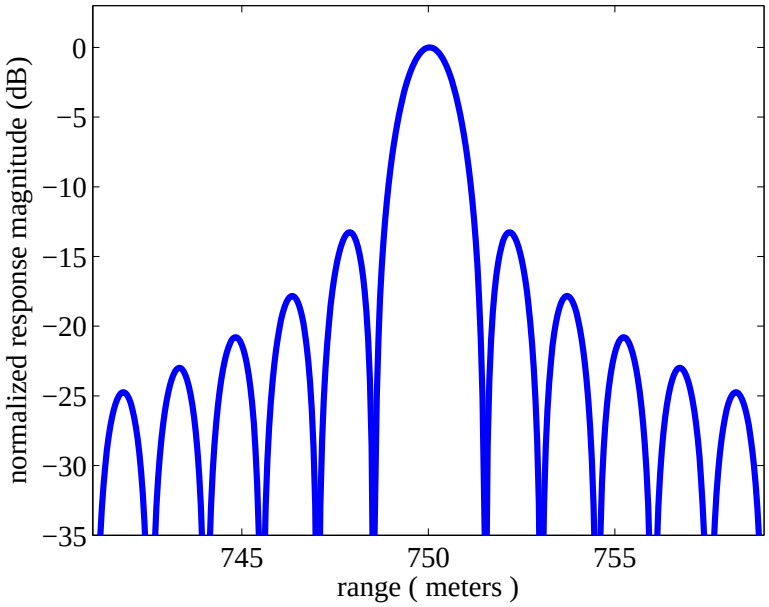

Figure 2.8: The point scatterer response of a scatterer at range of 750 meters. The pulse duration is 1 ms, and the chirp rate, β, is 100 MHz/ms. The 3-dB beamwidth of the main-lobe is 1.5 meters, which is the range resolution of the radar system.

2.3 Radar Interferometry

Interferometry is a technique widely used in many different areas of science and engineering, such as astronomy, seismology, etc, and refers to the use of a signal's phase in comparison to another signal, for deriving quantitative information about the interaction. In radar interferometry, the direction of a scatterer with respect to the radar is estimated through the coherent superposition of the outputs of multiple receivers. In synthetic aperture radar interferometry, two or more antennas, separated by a baseline, are used for receiving the radar echo from the same scatterer. These receiving antennas can observe the scatterer at the same time (single-pass) or at different times (repeat-pass). The Ka-band radar in this dissertation is configured for single-pass interferometry.

A diagram showing the geometric configuration of radar interferometry is shown in Figure 2.9. Here, the along-track direction is perpendicular to the page. In the figure, the points labeled as A1 and A2 denote the two receive antennas of the radar system. The transmission antenna can be one of the receive antennas or a third antenna, which is not shown in the figure. The red dot indicated by the P indicates a point scatterer.

In Figure 2.9(a), it shows that the radar system just measures the ranges from the scatterer to the two antennas when no other information is available. The signals for the two channels after the range compression are $S_1(R)$ and $S_2(R)$ respectively. According to (2.35), they can be expressed as

$$S_1(R) = A_1 e^{-j(\phi(R-R_1)-\phi_{\tau_1})} \mathrm{sinc}\big(\alpha_1(R-R_1)\big), \text{and} \tag{2.37}$$

$$S_2(R) = A_2 e^{-j(\phi(R-R_2)-\phi_{\tau_2})} \mathrm{sinc}\big(\alpha_2(R-R_2)\big). \tag{2.38}$$

After co-registration, the correlation between these two received signals can be calculated to get the differential phase using (2.30), as in

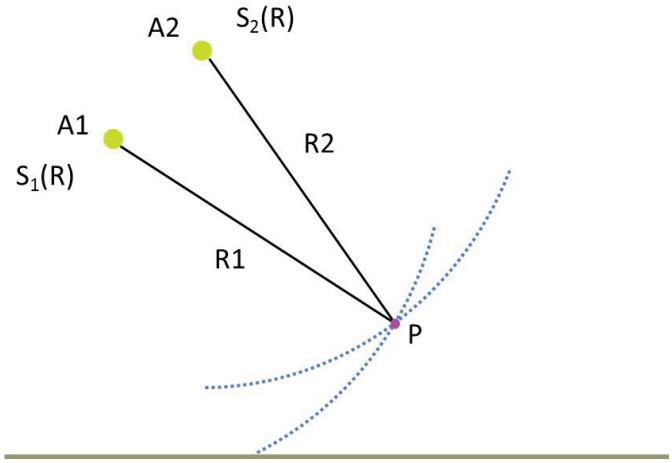

(a)

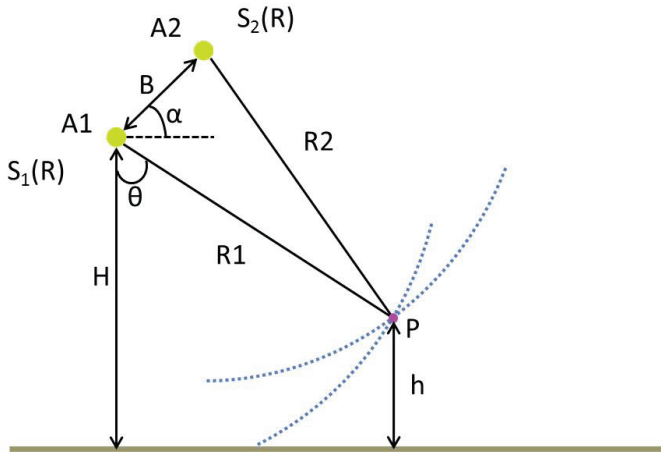

(b)

Figure 2.9: Diagram of radar interferometry.

$$\begin{aligned}
\phi &= \phi_{\tau_1} - \phi_{\tau_1} \\
&= 2\pi f_0 \tau_1 - \pi\beta\tau_1^2 - 2\pi f_0 \tau_2 + \pi\beta\tau_2^2 \\
&= 2\pi(\tau_1 - \tau_2)(f_0 - \beta\frac{\tau_1 + \tau_2}{2}) \\
&\simeq 2\pi f_0(\tau_1 - \tau_2). \qquad (2.39)
\end{aligned}$$

The above approximation is valid when $f_0 \gg \beta\frac{\tau_1+\tau_2}{2}$. Since the two receive antennas share the same transmission path, (that is $\tau_i = \tau_T + \tau_{r,i}, \text{for}\, i = 1, 2$), the difference of delays $\tau_1 - \tau_2$ depends only on the the difference between the receiving paths.

Therefore (2.39) can be written as

$$\phi = 2\pi f_0(\tau_{r,1} - \tau_{r,2}) = \frac{2\pi f_0}{c}(R_1 - R_2) = \frac{2\pi f_0}{c}\Delta R. \tag{2.40}$$

Hence, the differential phase is proportional to the differential range.

With the knowledge of the locations of the two antennas shown in Figure 2.9(b), the height of the scatterer, h, relative to a pre-defined flat-earth can then be derived. In Figure 2.9(b), the radar altitude, H, the distance between the two antennas, called baseline B, and the tilt angle of the baseline, α, are the necessary prior information which are obtained from lab measurements or GPS measurements of platform altitude made during flights.

The height of terrain, h, is related to these spatial parameters as

$$h = H - R_1\cos(\theta). \tag{2.41}$$

Since the look angle, θ, is not directly measurable, it is determined from the baseline length, tilt angle, and the differential range, ΔR, in (2.40) using the law of cosines, such that

$$\begin{aligned} R_2^2 &= R_1^2 + B^2 - 2R_1B\cos(\alpha + \frac{\pi}{2} - \theta), \\ \Delta R = R_1 - R_2 &= \frac{2R_1B\cos(\alpha + \frac{\pi}{2} - \theta) - B^2}{R_1 + R_2} \\ &\approx B\cos(\alpha + \frac{\pi}{2} - \theta) \\ &= B\sin(\theta - \alpha)\,. \end{aligned} \tag{2.42}$$

The approximation in (2.42) is valid if $R_1 \approx R_2 \gg B$, which is true for most practical cases, and hence a substitution is made so that,

$$\theta \approx \alpha + \sin^{-1}\big(\frac{\Delta R}{B}\big). \tag{2.43}$$

By substituting (2.40) and (2.43) into (2.41), an expression for the height is written as

$$h = H - R_1 \cos\left(\alpha + \sin^{-1}\left(\frac{c\,\phi}{2\pi f_0 B}\right)\right). \tag{2.44}$$

This shows that the topography can be determined from the differential phase and other radar parameters. The advantage of using the phase instead of the differential range is that it can obtain much better accuracy by measuring the phase. Because the phase measurement can achieve sub-wavelength accuracy, the corresponding accuracy of the differential range will be within a wavelength, which is usually much smaller than the range resolution of the radar, $\Delta R = \frac{c}{2BW}$. However the phase, ϕ, can have an ambiguity of $2\pi N$, where N is an integer, in a phenomenon known as phase wrapping for every 2π, which introduces a height ambiguity. In the horizontal planes where local topography is not known very well, phase unwrapping algorithms are often necessary, at the cost of increased processing complexity. However if the topography is known to some degree, the interferometric phase can be estimated through the viewing geometry.

CHAPTER 3

SYSTEM OVERVIEW

In 2007, the University of Massachusetts Amherst created a Ka-band interferometric radar [19, 20]. The Ka-band interferometric radar system consists of four sections: (1) Digital baseband, (2) RF front-end, (3) Antennas, and (4) Motion measurement hardware including Inertial Measurement Unit (IMU) and Global Positioning System (GPS). A block diagram of the radar system is shown in Figure 3.1. In the following sections, a detailed description of each block is given.

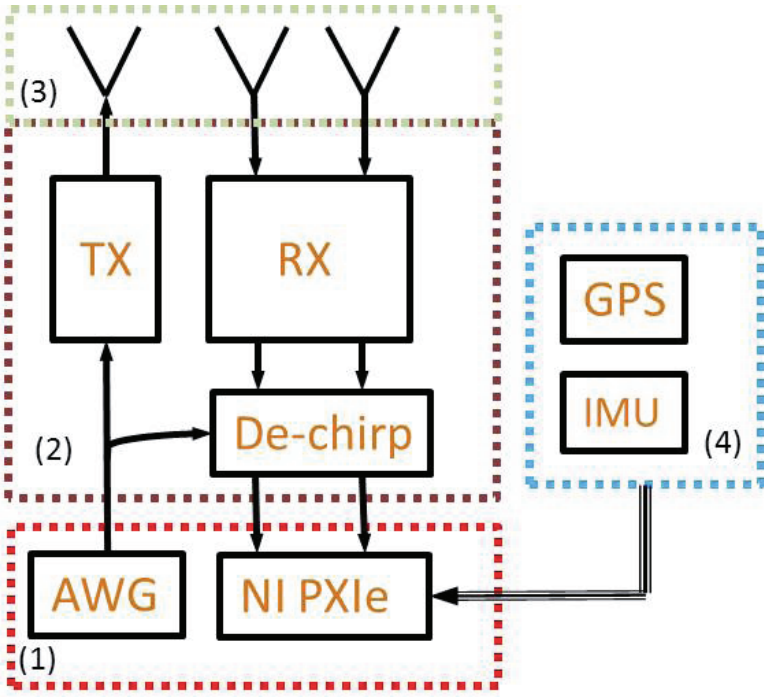

Figure 3.1: The system block diagram.

3.1 Digital Baseband

The digital baseband includes a transmitting and a receiving sub-block. The transmitting part consists of a Tektronix AFG3252 arbitrary waveform generator (AWG), which generates a linear frequency modulated continuous signal. The frequency of the signal sweeps from 5 MHz to 105 MHz in 1 ms. The return time of the signal is 0 s, i.e., its frequency changes from 105 MHz to 5 MHz immediately. A sample waveform from this generator was shown in Figure 2.6 for the purpose of illustration.

The frequency linearity of the signal will affect the system impulse response. A measure of the frequency error versus sweeping time of the signal has been measured by using the technique described in [21], and is shown in Figure 3.2. This figure shows that the frequency errors are piecewise constant. Since the frequency errors are the same for both transmitted and received signals, it can be shown that the effects due to these errors are negligible because most of the error is canceled in the de-chirping procedure. During the time that the frequency errors are not canceled due to the time delay of the received signal, the effect is small since these time durations (on the order of several micro-seconds) are much shorter than the the cycle of the pulse, 1ms. Hence their effect can be neglected. An evaluation of the waveform linearity with a simulation of a point target located at a slant range of 800 meters is shown in Figure 3.3. It can be seen that the spurs caused by the waveform nonlinearity is below -44 dBc. This is one of the limiting factor of the dynamic range in the slant range dimension of this radar system.

The digital part of the receiver consists of a National Instruments PXI-5152 8-bit digitizer with a 256 GB solid state drive (SSD). The received signals are from the output of the de-chirping hardware. The sampling rate was set to 2 MSamp/s for each channel, thus the total data rate is 4 MSamp/s, which is well below the maximum data rate available of the digitizer and the SSD. The maximum slant range corresponding to the sampling rate is given by $R_{max} = \frac{cF_s}{4\beta} = 1500\,\mathrm{m}$.

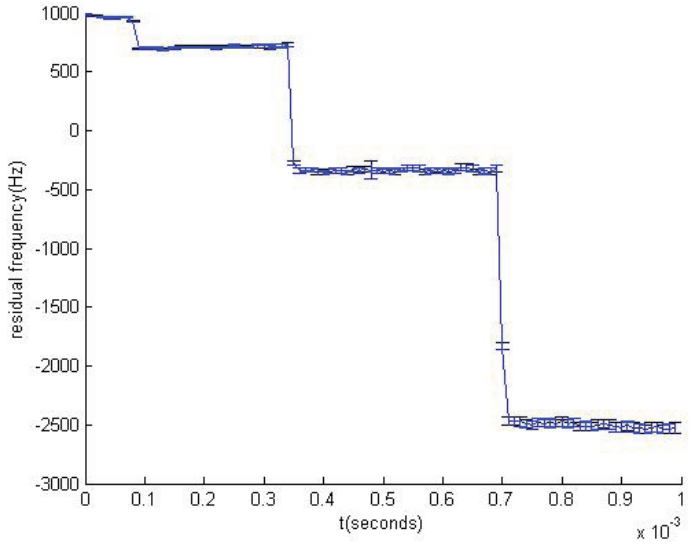

Figure 3.2: The measured frequency errors with respect to the nominal linear frequency of the chirp, which is linearly changing from 5 MHz to 105 MHz in 1 ms.

3.2 RF Frontend

3.2.1 Transmitter and Receiver

Both the transmitter and the receiver employ a two-stage superheterodyne architecture. The transmitter has a baseband to L-band up-converting stage and an L-band to Ka-band up-converting stage (Figure 3.4). The receiver contains a Ka-band to L-band down-converting stage and a L-band to baseband down-converting stage (Figure 3.5). The metallic connectors with screws are 2.4 mm connectors capable of operating at frequencies up to 40 GHz. The benefit of using two stages is that most of the gain blocks can be placed in the L-band to baseband stage with lower cost and smaller phase variation caused by the active components in the receiver due to temperature variations. The local oscillator (LO) frequencies are 1.3 GHz and 33.7 GHz for the two stages. They are provided by the outputs of stand-alone phase-locked oscillators (PLO), which have very low phase noise, typically -90 dBc/Hz at 100 kHz. The outputs of the transmitter board are fed into a 1 W off-board solid-state Ka-band

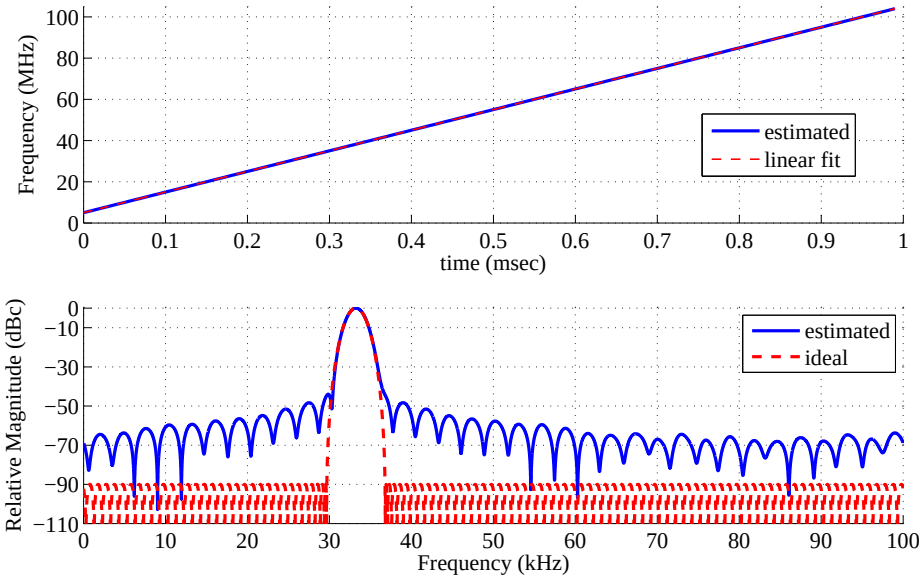

Figure 3.3: Waveform linearity evaluation: (Top)The estimated chirp frequency versus time. (Bottom) The simulated point target response for a target at 800 meters with the estimated waveform. A 90-dB chebyshev window is used in the simulation.

power amplifier. The parameters of the transmitter and the receiver are summarized in Table 3.1 below.

Parameter	Transmitter	Receiver
Bandwidth (BW)	100 MHz	100 MHz
Gain	N/A	70dB
Power	1 W	N/A
Noise Figure	N/A	4.5dB
$IP1_{in}$	N/A	-60 dBm

Table 3.1: Transmitter and receiver parameters.

3.2.2 Phase Characterization

The phase performance of the system can affect the imaging quality and measurement accuracy in two different ways. One is the short-term phase error and the other is the long-term phase instability.

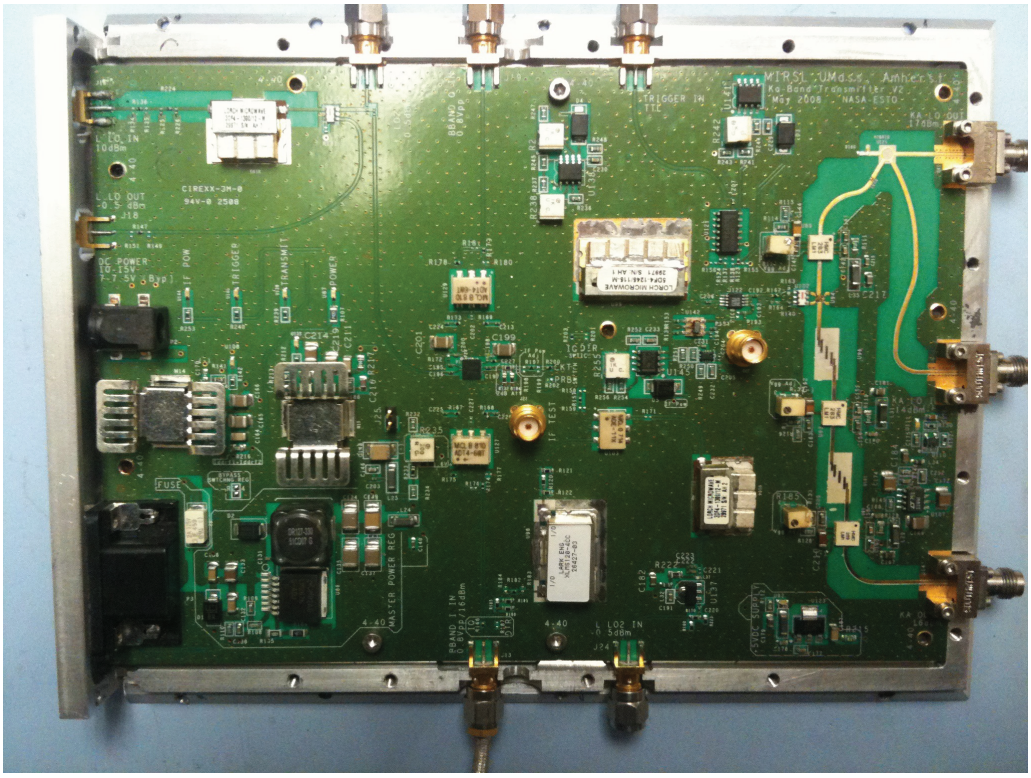

Figure 3.4: The photo of the transmitter board.

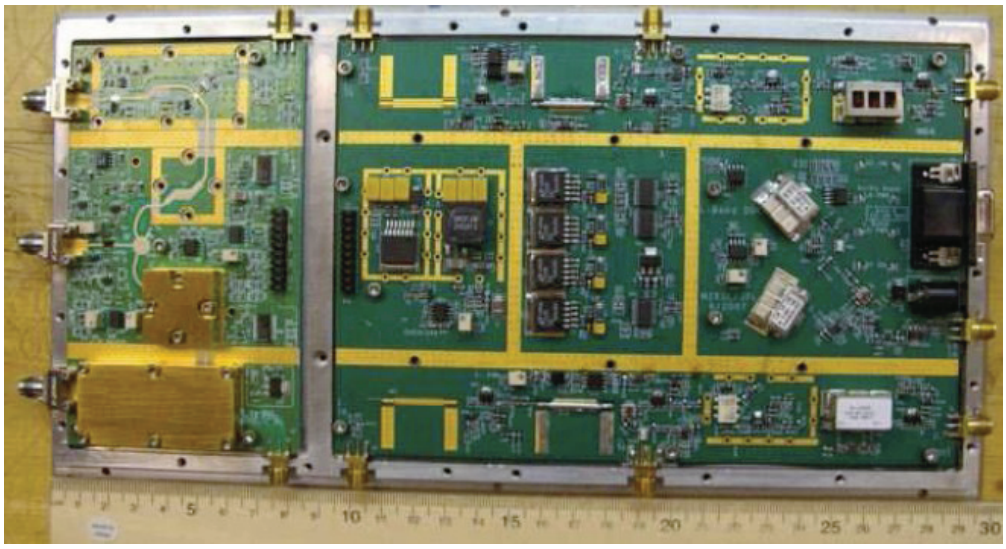

Figure 3.5: The photo of the receiver board.

Since the chirp signal usually occupies a wide bandwidth, 100 MHz in this case, the nonlinear phase response of the system (i.e. non-flat group delay) within the chirp

sweep time will cause a distortion to the input chirp signal. The input signal will be squeezed or stretched in the time domain. The measured group delay of the two system channels is shown in Figure 3.6. This causes frequency nonlinearities which is undesired in the range compression. The measured frequency nonlinearities caused by the system (including the transmitter and the receiver) are shown in Figure 3.7.

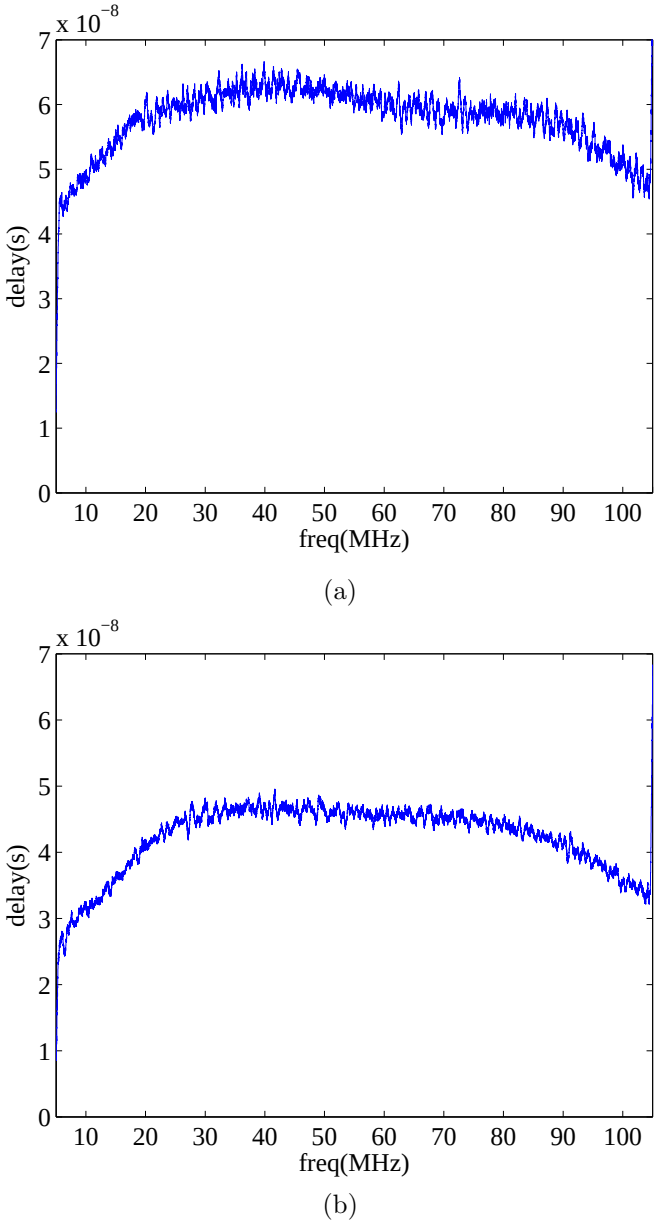

Figure 3.6: Measured group delay of the system. (a) Channel 1. (b) Channel 2.

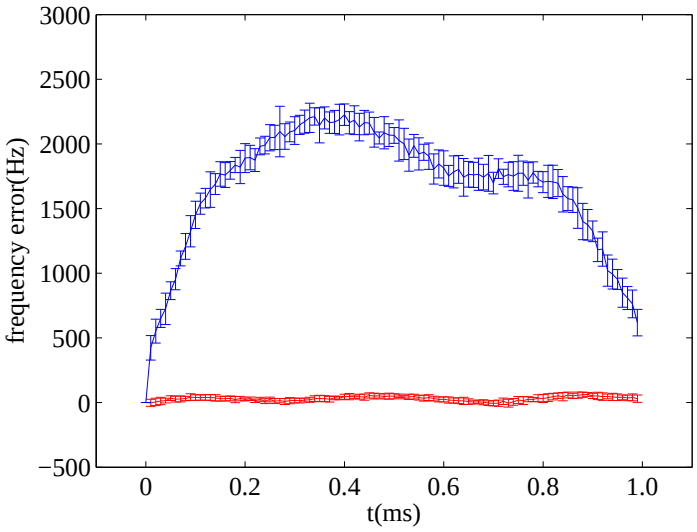

(a)

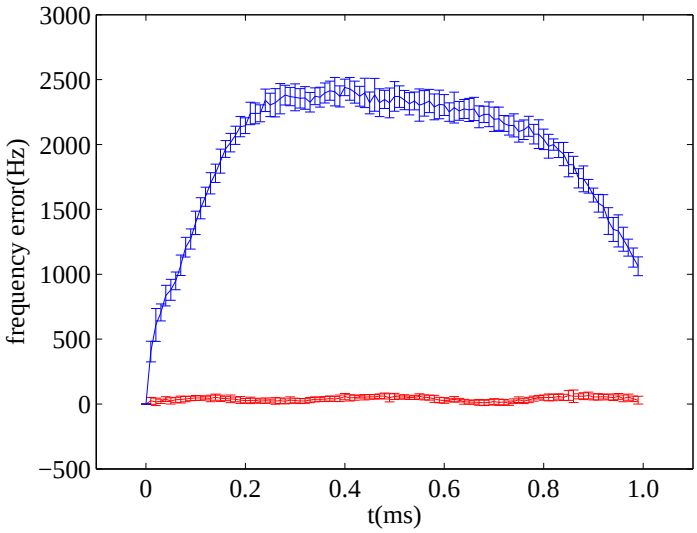

(b)

Figure 3.7: The frequency errors caused by the nonlinearity of the system. The red curve (lower) is for the input signal to the sysem, and the blue curve (upper) is for the output signal. (a) Channel 1. (b) Channel 2.

The long-term phase instability is characterized by the variation of differential phases in terms of environmental changes, which is the temperature change in this case. The differential phase instability is caused by the mismatch of the thermal distribution on the circuit board between the two channels. This variation will intro-

duce a time varying bias to the phase expressed in (2.40) and will cause topographic error via the measurement given by (2.44). Because of concerns such as this, the phase stability of the receiver has been measured and the result is shown in Table 3.2

Parameter	Ka-L	L-Baseband
Temperature coefficient (degrees of phase/degrees of temperature in C)	0.035	0.121
standard deviation (degrees of phase/degrees of temperature in C)	0.0076	0.0052

Table 3.2: The measured phase stability versus temperature for the two stages of the receiver.

3.2.3 De-chirping Hardware

The on-board de-chirping technique is used to demodulate the received signals with the transmitting signal. The demodulated signal is low-pass filtered and amplified, then delivered to the baseband digitizer described in Section 3.1. The diagram of the de-chirping hardware was shown in Figure 2.7. The de-chirping circuitries are identical for both channels.

3.3 Ka-band Antennas

In the UMass Ka-band InSAR, there are three identical Ka-band antennas in the system, one of them is the transmitting antenna and the other two are the receiving antennas. The antennas are slotted waveguide antennas. The center frequency of the antenna is 34.945 GHz, and the return loss at this frequency is 12 dB. The beam pattern of the antenna is designed to be narrow in the azimuth direction and broad in the elevation direction, called fan-beam [19]. The antenna patterns are shown in Figure 3.8. With a beam pattern such as this, it is possible to have a large range coverage and reasonable azimuth resolution even without performing synthetic aperture focusing. With a physical dimension of 50 cm in length and 1 cm in width,

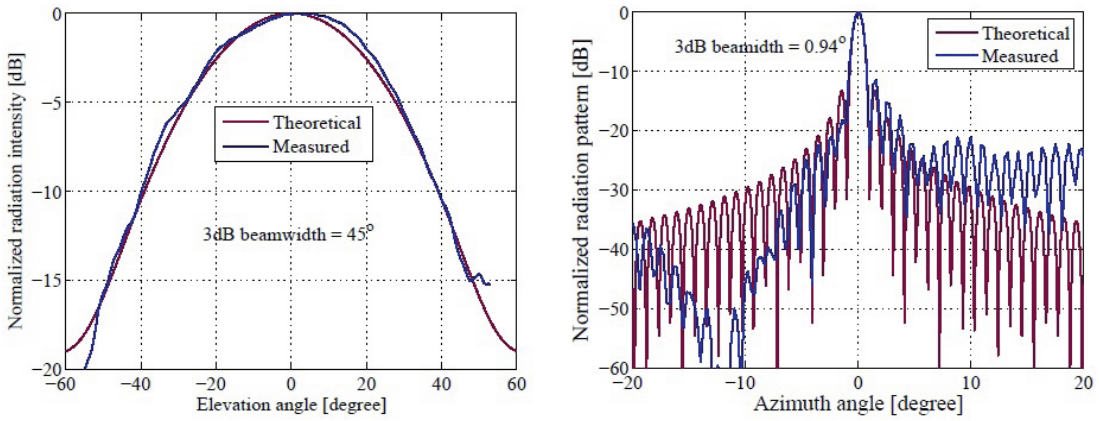

Figure 3.8: Measured and theoretical E-plane (left) and H-plane (right) radiation patterns for the interferometer antenna.

their beamwidth of the antenna is 1° in azimuth and 45° in elevation. A picture of one antenna being measured is shown in Figure 3.9.

3.4 Motion Measurement Instruments

As given by (2.44), the platform height is directly related to the topographic measurement. In addition, other attitude parameters such as platform velocity and steering angles are also necessary in processing the data as shown in the next chapter. To obtain the attitude information of the platform, an inertial measurement unit (IMU) and GPS device is employed on the platform. The IMU records pitch, roll and yaw angles and their rates of change versus time. The frame rate for this data is 71.1 Hz. The resolution of pitch, yaw and roll angle is 0.02° and the dynamic accuracy is ±0.5%. The GPS records the platform's three-dimensional position, including latitude, longitude and altitude and the speed of the platform.

3.5 The Platform

The radar system is mounted on a Cessna 206 aircraft. A spare door was purchased and adapted for the radar [20], shown in Figure 3.10. As can be seen in the figure, the

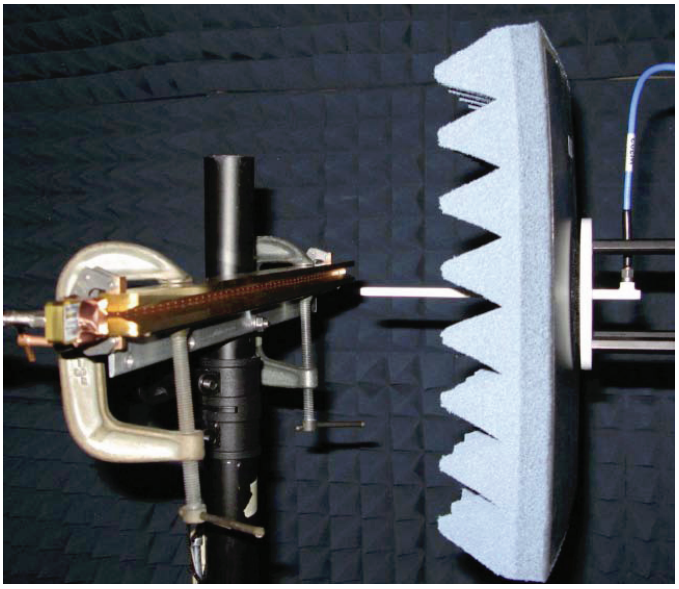

Figure 3.9: Picture of the Ka-band antenna. It is a slot waveguide antenna.

antennas are mounted on the outside. The radar box, containing the RF hardware, and a separate digital system are kept inside the door (not shown).

Figure 3.10: A photo of the Ka-band antennas mounting on the cargo door of the aircraft. The top two are the receiving antennas, and the bottom one is the transmitting antenna.

CHAPTER 4

DATA PROCESSING

To test the radar system, the radar platform was flown over the Connecticut river region in western Massachusetts near Amherst, shown in Figure 4.1, on June 11, 2012. More than 20 Gigabytes of raw data was recorded during this flight and initially was processed as real-aperture images [20]. In this chapter, the procedure of the synthetic aperture radar data processing is described. It begins with loading the raw data from the hard drive. The time series of the digitized samples in the raw data file are first converted to two-dimensional data matrices, with each column containing the radar echo samples from each pulse. Hence the column dimension represents the positions along the flight track. Next the matrices are processed to form a SAR image. Specifically, each scatterer should appear at the correct range and azimuth location with desired resolution in the output SAR image. Among the different SAR processing algorithms, the Range Doppler Algorithm (RDA) [22] is used here, which works well for the FMCW radar except for a minor difference in the range compression compared with the pulsed radar case.

One challenge of the airborne SAR processing is that the distortions and phase errors caused by undesired platform motion. The motion compensation will be addressed in Chapter 5. Figure 4.2 shows a flowchart of the processing procedures of SAR and interferometric SAR processing. In the following sections, each step of SAR processing is given in detail, and the interferometric processing and DEM generation will be the discussed in Chapter 6.

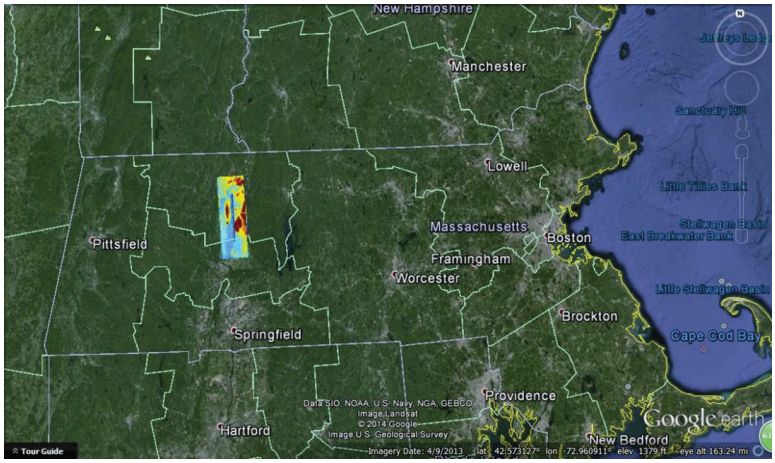

Figure 4.1: The coverage of the Ka-band radar data.

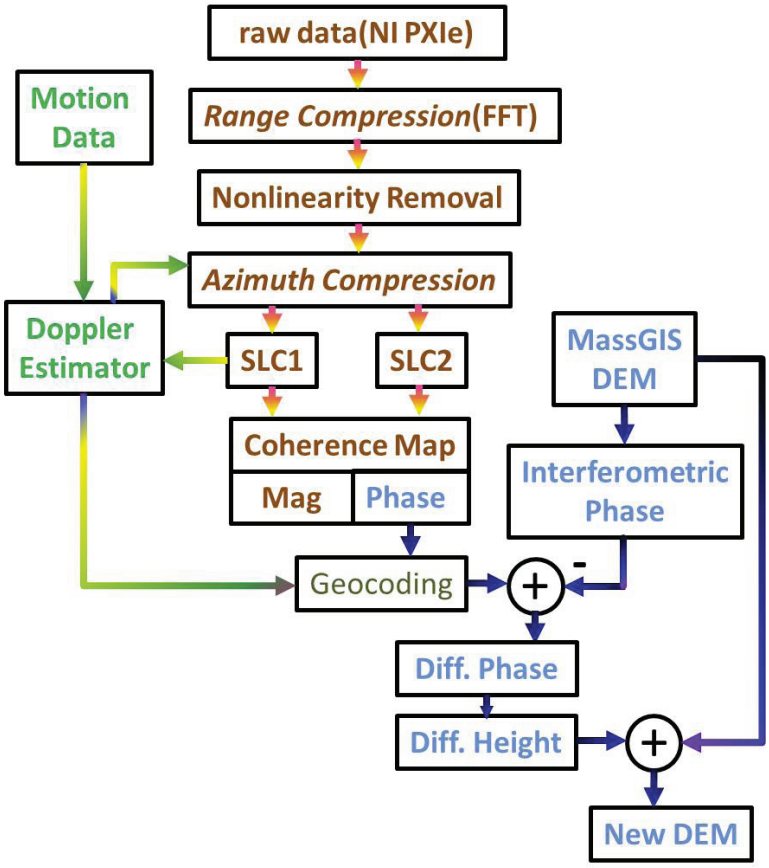

Figure 4.2: The flowchart of interferometric synthetic aperture radar data processing.

4.1 Range Compression

An analytical derivation of the range compression was given in Chapter 2. In this section, the same derivation is used but now the effects of demodulation of the carrier

frequency, f_{LO}, and the range variation with azimuth time, t, is included, since the pulses are transmitted at different t. The time series of the raw data for a point scatterer at its closest range, R_0, is given by

$$\begin{aligned} s(\tau, t; R_0) =& A_0 a_r(\tau - \frac{2R(t;R_0)}{c}) a_a(t - t_c) \cos\Bigg(\frac{4\pi\beta R(t;R_0)}{c}\tau + \frac{4\pi f_0 R(t;R_0)}{c} \\ & - \frac{4\pi\beta R(t;R_0)^2}{c^2} - \frac{4\pi f_{LO} R(t;R_0)}{c} \Bigg), \end{aligned} \tag{4.1}$$

where $a_r(\cdot)$ is the envelope of the transmitted chirp, which is the rectangular function in this case, $a_a(\cdot)$ is the antenna pattern in azimuth direction, f_0 is a the start frequency of the baseband chirp, e.g., the baseband chirp starts from 5 MHz for this InSAR system, f_{LO} is the RF carrier frequency(35 GHz) and β is the chirp rate. In the argument of the cosine function, the beat frequency for a scatterer at range R_0 is

$$\omega_b(t) = \frac{4\pi\beta R(t;R_0)}{c}, \tag{4.2}$$

and the effective carrier frequency is

$$\omega_{LO}^{'} = 2\pi(f_{LO} - f_0)\,. \tag{4.3}$$

The signal $s(\tau, t; R_0)$ can be rewritten as

$$\begin{aligned} s(\tau, t; R_0) = A_0 a_r(\tau - \frac{2R(t;R_0)}{c}) a_a(t - t_c) \\ \cos\Bigg(\omega_b(t)\tau - \frac{2\omega_{LO}^{'} R(t;R_0)}{c} - \frac{\omega_b(t) R(t;R_0)}{c} \Bigg), \end{aligned} \tag{4.4}$$

which shows that the de-chirped signal $s(\tau, t; R_0)$ has a phase term proportional to the effective carrier frequency $\omega_{LO}^{'}$, and another phase term proportional to the beat frequency ω_b, which is much smaller than the carrier frequency.

An example of the collected raw data is shown in Figure 4.3, the corresponding optical image from GoogleEarth is shown in Figure 4.4. One slice of the raw data is plotted in Figure 4.5.

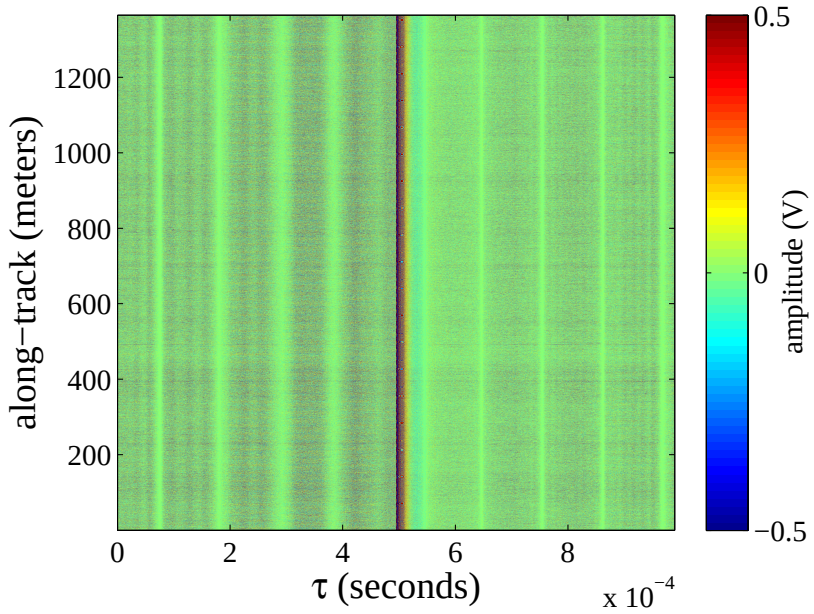

Figure 4.3: The time domain raw data of the selected scene in voltages.

As shown in Section 2.2.1, the range compression is accomplished by calculating the Fourier transform of the raw data $s(\tau, t; R_0)$ with respect to the fast time τ and then a mapping from the frequency domain to the range domain through the relation $r = \frac{cf}{2\beta}$. The compression follows (2.35) except replacing R_0 with $R(t; R_0)$. The range compressed signal is written as

$$\begin{aligned} s(r, t; R_0) =& A_1 \left(T - \frac{2R(t; R_0)}{c}\right) a_a(t - t_c) \operatorname{sinc}\left(\frac{2}{c}\beta(T - \frac{2R(t; R_0)}{c})(r - R(t; R_0))\right) \\ & \cdot \exp\left\{-j\frac{2\pi\beta}{c}\left(T + \frac{2R(t; R_0)}{c}\right)\left(r - R(t; R_0)\right)\right\} \\ & \cdot \exp\left\{-j\left(\frac{2\omega'_{LO}R(t; R_0)}{c}\right)\right\} \cdot \exp\left\{-\frac{\omega_b(t)R(t; R_0)}{c}\right\}, \end{aligned} \tag{4.5}$$

Figure 4.4: The satellite image of the selected scene obtained from Google Earth.

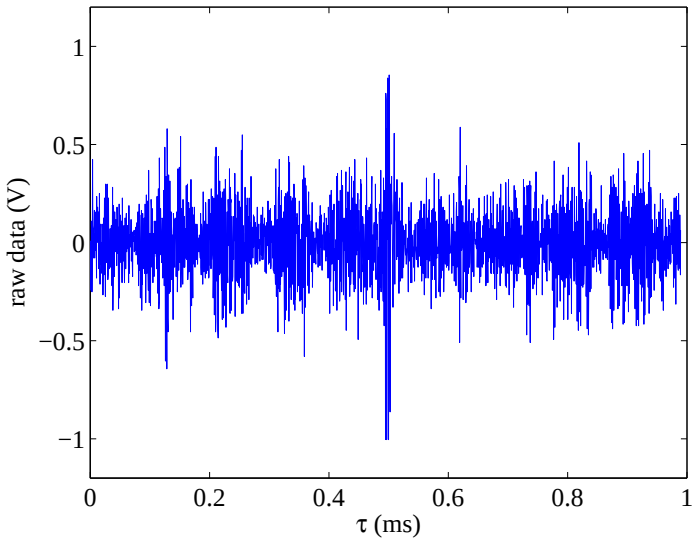

Figure 4.5: One slice of the raw data.

where A_1 is a complex amplitude which has contained the phase term ϕ_3. In (4.5), the argument of the sinc function and the first exponential term represents the

range migration effect, which means that the location of the scatterer in the range compressed image is varying with time t through $R(t;R_0)$; the argument of the second exponential represents the phase due to the effective carrier frequency and the argument of the third exponential term is a quadratic phase which can be seen from (4.4). In the case of an airborne platform, the time delay of the echo $\frac{2R(t;R_0)}{c} \ll T$, thus $s(r,t;R_0)$ can be simplified as

$$\begin{aligned} s(r,t;R_0) \simeq & A_1\, T\, a_a(t-t_c)\,\mathrm{sinc}\big(\frac{1}{\delta r}(r-R(t;R_0))\big) \\ & \cdot \exp\Big\{-j\frac{\pi}{\delta r}\big(r-R(t;R_0)\big)\Big\} \\ & \cdot \exp\Big\{-j\big(\frac{2\omega_{LO}^{'}R(t;R_0)}{c}\big)\Big\}, \end{aligned} \tag{4.6}$$

in which δr is the slant range resolution $\delta r = \frac{c}{2BW} = \frac{c}{2\beta T}$.

A numerical simulation has been done to verify the range compression, with the results shown in Figure 4.6. The parameters used for this simulation are listed in Table 4.1.

Parameter	Value
platform height	696 m
velocity	61 m/s
system bandwidth	100 MHz
chirp rate	1.0×10^{11} Hz/s
pulse period	1 ms
sampling rate	2 MSa/s
pulse repetition frequency	500 Hz
antenna azimuth beamwidth	0.95 degrees
antenna elevation beamwidth	45 degrees
antenna squint angle	0 degrees
baseline length	0.08 m
baseline tilting angle	5 degrees

Table 4.1: Numerical simulation parameters.

The range compressed image of the raw data in Figure 4.3 is shown in Figure 4.7. Careful inspection of this processed image reveals a slight blurring in the image,

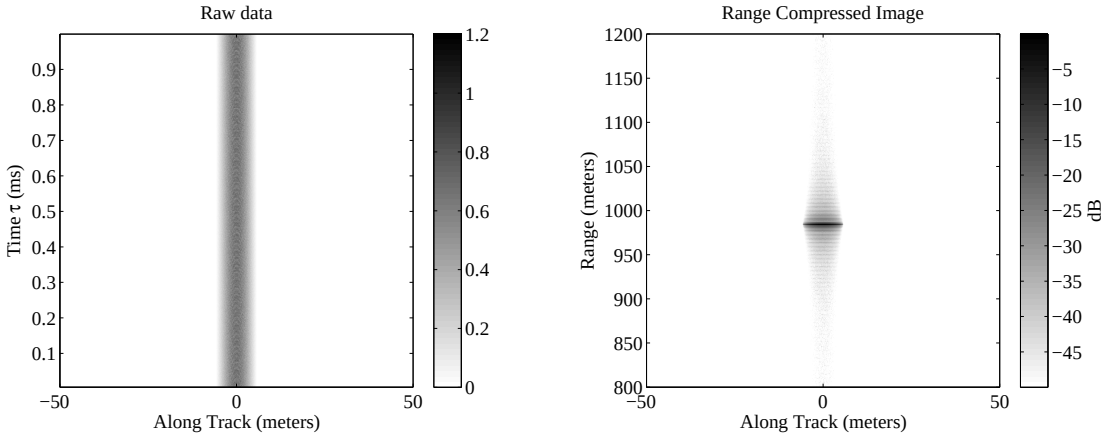

(a) (b)

Figure 4.6: Range compression simulation of a point scatterer. The scatterer is located at along-track position of zero. (a) The raw data. It is nonzero only in the narrow region around the zero along-track position because of the antenna beam pattern in the azimuth direction. (b) The range compressed image. The sidelobes of the point scatterer response can be seen from the image. (c) The range profile through the center of the image. The -13dB sidelobe can be seen.

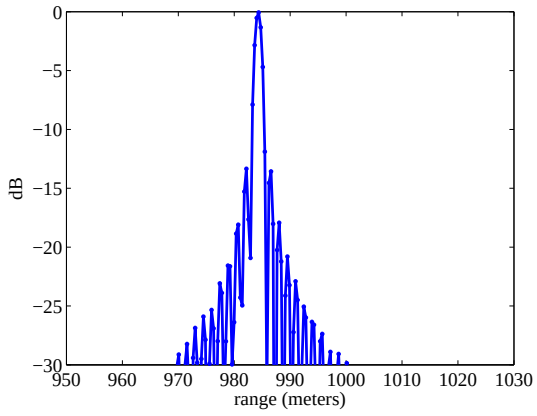

(c)

Figure 4.6: (Continued) Range compression simulation of a point scatterer. The scatterer is located at along-track position of zero. (a) The raw data. It is nonzero only in the narrow region around the zero along-track position because of the antenna beam pattern in the azimuth direction. (b) The range compressed image. The sidelobes of the point scatterer response can be seen from the image. (c) The range profile through the center of the image. The -13dB sidelobe can be seen.

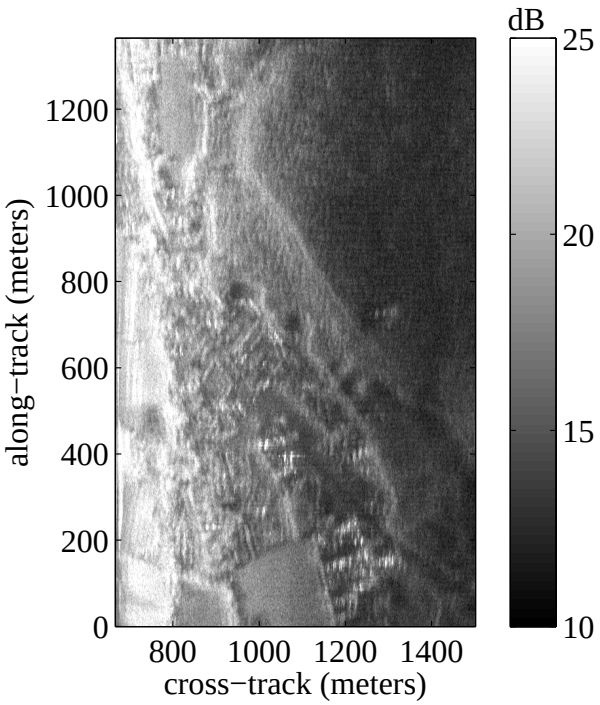

Figure 4.7: Result of range compression of one scene.

which means the image is out of focus. In other words, the point scatterer response of the system deviates from what is expected from Equation 4.6. It seems that the targets are showing two times in the range direction. This phenomenon is more distinguishable for the bright targets. A one-dimensional range profile including a bright scatterer (CrossTrack = 1012 m, AlongTrack = 420 m) is plotted in Figure 4.8. It shows two peaks instead of the one peak that would be expected for a point-like scatterer. The separation between the two peaks is 15 meters, which is consistent with the response for other bright targets in the image, and indicates a systematic error.

It is expected that this phenomenon is caused by the nonlinearities of the system, which would be a problem for any chirp compression system. These nonlinearities may be caused by the frequency nonlinearity noted in the baseband signal (see Figure 3.2), and/or the phase nonlinearities of the RF frontend and the antennas. When

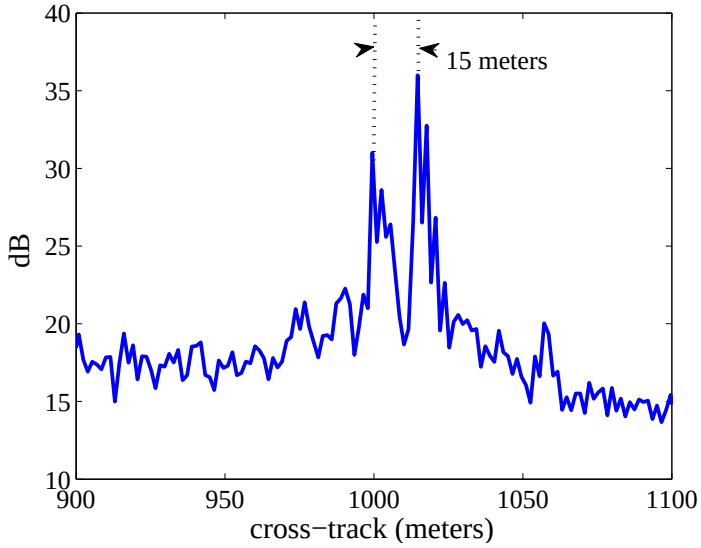

Figure 4.8: A range line profile at along-track position of 420 meters. The two peaks which correspond to the same scatterer are separated by 15 meters. A consistent pattern has been noted for other bright targets in the image.

nonlinearity occurs, the de-chirping output will not be the exact form of Equation 4.1, it will have a phase error. A diagram illustrating the nonlinearity issue is shown in Figure 4.9.

4.2 Phase Error Correction

It is necessary to remove the nonlinearities in the raw data before proceeding to the next step of data processing. If the specific form of the nonlinearity or the phase error is known as a prior knowledge, then it will be straightforward to implement a filter to cancel the nonlinearity effects. The raw data distorted by a phase error can be expressed as

$$s_e(\tau, t; R_0) = A_0 a_r(\tau - \frac{2R(t;R_0)}{c}) a_a(t - t_c) \cos\Big(\omega_b(t)\tau - \frac{2\omega'_{LO}R(t;R_0)}{c} - \frac{\omega_b(t)R(t;R_0)}{c} + \phi_e(\tau) + \phi_3\Big), \tag{4.7}$$

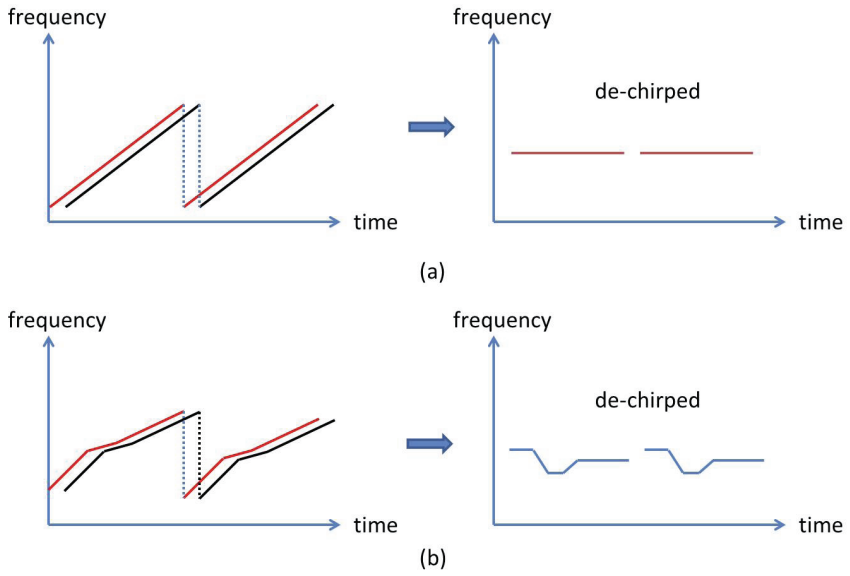

Figure 4.9: A diagram illustrating the nonlinearity issue for the response of the system to a point scatterer. (a) The de-chirping result of FMCW signal without nonlinearity. (b) The de-chirping result when the FMCW signal is affected by nonlinearities. The output has a frequency variation instead of the single-tone that would be expected for such a scatterer.

where the subscript e of the signal $s(\cdot)$ denotes the existence of distortion from a phase error $\phi_e(\tau)$.

However, the specific type of the phase error $\phi_e(\tau)$ may not be known in advance, since it can be caused from some sources which are not easy to characterize, such as platform movement or RF interference. Even though the nonlinearity can be characterized, its accuracy is limited by the hardware setup, the signal-to-noise ratio, and the method used for calibration. In such a scenario, the phase error $\phi_e(\tau)$ can be estimated from the data, which may provide a more reliable version of the phase error.

Estimation of the phase error in the along-track dimension has been investigated in the circumstance of SAR image auto-focusing. Among the different methods, the phase gradient algorithm (PGA) [23] is capable of estimating the phase error from data without knowing its specific form. The idea of PGA is that the derivative of the

phase error term $\phi_e(\tau)$ can be estimated from the point scatterer response, which can be extracted from the bright scatterers in each range line. Although the auto-focusing algorithm is originally used for phase error estimation in the along-track dimension, it can be adapted to the range dimension easily.

For the derivation such as the one given in [23], it is convenient to write the returned signal as a complex exponential, given by

$$\begin{aligned} s_e(\tau, t; R_0) =& A_1 a_r(\tau - \frac{2R(t;R_0)}{c}) a_a(t - t_c) \\ & \cdot \exp\left\{ j\big(\omega_b(t)\tau + \phi(t;R_0)\big)\right\} \cdot \exp\left\{ j\phi_e(\tau)\right\} , \end{aligned} \tag{4.8}$$

in which

$$\phi(t;R_0) = -\frac{2\omega_{LO}^{'} R(t;R_0)}{c} - \frac{\omega_b(t) R(t;R_0)}{c} . \tag{4.9}$$

The result of range compression will not change since only the positive frequency spectrum is kept and is the same for (4.7) and (4.8). The derivative of (4.8) with respect to τ is given by

$$\frac{\partial s_e(\tau, t; R_0)}{\partial \tau} = j\big(\omega_b(t) + \frac{\partial \phi_e(\tau)}{\partial \tau}\big) s_e(\tau, t; R_0) . \tag{4.10}$$

Hence, the derivative of the phase error term, $\frac{\partial \phi_e(\tau)}{\partial \tau}$, can be obtained by multiplying the left and right sides of (4.10) with $s_e^*(\tau, t; R_0)$, then taking the imaginary part, as in

$$\frac{\partial \phi_e(\tau)}{\partial \tau} = \frac{\mathrm{Im}[\frac{\partial s_e(\tau,t;R_0)}{\partial \tau} s_e^*(\tau, t; R_0)]}{|s_e(\tau, t; R_0)|^2} - \omega_b(t) . \tag{4.11}$$

This shows that the derivative of the phase error term can be accurately derived from the point scatterer response $s_e(\tau, t; R_0)$. However, for real data, such as shown in Figure 4.7, there may not be any point scatterers available. Hence, the point scatterer response $s_e(\tau, t; R_0)$ is not immediately available, and needs to be determined from the data. This can be accomplished in the range compressed image, in which those

bright scatterers will be taken to be the "point like" scatterers. The responses of these "point like" scatterers are used as an approximation to the range compression result of $s_e(\tau, t; R_0)$. Note that in a range compressed image, which is obtained through the Fourier transform, a point scatterer can be expressed as a sinc function (see Equation 4.6) if there is no phase error. If there exists a phase error, the ideal response of sinc function will convolve with the spectrum of the phase error in the frequency domain

$$S_e(f, t; R_0) = S(f, t; R_0) \otimes_f \Phi_e(f), \tag{4.12}$$

where $S_e(f, t; R_0)$ is the spectrum of the point scatterer response with a systematic phase error, $S(f, t; R_0)$ is the ideal spectrum of the point scatterer response, $\Phi_e(f)$ is the spectrum of the phase error term $e^{j\phi_e(\tau)}$, and $\otimes_f$ denotes convolution in the frequency domain. The effect of this convolution is a broadening of the main lobe of the sinc function or multiple peaks in the case of high frequency phase error. However, if the bandwidth of $\Phi_e(f)$ is small, the point scatterer response can be still extracted from the spectrum.

In the range compressed image, the brightest scatterers are found for each range line and then each range line is circularly shifted such that the brightest scatterers are at the center of the range line. The extraction of the brightest scatterers is accomplished by multiplying the range compressed data with a window function centering at the brightest scatterers, as in

$$S_{ow}(f, t; R_0) = W(f - f_{mid}) S(f - (f_{mid} - f_b), t; R_0) \otimes_f \Phi_e(f), \tag{4.13}$$

where f_{mid} is the frequency at the center and f_b is the frequency of the brightest scatterer of the i^{th} range line. The window $W(f)$ also removes the spectrum outside the bright scatterer spectrum, which can be considered here as a noise source for the estimation.

In practice, the error of estimation can be further decreased by calculating the average of the responses over all of the lines,

$$\frac{\partial \widehat{\phi_e(\tau)}}{\partial \tau} = \frac{\sum_i \mathrm{Im}[\frac{\partial s_{e,i}(\tau,t;R_0)}{\partial \tau} s^*_{e,i}(\tau,t;R_0)]}{\sum_i |s_{e,i}(\tau,t;R_0)|^2}\,, \tag{4.14}$$

in which, the constant term is neglected, since only higher order phase errors are of interest.

The general steps of phase error estimation are summarized in Figure 4.10. The first step is to take the Fourier transform along the range dimension of the raw data, and only keep the spectrum with positive frequency components. The second step is circularly shifting the brightest scatterer of each range line to the center. The third step is windowing around the bright scatterers. A large window size can be used initially and then decreased iteratively until the estimated phase gradient converges. The fourth step is the estimation of the phase gradient, using (4.14).

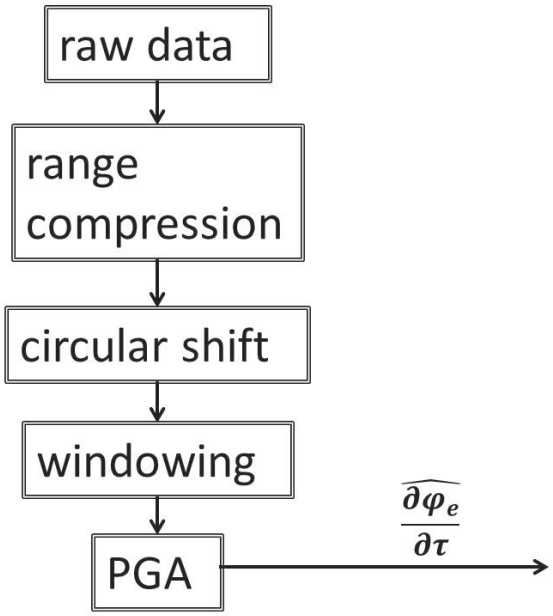

Figure 4.10: Processing steps of phase error estimation using phase gradient algorithm.

Once the phase gradient is obtained, the phase error term $\phi_e(\tau)$ can be calculated from the integration of (4.14). It should be noted that any constant and linear trend in the estimated phase error $\widehat{\phi_e(\tau)}$ should be removed. The whole process is iterated with decreasing window size. Finally, the raw data can be corrected by multiplying the phase error by $\exp\left\{-j\widehat{\phi_e(\tau)}\right\}$, as in

$$\begin{aligned} s_c(\tau, t; R_0) =& A_0 a_r(\tau - \frac{2R(t;R_0)}{c}) a_a(t - t_c) \\ & \cdot \exp\left\{j\big(\omega_b(t)\tau + \phi(t;R_0)\big)\right\} \\ & \cdot \exp\left\{j(\phi_e(\tau) - \widehat{\phi_e(\tau)})\right\} \\ \simeq& A_0 a_r(\tau - \frac{2R(t;R_0)}{c}) a_a(t - t_c) \\ & \cdot \exp\left\{j\big(\omega_b(t)\tau + \phi(t;R_0)\big)\right\}, \end{aligned} \tag{4.15}$$

where the subscript c in s_c denotes the corrected signal.

The result of phase error correction from Figure 4.7 is shown in Figure 4.11, and the estimated phase error is shown in Figure 4.12. It can be seen that the image does not look blurred, and the estimated phase error shows a high-frequency variation, which is what caused the scatterers to appear two times in the original image.

4.3 Azimuth Fourier Transform

The two dimensional signal is now in the two-dimensional domain of range, R, and azimuth time, t, as shown in (4.6), and needs to be converted to the range-Doppler domain by the Fourier transform in the azimuth time domain, such that a matched filter can be implemented in the frequency domain. Since there is not any closed-form expression for the Fourier transform of (4.6), the principle of stationary phase (POSP) [24] can be used to get a close approximation to the Fourier transform as long as the time-bandwidth product is sufficient large, e.g. the product of synthetic

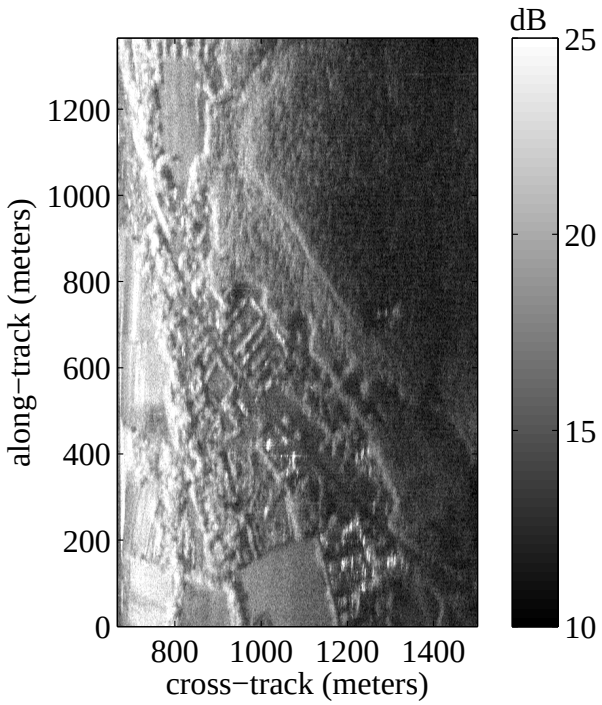

Figure 4.11: The result of phase error correction.

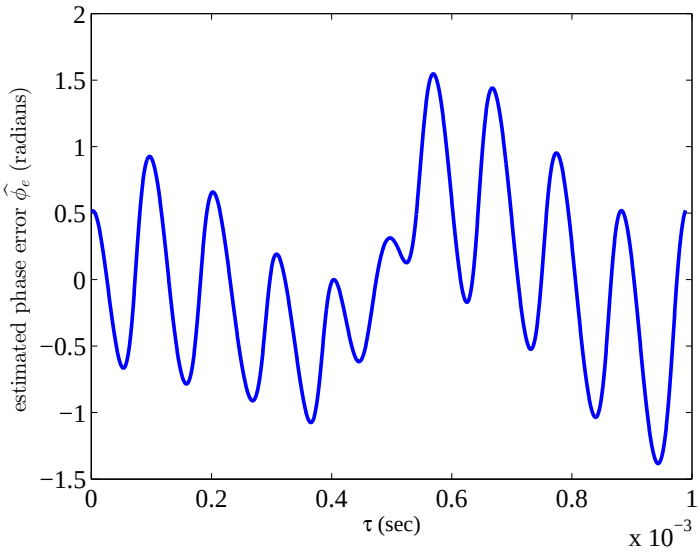

Figure 4.12: The estimated phase error $\hat{\phi}_e$.

aperture time, T, and the Doppler bandwidth, BW_D, $T \cdot BW_D \approx 100$; which for the UMass Ka-band system $T \cdot BW_D = 75$ is in the middle range.

The Fourier transform of the range-azimuth signal can be written as

$$S(r, f_t; R_0) = \int_t s(r, t; R_0)\, e^{-j2\pi f_t t}\, dt. \tag{4.16}$$

The phase of the integrand in (4.16) is the sum of the phase of $s(r, t; R_0)$ (as in (4.6)) and the phase of the Fourier basis $e^{-j2\pi f_t t}$, and is written as

$$\theta(t) = -\frac{\pi}{\delta r}(r - R(t; R_0)) - \frac{4\pi R(t; R_0) f_{LO}^{'}}{c} - 2\pi f_t t \tag{4.17}$$

where,

$$R(t; R_0) = \sqrt{R_0^2 + v^2 t^2}. \tag{4.18}$$

From the expression in (4.17), the derivative of $\theta(t)$ with respect to t is given as

$$\begin{aligned} \frac{d\theta(t)}{dt} =& \frac{\pi}{\delta r}\frac{dR(t; R_0)}{dt} - \frac{4\pi f_{LO}^{'}}{c}\frac{dR(t; R_0)}{dt} - 2\pi f_t \\ &= \pi(\frac{1}{\delta r} - \frac{4f_{LO}^{'}}{c})\frac{v^2 t}{\sqrt{R_0^2 + v^2 t^2}} - 2\pi f_t. \end{aligned} \tag{4.19}$$

The stationary point can be found by letting $\frac{d\theta}{dt} = 0$, then the relation between azimuth frequency, f_t and azimuth time, t is written as

$$f_t = \frac{1}{2}(\frac{1}{\delta r} - \frac{4f_{LO}^{'}}{c})\frac{v^2 t}{\sqrt{R_0^2 + v^2 t^2}}\,, \tag{4.20}$$

or, after inverting for time,

$$t = -\frac{2R_0 f_t}{v\sqrt{\left(\frac{1}{\delta r} - \frac{4f_{LO}^{'}}{c}\right)^2 v^2 - 4f_t^2}}\,. \tag{4.21}$$

Note that in (4.20),

$$\frac{1}{\delta r} - \frac{4f_{LO}^{'}}{c} = -\frac{4f_{LO}^{'} - 2B}{c} = -\frac{4(f_{LO} - f_0 - \frac{B}{2})}{c}, \tag{4.22}$$

and the center frequency of the modulated chirp, $f_c = f_{LO} - f_0 - \frac{B}{2}$, hence $\frac{1}{\delta r} - \frac{4f'_{LO}}{c} = -\frac{4f_c}{c}$. Then (4.20) and (4.21) can be re-written as,

$$f_t = -\frac{2v^2 f_c t}{c\sqrt{R_0^2 + v^2 t^2}} \tag{4.23}$$

and

$$t = -\frac{cR_0 f_t}{2f_c v^2 \sqrt{1 - \frac{c^2 f_t^2}{4f_c^2 v^2}}}\,. \tag{4.24}$$

The azimuth Fourier transform can then be obtained by substituting (4.24) into the integrand of (4.16) to get

$$\begin{aligned} S(r, f_t; R_0) &= A_1 T\, A_a(f_t - f_{tc}) \operatorname{sinc}\left(\frac{1}{\delta r}\big(r - R(f_t; R_0)\big)\right) \\ &\quad \cdot \exp\left\{-j\frac{\pi}{\delta r} r\right\} \cdot \exp\left\{-j\frac{4\pi R(f_t; R_0) f_c}{c}\right\} \\ &\quad \cdot \exp\left\{j\frac{\pi c R_0 f_t^2}{f_c v^2 \sqrt{1 - \frac{c^2 f_t^2}{4f_c^2 v^2}}}\right\} \\ &= A_1 T\, A_a(f_t - f_{tc}) \operatorname{sinc}\left(\frac{1}{\delta r}\big(r - R(f_t; R_0)\big)\right) \\ &\quad \cdot \exp\left\{-j\frac{\pi}{\delta r} r\right\} \cdot \exp\left\{-j\frac{4\pi R(f_t; R_0) f_c}{c}\big(1 - \frac{c^2 f_t^2}{4f_c^2 v^2}\big)\right\} \\ &= A_1 T\, A_a(f_t - f_{tc}) \operatorname{sinc}\left(\frac{1}{\delta r}\big(r - R(f_t; R_0)\big)\right) \\ &\quad \cdot \exp\left\{-j\frac{\pi}{\delta r} r\right\} \cdot \exp\left\{-j\frac{4\pi R_0 f_c}{c}\sqrt{1 - \frac{c^2 f_t^2}{4f_c^2 v^2}}\right\} \end{aligned} \tag{4.25}$$

in which f_{tc} in the envelope A_a is the frequency corresponding to the beam center crossing time t_c, as shown in Figure 4.13. The range migration in the frequency domain, expressed as $R(f_t; R_0)$ is

$$R(f_t; R_0) = \frac{R_0}{\sqrt{1 - \frac{c^2 f_t^2}{4f_c^2 v^2}}}\,. \tag{4.26}$$

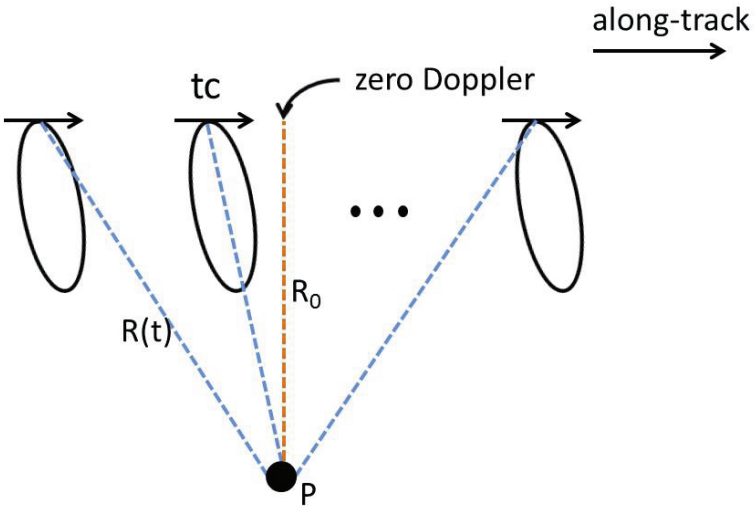

(a)

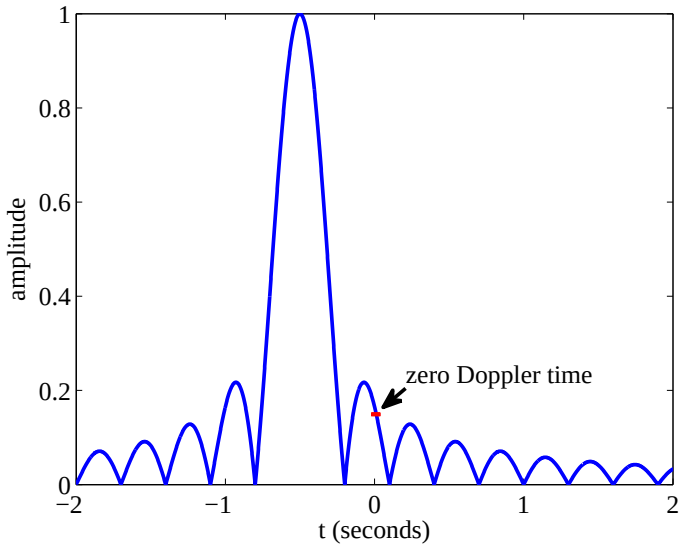

(b)

Figure 4.13: (a) Relative position between the antenna and the scatterer. Time t_c is beam center crossing time. (b) Example azimuth antenna pattern in time domain with $t_c = -0.5$s.

The range migration in the sinc function can be accommodated by interpolating in a process called range cell migration correction (RCMC). After RCMC, the signal in (4.25) becomes

$$
\begin{aligned}
S(r, f_t; R_0) =& A_1 T\, A_a(f_t - f_{tc}) \operatorname{sinc}\left(\frac{1}{\delta r}(r - R_0)\right) \\
& \cdot \exp\left\{-j\frac{\pi}{\delta r} r\right\} \cdot \exp\left\{-j\frac{4\pi R_0 f_c}{c}\sqrt{1 - \frac{c^2 f_t^2}{4 f_c^2 v^2}}\right\} .
\end{aligned}
\tag{4.27}
$$

4.4 Doppler Centroid Estimation

The azimuth spectrum of the signal is given in Equation 4.27. Once this is known, it is straightforward to implement the matched filter to compensate for its nonlinear phase. However, due to the discrete nature of the azimuth data, the spectrum is shifted by multiples of the along-track sampling frequency (or equivalently, the pulse repetition frequency, PRF), shown in Figure 4.14.

Before performing the azimuth compression, the Doppler centroid needs to be estimated from data in order to infer the antenna squint angle with respect to the direction of travel. For a point scatterer, the Doppler centroid is the frequency at which the azimuth spectrum reaches a maximum. Figure 4.14(a) shows how the Doppler bandwidth is limited by the antenna pattern, and Figure 4.14(b) shows the effect of sampling in the azimuth time domain. It can be seen that the magnitude of the spectrum has a maximum at the Doppler centroid. Therefore the Doppler centroid for a particular scatterer can be estimated from the maximum of its spectrum magnitude. However, as shown in Figure 4.14(b), due to the sampling in azimuth time, the only visible part of the spectrum is between $[-\frac{F_s}{2}, \frac{F_s}{2}]$, where F_s is sampling frequency in azimuth dimension and equals to PRF. Hence, the true Doppler centroid can be decomposed into two parts

$$
f_{dc}(r,t) = f_{dc,b}(r,t) + M(r,t) \cdot F_s;\ M \in \mathcal{Z} \quad , \tag{4.28}
$$

in which $\mathcal{Z}$ is the set of integers, $M(r,t)$ is called the ambiguity number and $f_{dc,b}(r,t)$ is the baseband Doppler centroid which can be directly estimated from the spectrum.

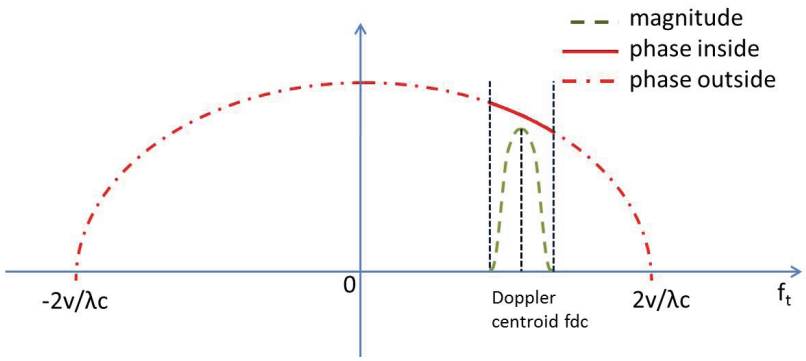

(a)

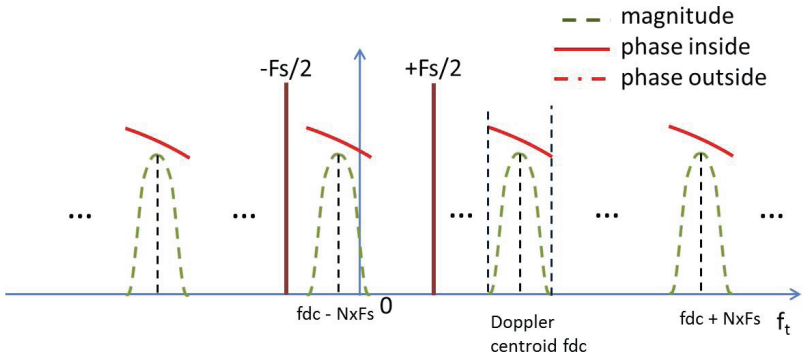

(b)

Figure 4.14: An illustration of the azimuth spectrum. (a) The dash-dotted curve is the phase if the antenna is omni-directional in azimuth direction. The solid curve is the phase if the antenna has a beam pattern as the dashed curve. (b) If sampled in the azimuth direction, its spectrum is shifting by multiples of sampling frequency F_s and only the spectrum between $[-\frac{F_s}{2}, \frac{F_s}{2}]$ is observed.

Note that $f_{dc}(r,t)$ is a two-dimensional function of the range, r, and the azimuth time, t.

While the baseband Doppler centroid can be estimated from the azimuth spectrum, as shown later in this section, the ambiguity number M can only be estimated with the aid of information about the platform attitude. That is, parameters of platform yaw and pitch angles, which affect the pointing direction of the antenna beam with respect to the direction of platform motion. The Doppler centroid can be found from the Doppler velocity at the beam center crossing time, t_c

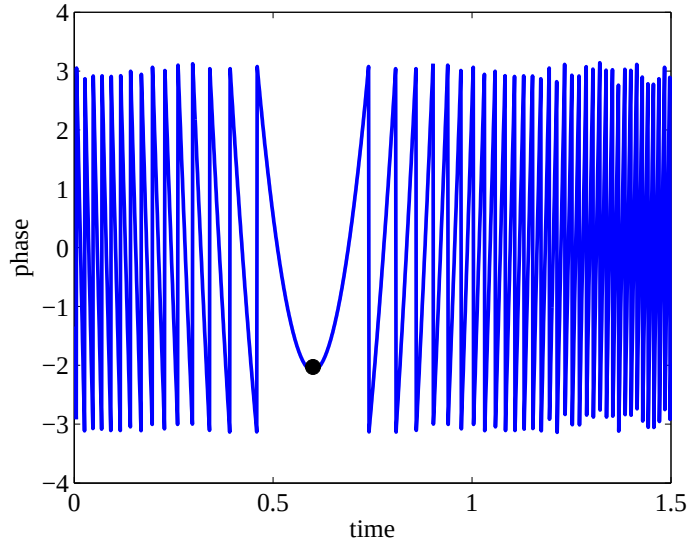

Figure 4.15: Phase of radar echo versus time.

$$f_{dc} = \frac{2v_r}{\lambda_c} = \frac{2\,v \sin\theta_{sq}}{\lambda_c} \quad , \tag{4.29}$$

where v_r is the radial velocity between the radar and the scatterer, θ_{sq} is the squint angle shown in Figure 4.16, and (4.29) is the projection of the platform velocity v onto the direction of antenna main lobe.

The geometry of the radar and a point scatterer A is shown in Figure 4.16. The squint angle, θ_{sq}, can be expressed in terms of the yaw angle, θ_y, the pitch angle, θ_p, the altitude of the radar, H, the scatterer height, h, and the slant range, R, given by

$$\sin\theta_{sq} = \frac{-H'}{R}\cos\theta_y\, tan\theta_p - \sin\theta_y\sqrt{1-(\frac{H'}{R})^2\frac{1}{\cos^2\theta_p}} \quad , \tag{4.30}$$

in which $H' = H - h$.

Hence the Doppler centroid can be derived by substituting (4.30) into (4.29) to get

$$f_{dc,geom}(\theta_y,\theta_p,H',R) = \frac{-2v}{\lambda_c}\left(\frac{H'}{R}\cos\theta_y\tan\theta_p + \sin\theta_y\sqrt{1-(\frac{H'}{R})^2\frac{1}{\cos^2\theta_p}}\right). \tag{4.31}$$

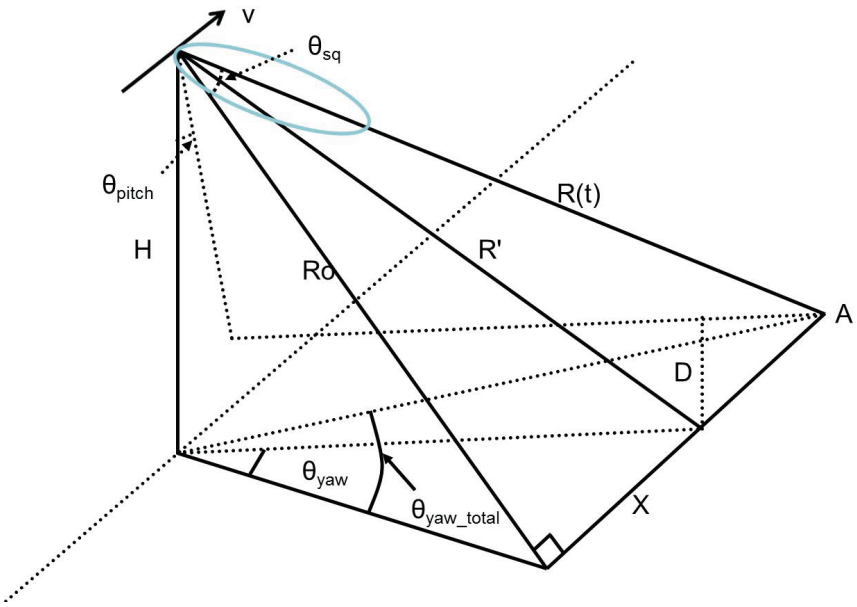

Figure 4.16: The geometry of the radar and the scatterer A. The antenna beam is represented by an ellipse. R(t) is the instantaneous slant range, and R_0 is the closest approach corresponding to the zero-Doppler time.

The parameters, θ_y and θ_p, refering to the yaw and pitch angles, and the platform height, H, are measured by the IMU and GPS. Often the measurement accuracy of these parameters is not good enough for the requirement of the Doppler centroid estimation. However, the calculated $f_{dc,geom}$ from the geometric model can be useful in estimating the ambiguity number M as in

$$M = \underset{N}{\operatorname{argmin}} \left| f_{dc,b} + N \cdot F_s - f_{dc,geom} \right|^2 , \tag{4.32}$$

in which, M is determined with the minimum square error (MSE) criterion. Although $f_{dc,geom}$ is not accurate, the tolerance of its error is also large, which is $\frac{F_s}{2}$ as illustrated in Figure 4.17. Hence an accurate estimation of M can be still achieved.

In addition to the yaw and pitch angles from the outputs of the IMU, the installation of the antenna may not be aligned perfectly with the platform. Hence, some offset angles are necessary to accurately model the ambiguity number and the antenna

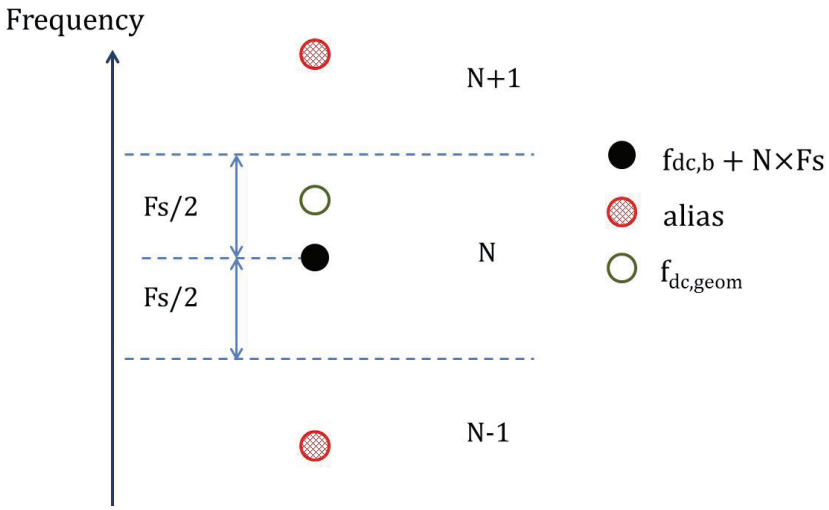

Figure 4.17: Determination of the ambiguity number M using the geometry model. The black circle represents the true Doppler centroid, and the red circles are its aliases. The calculated Doppler centroid $f_{dc,geom}$, represented as the white circle, will yield an accurate estimation of the ambiguity number as long as it is within $F_s/2$ of true Doppler centroid.

pointing direction which will be used in the geo-registration of the radar image. A model of the Doppler frequency shift that includes these errors is given by

$$f_{Dp}(\theta_y, \theta_{y\_os}, \theta_p, \theta_{p\_os}, H', R) = \frac{-2v}{\lambda}\Big(\frac{H'}{R}\cos(\theta_y + \theta_{y\_os})\tan(\theta_p + \theta_{p\_os}) + \sqrt{1 - (\frac{H'}{R})^2 \frac{1}{\cos^2(\theta_p + \theta_{p\_os})}}\sin(\theta_y + \theta_{y\_os})\Big). \tag{4.33}$$

The offset angles θ_{y_os} and θ_{p_os} can be obtained through measurement or calculations if the positions of the platform and the scatterers are known.

To estimate the baseband Doppler centroid $f_{dc,b}$ as the two-dimensional function in (4.28), the range compressed image can be divided into smaller blocks, and the corresponding Doppler centroid estimated for each block to generate of map of the Doppler centroid. The spectrums of all the range bins within one block are summed to decrease the noise. An example of the block division is shown in Figure 4.18, and

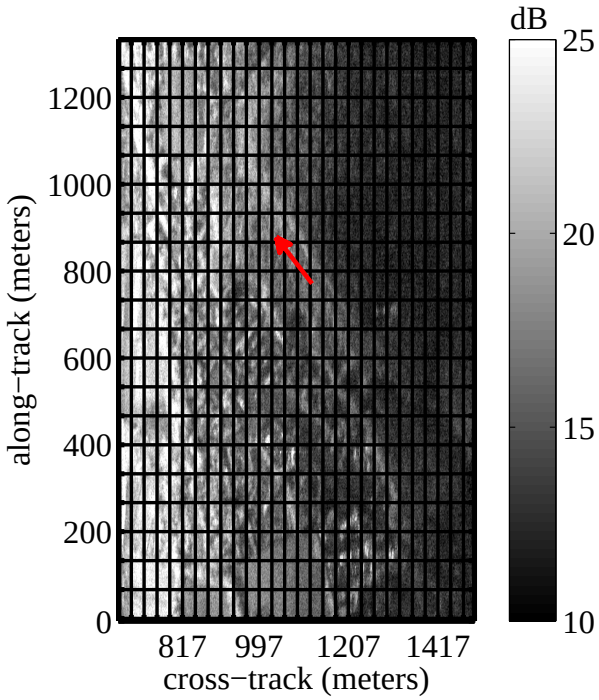

Figure 4.18: An example of block division of an range compressed image. The arrow points to a region where the Doppler spectrum is shown in Figure 4.19.

the spectrum corresponding to the block pointed by the arrow is shown in Figure 4.19.

It can be seen that the spectrum in Figure 4.19 is noisy and thus it is difficult to determine the location of the maximum. A power balancing filter [22] can be utilized to decrease the noise power. The filter is given as

$$F_{pb}(f_t) = \begin{cases} +1 & \text{if } 0 \leq f_t \leq F_s/2 \\ -1 & \text{otherwise} \end{cases} . \tag{4.34}$$

The output is the result of circular convolution between the power balancing filter and the summed block spectrum. For each output frequency, the filter integrates the right and the left side around its center. Hence, the noise power is decreased by integration, and the result will have a negative sloped zero-crossing at the point where the spectrum has a maximum. The resulting spectrum is shown in Figure

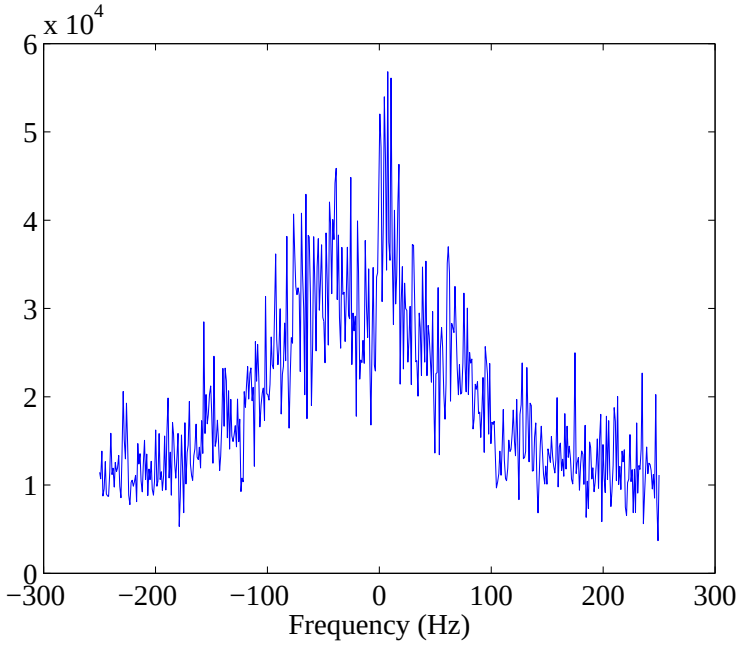

Figure 4.19: Spectrum of the cell pointed by an arrow in Figure 4.18.

4.20. However, it is possible, if not likely, that the result has more than one zero-crossing points caused by the noise or not any zero-crossing point if it happens to be at the frequency of $\pm\frac{PRF}{2}$. To solve the former problem, the noisy spectrum can be piecewisely fitted by a polynomial curve, as shown in Figure 4.20, thus the random fluctuations around the zero-crossing point can be eliminated. To solve the latter problem, the spectrum can be circularly shifted for a small amount of frequency, such that the zero-crossing point is not appearing at the edge of the frequency band.

The accuracy of the estimation of baseband Doppler centroid for each cell depends on the signal-to-noise ratio (SNR) and the homogeneity of the scene in a block. Typically, the estimated baseband Doppler centroid is noisy, shown in Figure 4.21. It can be seen that there are outlier points in the far range due to the low signal-to-noise ratio. The surface is also noisy along the azimuth direction. The two-dimensional Doppler centroid can be fitted with a polynomial surface to get a better estimation in a least square sense. The result of this fit is shown in Figure 4.22.

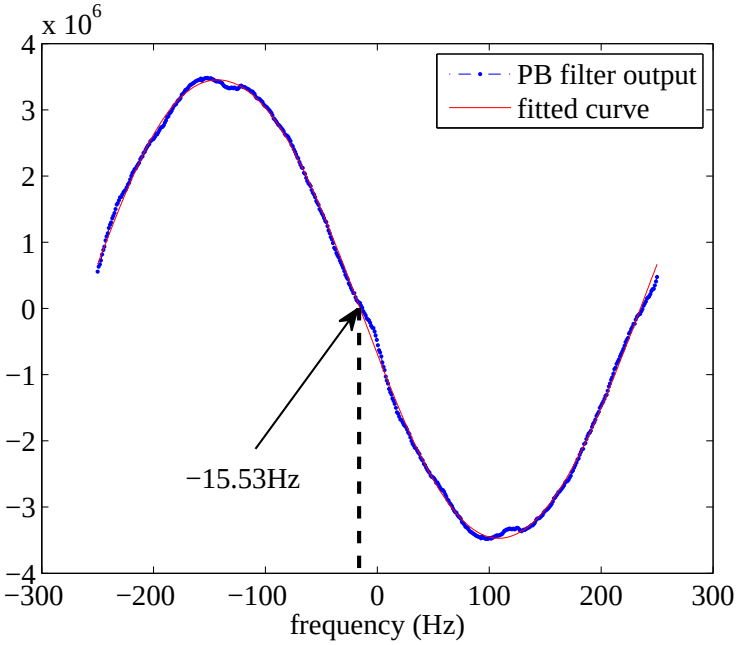

Figure 4.20: The resulting spectrum after applying the power balancing filter.

Now with the estimation of the baseband Doppler centroid $f_{dc,b}$ and the ambiguity number, M, the offset angles in the geometric model (Equation 4.31) can be further refined by comparing the estimated Doppler centroid, f_{dc}, and the one calculated from the geometric model, $f_{dc,geom}$. The final offset angles will have the minimum error between the two Doppler centroid estimates under the least square criterion.

The steps to estimate the Doppler centroid and the offset angles are summarized as

1. Determine the offset angles from direct measurements, or from calculations if the positions are known for selected targets and the platform.

2. Estimate the baseband Doppler centroid $f_{dc,b}$ from data and fit to a polynomial surface.

3. Determine the Doppler ambiguity number M for each $f_{dc,b}$.

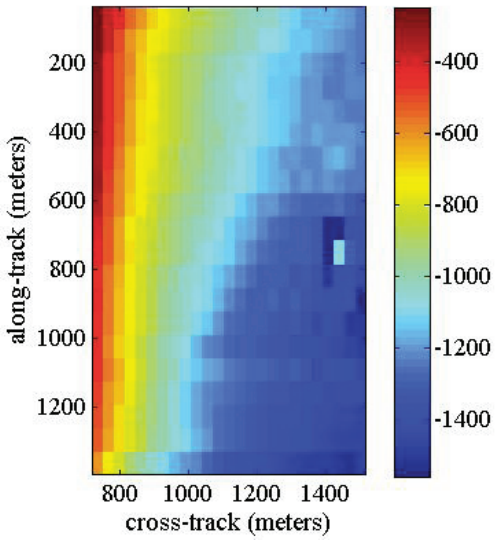

(a)

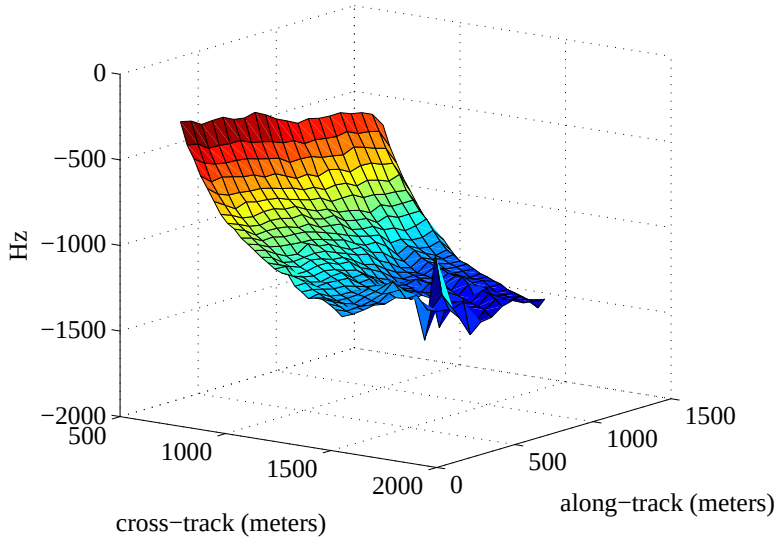

(b)

Figure 4.21: The estimated two-dimensional baseband Doppler centroid of Figure 4.18. (a) Two-dimensional view. (b) A surface view.

4. Refine the offset angles by minimizing the difference between the geometric model and the estimated Doppler centroid.

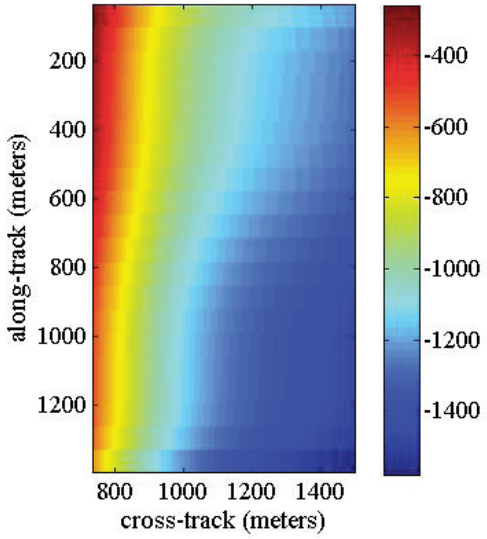

(a)

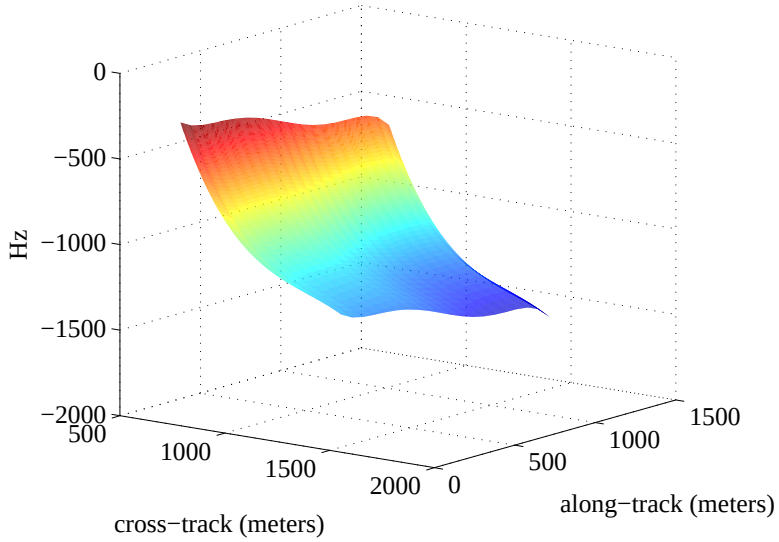

(b)

Figure 4.22: Polynomial fit of the two dimensional estimated Doppler centroid. 7th order polynomial fit in along-track direction, 3th order polynomial fit in cross-track direction.

4.5 Azimuth Compression

In azimuth compression, the nonlinearities in phase in the f_t domain, Equation 4.27, needs to be compensated by a matched filter. The part of phase in (4.27) related to f_t is

$$\phi(f_t) = -\frac{4\pi R_0 f_c}{c}\sqrt{1 - \frac{c^2 f_t^2}{4 f_c^2 v^2}} \quad . \tag{4.35}$$

The above equation can be expanded as a function of frequency in the neighborhood of the Doppler centroid, f_{tc}, and which is approximated as

$$\phi(f_t) \approx -\frac{4\pi R_0 f_c}{c}\left(\sqrt{1 - \left(\frac{f_{tc}}{f_{d\infty}}\right)^2} - \frac{(\frac{f_t}{f_{d\infty}})^2 - (\frac{f_{tc}}{f_{d\infty}})^2}{2\sqrt{1 - (\frac{f_{tc}}{f_{d\infty}})^2}}\right) \quad , \tag{4.36}$$

in which

$$f_{d\infty} = \frac{2v f_c}{c}, \tag{4.37}$$

is the Doppler frequency when the radar is at an infinite distance away from the scatterer, which corresponds to 90 degrees of squint angle, θ_{sq}.

Recalling that

$$f_{tc} = f_{d\infty}\sin(\theta_{sq,c}) \text{ and,} \tag{4.38}$$

$$f_t = f_{d\infty}\sin(\theta_{sq}) \tag{4.39}$$

Equation 4.36 can be further written as

$$\phi(f_t) \approx -\frac{4\pi R_0 f_c}{c}\left(\cos\theta_{sq,c} - \frac{\sin^2\theta_{sq} - \sin^2\theta_{sq,c}}{2\cos\theta_{sq,c}}\right) \quad , \tag{4.40}$$

where θ_{sq} is the instantaneous squint angle between the line of sight direction of the scatterer and the platform moving direction, and $\theta_{sq,c}$ is the squint angle at the time the antenna beam center is crossing the scatterer. For small squint angles of the beam center (< 10 degrees), (4.40) can be simplified by substituting $\theta_{sq} = cf_t/2vf_c$ and using the small argument approximation of sine function to get

$$\begin{aligned} \phi(f_t) &\approx -\frac{4\pi R_0 f_c}{c}\left(1 - \frac{\sin^2\theta_{sq}}{2}\right) \\ &= -\frac{4\pi R_0 f_c}{c}\left(1 - \frac{1}{2}(\frac{cf_t}{2vf_c})^2\right) \quad . \end{aligned} \tag{4.41}$$

Hence, the matched filter is given as

$$M_{az}(f_t; R_0) = \exp\left\{-j\pi \frac{cR_0}{2v^2 f_c} f_t^2\right\}, \tag{4.42}$$

where the envelope can be approximated as a constant if the antenna's azimuth pattern is considered as a weighting window in the azimuth direction. In the frequency domain, the azimuth compression is accomplished with just one vector multiplication for a given range, hence, the computation is more efficient than the time domain matched filter.

Initially, a matched filter for the zero Doppler is first designed and then it is circularly shifted so that the filter center frequency is equal to the frequency of baseband Doppler centroid. After compression in the frequency domain, the signal in (4.27) becomes

$$S(r, f_t; R_0) = A_1 T\, A_a(f_t - f_{tc}) \operatorname{sinc}\left(\frac{r - R_0}{\delta r}\right) \exp\{-j\frac{\pi}{\delta r} r\} \exp\{-j\frac{4\pi R_0 f_c}{c}\}. \tag{4.43}$$

The inverse Fourier transform of (4.43) is

$$s(r, t; R_0) = A_1 T\, p_a(t) \operatorname{sinc}\left(\frac{r - R_0}{\delta r}\right) \exp\left\{-j\frac{\pi}{\delta r} r\right\} \exp\{-j\frac{4\pi R_0 f_c}{c}\} \exp\{j2\pi f_{tc} t\}, \tag{4.44}$$

in which $p_a(t)$ is the inverse Fourier transform of the frequency domain envelope, $A_a(f_t)$. The frequency shift of the envelope, f_{tc}, becomes a linear phase term in the time domain, $\exp\{j2\pi f_{tc} t\}$, after the inverse Fourier transform.

A compressed SAR image is shown in Figure 4.23, where the improvement of along-track resolution compared to Figure 4.11 can be observed. For a large squint angle case, the approximation in (4.41) cannot be used, and the higher order terms in (4.40) need to be included. Since most of the data processed here fell within the small argument approximation, this issue is not addressed here.

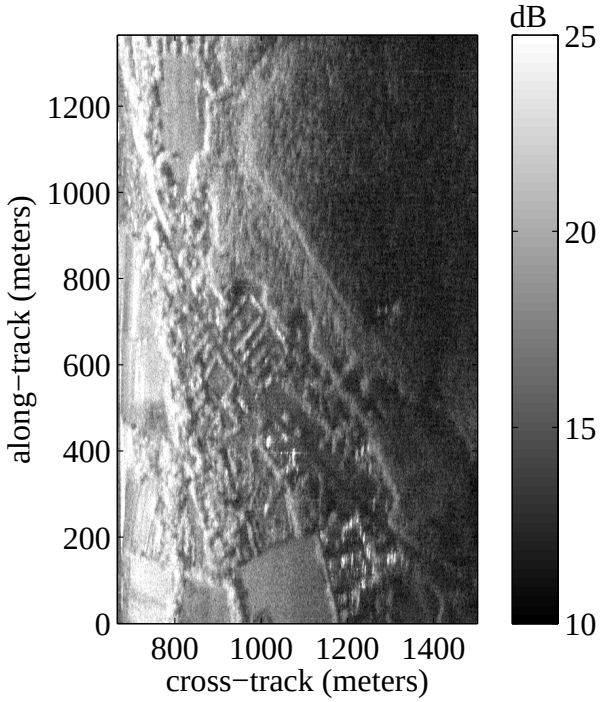

(a)

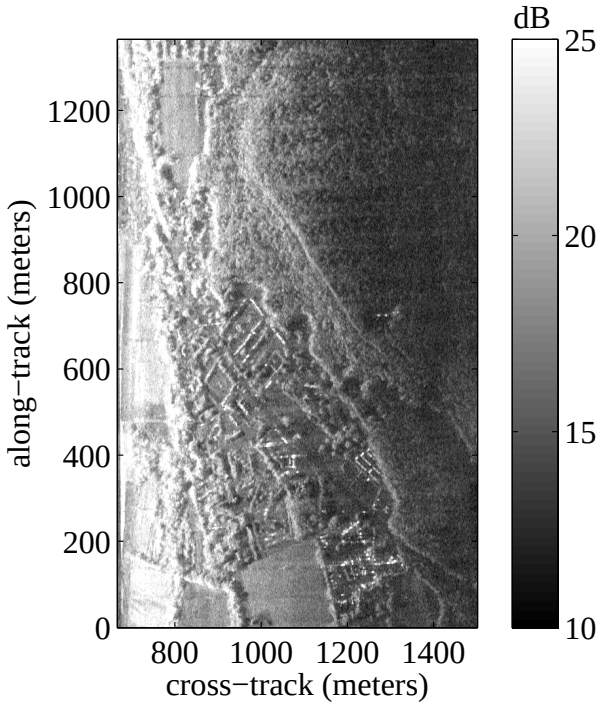

(b)

Figure 4.23: (a) The magnitude image before azimuth focusing. (b) The SAR image compressed after range and azimuth filtering.

CHAPTER 5

MOTION EFFECTS AND COMPENSATION

During the Doppler processing of the SAR data, the trajectory of the platform is assumed to be a straight line, and its speed is constant. Based on these assumptions, the matched filter in the Doppler processing has a simple form. In the practical situation however, a discrepancy exists between the real platform trajectory and the straight-line trajectory. For airborne platforms, this is more crucial than for satellite platforms due to atmospheric turbulence and the presence of cross-winds. The trajectory discrepancy will cause range-dependent phase errors to the processed images. The discrepancy from the ideal trajectory has two forms, i.)the translational displacement of the radar phase center, and ii.) the rotary movement of the platform.

The global positioning system (GPS) and inertial measurement unit (IMU) are mounted on the platform in order to record the platform positions and attitude as a function of time. These data, combined with an accurate geometrical model, can be utilized for the compensation of motion induced phase errors. The accuracy and precision of the compensation depends on the quality of motion measurements which typically cannot meet the requirement of sub-wavelength accuracy. In such cases, the radar data may be used as an alternative to improve the accuracy.

Motion compensation (MOCO) has been studied extensively in the literature since the invention of SAR. Several different methods of MOCO have been proposed , such as: i.) use the direct measurements through IMU and GPS, and use of a motion model to compensate the trajectory deviations [25],[26]. ii.) the motion effects can be estimated directly from the radar data [27], iii.) utilize an auto-focusing algorithm,

such as the phase-gradient algorithm [23] to compensate for motion-induced phase deviation, or iv.) the phase retrieval method [28] is used to reconstruct the SAR image by minimizing a proper functional, which is based on the intensity square of the SAR image.

5.1 A General Forward Motion Model

In this section, a general forward model incorporating the platform motion is derived. If we assume that the transmitted pulse or waveform at azimuth time, t, is $s(t_r)$, where t_r is the range time (equivalently the fast time), then the received scattered signal from a point scatterer is

$$s_r(t) = a(t)s(t_r - \tau_d) \tag{5.1}$$

where τ_d is the time delay at time, t, and $a(t)$ is the amplitude at time t. Since the speed of light is much faster than the velocity of the platform, it is assumed to be not moving at this moment, hence t is usually taken as discrete values, with a constant sampling rate, $1/PRF$. For an FMCW radar, the typical transmitting signal has a waveform of linear frequency modulation, as in

$$s(t_r) = e^{j(2\pi f_0 t_r + \pi\beta t_r^2 + \phi_0)}, \tag{5.2}$$

where f_0 is the start frequency of the waveform, β is the frequency slope (chirp rate) and ϕ_0 is the phase offset. As described in chapter 4, the output of the de-chirping process, $s_{dc}(t, t_r)$, is given by

$$\begin{aligned} s_{dc}(t, t_r) =& s(t_r) \cdot a^*(t)s^*(t_r - \tau_d) \cdot e^{j2\pi f_c \tau_d} \\ =& a(t) \cdot e^{j(2\pi f_0 \tau_d - \pi\beta\tau_d^2 + 2\pi f_c \tau_d)} \cdot e^{j2\pi\beta\tau_d t_r}, \end{aligned} \tag{5.3}$$

where the term, $e^{j2\pi f_c \tau_d}$, is the phase delay associated with the carrier frequency, f_c. After the range compression, the two-dimensional time-domain signal, $s_{dc}(t, t_r)$, becomes a sinc function as shown in chapter 4. The magnitude and phase at the center of the sinc function is given by

$$s_{rc}(t) = a(t) \cdot e^{j\phi(t)}, \tag{5.4}$$

where

$$\phi(t) = 2\pi f_0 \tau_d - \pi \beta \tau_d^2 + 2\pi f_c \tau_d. \tag{5.5}$$

Both the amplitude, $a(t)$, and the phase, $\phi(t)$, is a function of the radar attitude and position. The amplitude, $a(t)$, depends on the specific antenna gain in the line of sight direction of the scatterer, is modeled as

$$a(t) = \alpha G_{los}^2(t) \tag{5.6}$$

where $G_{los}(t)$ is the antenna gain in the line of sight direction and α is a constant depending on the transmitting power, the radar wavelength and the instantaneous range, which is assumed to be a constant due its relatively small variation. The square of the gain comes from the two-way propagation of the electromagnetic wave, and here we assume the transmit and receive antennas are close to each other such that the gain is the same.

The antenna gain, $G_{los}(t)$, depends on the radar beam pointing direction and the scatterer location. It can be expressed as

$$G_{los}(t) = G_{los}\left(\, \theta_{sr}(t), \phi_{sr}(t) \,\right), \tag{5.7}$$

where $\theta_{sr}(t)$, and $\phi_{sr}(t)$ are the elevation angle and the azimuth angle of the scatterer relative to the radar beam coordinate system. The phase, $\phi(t)$, which is a function

of the two-way time delay, τ_d, depends on the radar position for a given scatterer. Hence, the range compressed signal, $s_{rc}(t)$, is a function of the radar platform motion parameters. Its amplitude directly relates to the attitude parameter, i.e., yaw, roll, pitch angles, and its phase directly relates to the position parameters, i.e., the latitude, longitude, and altitude. If the trajectory and/or the attitude of the radar deviates from the nominal one, i.e., its position and/or its attitude parameters deviates, the range compressed signal $s_{rc}(t)$ will consequently deviates from its nominal form. Figure 5.1 illustrates the effect of trajectory and attitude deviation.

The antenna gain, $G_{los}(t)$, at time, t, is determined by the line-of-sight direction from the scatterer to the radar phase center and radar boresight direction, as illustrated in Figure 5.2. The orientation of the radar coordinate system can be determined with a 3D rotation in the global coordinate system, as illustrated in Figure 5.3. The specific form of the 3D rotation can be determined from the attitude parameters of the platform, which is yaw, pitch and roll angle, as shown in [29]

$$\overline{\overline{R}} = \overline{\overline{R}}_X(\psi_r)\overline{\overline{R}}_Y(\psi_p)\overline{\overline{R}}_Z(\psi_y) \tag{5.8}$$

where R is the 3D rotation, $\overline{\overline{R}}_X$, $\overline{\overline{R}}_Y$ and $\overline{\overline{R}}_Z$ are 3×3 matrices representing 1D rotations with respect to XYZ axes by a particular angle, which is given by the arguments, ψ_r, ψ_p and ψ_y representing the roll, pitch and yaw angle. For example, $\overline{\overline{R}}_Z(\psi_y)$ represents the rotation with respect to Z axis with an amount of ψ_y. The rotation matrices are given by

$$\overline{\overline{R}}_X(\theta) = \begin{pmatrix} 1 & 0 & 0 \\ 0 & \cos\theta & -\sin\theta \\ 0 & \sin\theta & \cos\theta \end{pmatrix} \tag{5.9}$$

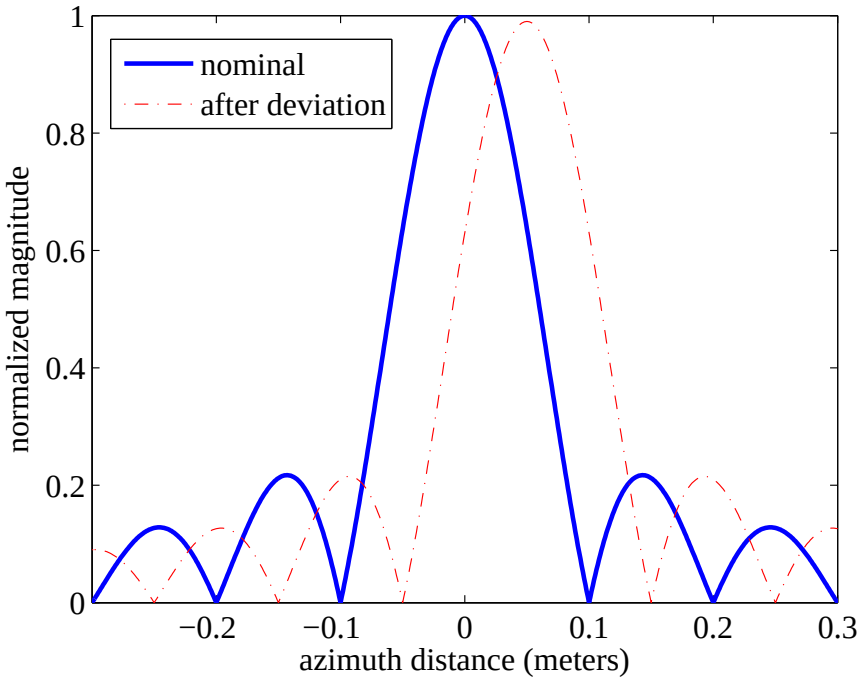

(a)

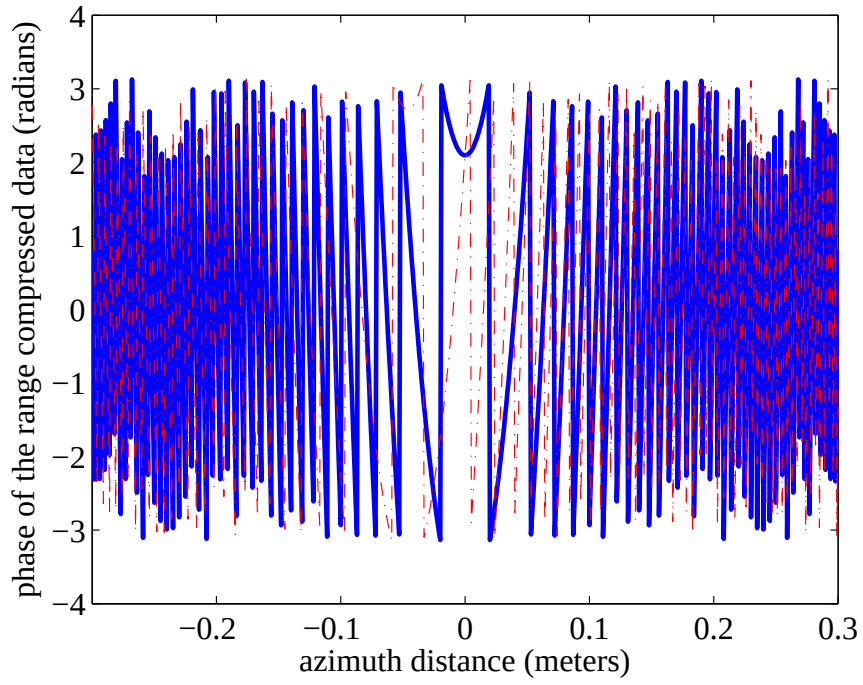

(b)

Figure 5.1: The effect of trajectory and attitude deviation on the range compressed signal $s_{rc}(t)$ for a point scatterer. (a) The effect of yaw angle variation on the amplitude. (b) The effect of linear slant range variation of 0.1 meter on the phase.

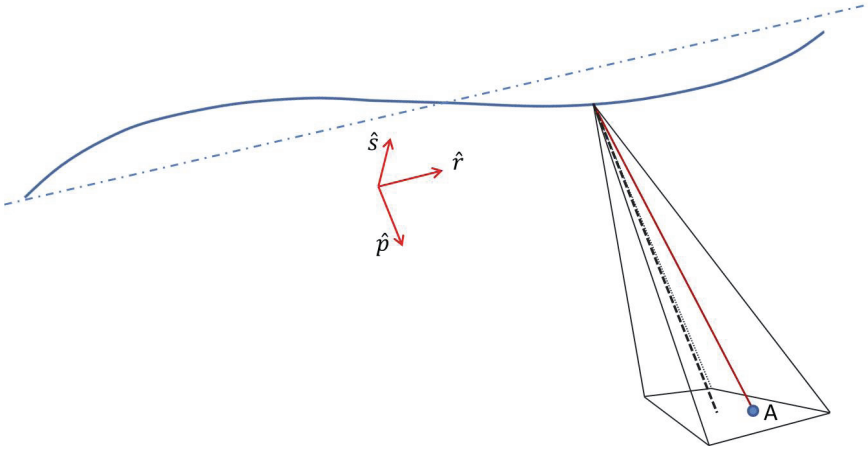

Figure 5.2: The antenna gain, $G_{los}(t)$, is determined by the line-of-sight direction of scatterer A and the radar antenna boresight direction (dashed line). The coordination system $\hat{r}\hat{s}\hat{p}$ is the radar coordination system, where $\hat{r}$ and $\hat{s}$ are the antenna azimuth and elevation direction, $\hat{p}$ is the antenna boresight direction.

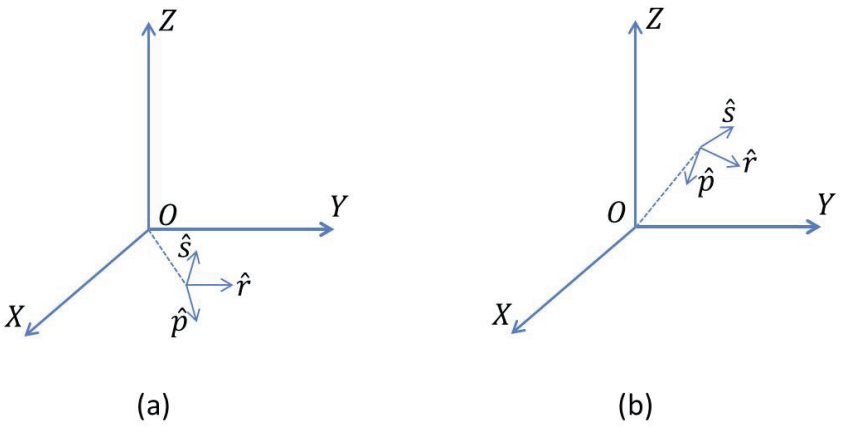

Figure 5.3: The global coordinate system, XYZ, where X is the ideal cross-track direction, Y is the ideal heading direction, Z is the ideal vertical direction and the origin, o is the ideal platform position at time, t; and the radar coordinate system, $\hat{r}\hat{s}\hat{p}$, where r is the radar azimuth direction, s is the radar elevation direction and p is the radar boresight pointing direction. (a) The radar coordinate system $\hat{r}\hat{s}\hat{p}$ before the 3D rotation. (b) The radar coordinate system $\hat{r}\hat{s}\hat{p}$ after three dimensional rotations.

$$\overline{\overline{R}}_Y(\theta) = \begin{pmatrix} \cos\theta & 0 & -\sin\theta \\ 0 & 1 & 0 \\ \sin\theta & 0 & \cos\theta \end{pmatrix} \tag{5.10}$$

$$\overline{\overline{R}}_Z(\theta) = \begin{pmatrix} \cos\theta & -\sin\theta & 0 \\ \sin\theta & \cos\theta & 0 \\ 0 & 0 & 1 \end{pmatrix} \quad . \tag{5.11}$$

The 3D rotation represented by the matrix $\overline{\overline{R}}$ in (5.1) is the rotation caused by attitude variation of the platform. However, there is an additional rotation of the radar coordinate system caused by the installation of the radar on the platform. For example, the plane of the antenna panel is not parallel to the Y-Z plane, but is tilted from the vertical direction. In the case of the Umass Ka-band radar, the antenna plane is titled by 5 degrees from the vertical direction. The additional installation rotation is given by,

$$\overline{\overline{R}}_i = \overline{\overline{R}}_Y(\theta_t)\overline{\overline{R}}_Z(\theta_{sq})\overline{\overline{R}}_X(\theta_d), \tag{5.12}$$

where θ_t is the tilting angle from the vertical direction, θ_{sq} is the squint angle and θ_d is the depression angle. These angles can be assumed to be known since they can be measured before the flight. Hence, the orientation of the radar coordinate system can be derived from the composition of $\overline{\overline{R}}$ and $\overline{\overline{R}}_i$.

Note that in practice the origin of the radar coordinate system and the rotation center of the platform are not at the same point, because the antenna is mounted outside of the platform. Hence there is an offset vector, $\bar{b}(t)$ between them, given as

$$\bar{b}(t) = \overline{\overline{R}}_2(t)\overline{\overline{R}}_1(t)\overline{b_0}, \tag{5.13}$$

where $\bar{b}_0$ is the initial offset vector from the origin of the global coordinate system, XYZ to the origin of the radar coordinate system, $\hat{r}\hat{s}\hat{p}$.

The basis vectors of the radar coordinate system, $\hat{r}\hat{s}\hat{p}$, can be obtained through

$$\begin{aligned}\hat{r}(t) &= \overline{\overline{R}}(t)\overline{\overline{R}}_i(t)\,[0\,0\,1]^T \\ \hat{s}(t) &= \overline{\overline{R}}(t)\overline{\overline{R}}_i(t)\,[1\,0\,0]^T \\ \hat{p}(t) &= \overline{\overline{R}}(t)\overline{\overline{R}}_i(t)\,[0\,1\,0]^T.\end{aligned} \tag{5.14}$$

With the knowledge of radar orientation, the elevation and azimuth angles, θ_{rs} and ϕ_{rs} of the scatterer relative to the radar coordinate system can be derived. Hence, for a given point scatterer A at location $\bar{p}$, the gain, $G_{los}(t)$, can be determined from the attitude and position parameters using (5.8), (5.9)-(5.12).

5.2 Motion Effects

5.2.1 Motion Effects on the SAR Magnitude Image

To fully understand the motion effect on the formation of SAR image, a simplified model of the radar and a point scatterer on the ground can be used to derive the point scatterer response of the radar, shown in Figure 5.4, from which the effects of radar motion can be determined. This work has been done in [25]. The derivation is included in this section for completeness. The nominal track of the platform is

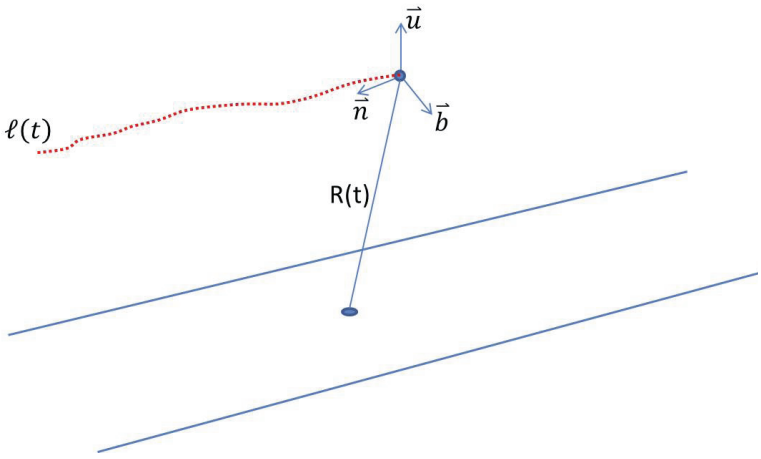

Figure 5.4: The setup of the radar and a point scatterer on the ground.

assumed to be a straight line and that the speed of the platform is a constant. Due to atmospheric turbulence, the actual position of the platform deviates from this nominal line. The deviation in the range direction is denoted by δR, which is a function of azimuth time, and the nominal range, as shown in Figure 5.5, in which the solid dot represents the nominal position and the hollow one represents the actual position. Here, the transmitted signal is given by

$$g_T(t) = A\,cos(2\pi f_0 t + \pi\beta t^2 + \phi_0), \quad t \in [0, T]. \tag{5.15}$$

The range-compressed signal, which is the result of Fourier transform from the raw

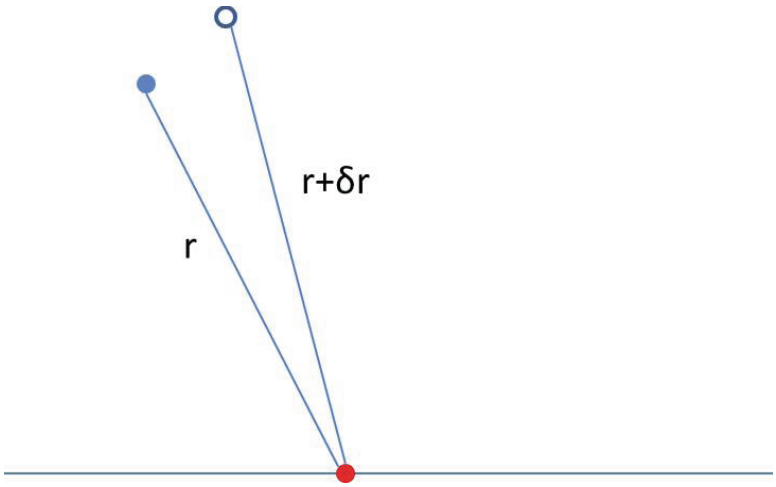

Figure 5.5: The setup of the radar and a point scatterer on the ground.

data, has the same form as (4.6) except that the instantaneous range $R(t; R_0)$ is replaced by $R_n(t) + \delta R(t)$. The term, $R_n(t)$, is the nominal range when the platform is flying in a straight line with a constant speed, and $\delta R(t)$ is the deviation of the range from the nominal one. The resulting expression of the range-compressed data then is given as

$$\begin{aligned} s(r, t; R_0) \approx & A_2\, a_a(t - t_c)\, \text{sinc}\left(\frac{(r - R(t; R_0))}{\Delta r}\right) \\ & \cdot \exp\left\{-j\frac{\pi r}{\Delta r}\right\} \cdot \exp\left\{j\phi_n(t)\right\} \cdot \exp\left\{j\phi_\delta(t)\right\}. \end{aligned} \tag{5.16}$$

In (5.16), $\phi_n(t)$ and $\phi_\delta(t)$ are the phases due to the nominal trajectory and the deviation from that trajectory, given as

$$\phi_n(t) = -\frac{4\pi R_n}{c}(f_{LO} - f_0) - \frac{4\pi\beta R_n^2(t)}{c^2}, \tag{5.17}$$

$$\phi_\delta(t) = -\frac{4\pi\delta R}{c} f_c - \frac{4\pi\beta}{c^2}(\delta R^2 + 2R_n\delta R). \tag{5.18}$$

In the above equations, Δr is the slant range resolution and δR is the amount of deviation from the nominal range, R_n, in the range dimension, f_c equals $f_{LO} - f_0 - \frac{B}{2}$. It can be seen that the effect of the non-ideal platform moving trajectory on the range-compressed data is that an additional phase term, $\phi_\delta(t)$, which is nearly proportional to the amount of deviation of δR, is added to the nominal phase, $\phi_n(t)$. Effectively, the motion error term is a phase "modulation" of the original signal in the azimuth dimension. Another effect is the peak location in the magnitude image is shifted by an amount equal to the deviation, δR.

As shown in Chapter 4, the next step of data processing is azimuth Fourier transform. From the property of Fourier transforms, the multiplication in time domain is equivalent to a convolution in the frequency domain, given by

$$S(r, f_t; R_0) \approx S_n(r, f_t; R_0) * MO_e(f_t), \tag{5.19}$$

in which $MO_e(f_t)$ represents the Fourier transform of the phase term, $\exp\{j\phi_\delta(t)\}$, as in

$$MO_e(f_t) = \int e^{j\phi_\delta(t)} e^{-j2\pi f_t t} dt, \tag{5.20}$$

and $S_n(r, f; R_0)$ is the nominal spectrum shown in Section 4.3, which is

$$\begin{aligned} S_n(r, f_t; R_0) =& A_2\, A_a(f_t - f_{tc})\, \mathrm{sinc}\left(\frac{1}{\Delta r}(r - R_0)\right) \\ & \cdot \exp\left\{-j\frac{\pi}{\Delta r} r\right\} \cdot \exp\left\{-j\frac{4\pi R(f_t; R_0) f_c}{c}\right\}. \end{aligned} \tag{5.21}$$

It can be seen that the spectrum in the azimuth dimension is modified by the spectrum of motion error. It should also be noted that the modification is ground-range dependent since $\delta R(t)$ is a function of the radar look angle.

After transforming the data along the azimuth dimension to the frequency domain, if the same matching filter as shown in (4.42) is applied, then the resulting output is

$$\begin{aligned} S(r, f_t; R_0) &= (S_n(r, f_t; R_0) * MO_e(f_t)) \cdot M_{az}(f_t; R_0) \\ &= M_{az}(f_t; R_0) \int_{\xi} S_n(r, \xi) MO_e(f_t - \xi) d\xi. \end{aligned} \tag{5.22}$$

Hence, the frequency domain matching filter will not correctly compensate the phase variation in the azimuth dimension, since the phase is corrupted from the convolution between the nominal signal and the motion error term. The output of the matching filter will have a residual phase due to the motion. The effect of the motion error depends on the spectrum of the motion error term $MO_e(f_t)$, and needs to be compensated. Taking a simple form of the motion error as an example, if the motion is in a single frequency sinusoidal form, then $e^{j\phi_\delta(t)} = e^{jdr\sin(\omega_m(t))}$, which can be expanded into a series of cosine functions that are multiples of the fundamental frequencies,

$$e^{j\phi_\delta(t)} = \sum_{k=0}^{+\infty} j^k J_k(dr) \cos(k\omega_m f_t + k\pi/2). \tag{5.23}$$

The effect on the convolution in (5.22) is a summation of the shifted version of the nominal signal spectrum $S_n(r, f_t)$,

$$S(r, f_t; R_0) = M_{az}(f_t; R_0) \sum_{k=-\infty}^{+\infty} C_k j^{|k|} J_{|k|} S_n(r, f_t - k\omega_m), \tag{5.24}$$

in which, $C_k = 1/2$ for $k \neq 0$, and $C_0 = 1$. From this simple example, it shows that the azimuth spectrum is smeared, causing a resolution degradation. The effect of (5.22) is that the final phase is that of the integration result of the original spectrum $S_n(r, f_t)$, but weighted by the motion error spectrum, $MO_e(f_t)$.

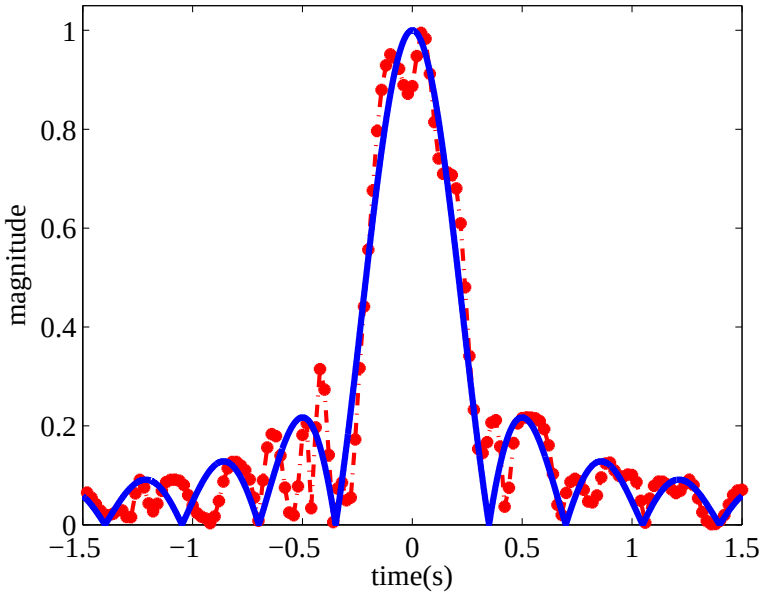

Figure 5.6: A simulated case with magnitude variation during a synthetic aperture. The blue line is the nominal magnitude response and the red dashed line is the magnitude with a random variation of yaw angle, which has a standard deviation of 0.2 degree and a bandwidth of 5Hz.

5.2.2 Effects of Magnitude Variation

As shown previously, the platform attitude variation can cause a variation in the signal magnitude along the azimuth direction for a point scatterer. An example is shown in Figure 5.6 and 5.7. The effects of the magnitude variation can be complex. For example, if the variation is slow such that during the synthetic aperture time, the platform has a constant deviation angle from its nominal heading, then the response signal will be time-shifted, as shown in Figure 5.8, and in the frequency domain, it will be a Doppler shift. This has been discussed in the previous chapter under Section 4.3.

Another extreme case is that the platform encounters a "fast" attitude vibration during the synthetic aperture time. In this context, fast is relative to the correlation time of the random process which would be much less than the synthetic aperture time, as in

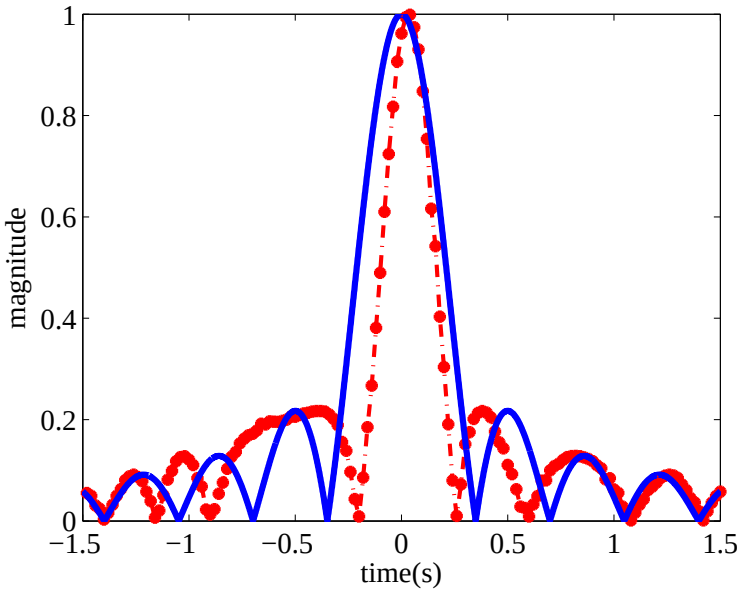

Figure 5.7: A simulated case: the platform deviates from its nominal heading with a time-dependent random angle, which has a narrow bandwidth of 1 Hz and a standard deviation of 0.2 degree.

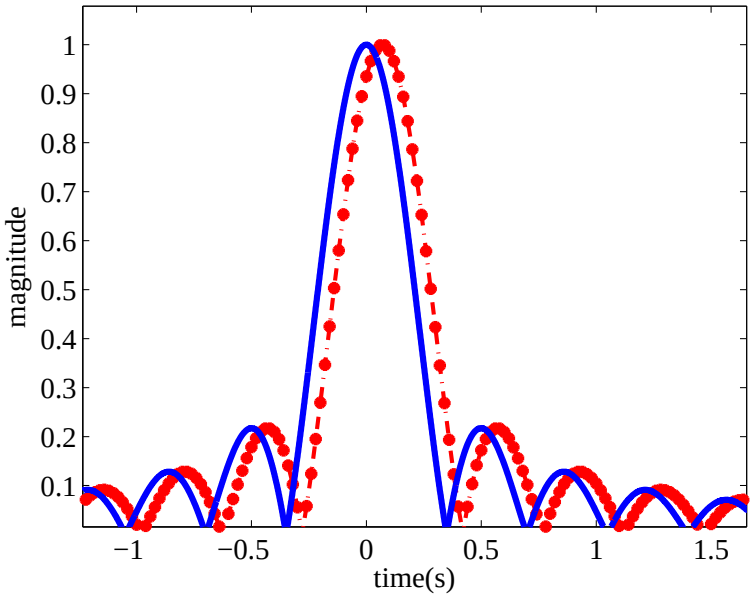

Figure 5.8: A simulated case: the platform deviates from its nominal heading with a angle of 0.2 degree.

L	0.5m
v	50m/s
λ	8.6mm
R	1000m

Table 5.1: System parameters and values used for (5.25).

$$\begin{aligned} & \tau_v \ll T \\ \text{or} \quad & \frac{1}{BW_v} \ll \frac{\lambda R}{Lv} \\ \text{then} \quad & BW_v \gg \frac{Lv}{\lambda R}. \end{aligned} \tag{5.25}$$

In such a case, due to the longer integration time, which is the synthetic aperture time, T shown in (5.25), the effects caused by the random magnitude variation can be largely reduced.

As an example, with the system parameters of the platform being used in this dissertation, shown in Table 5.1, the criterion for a *fast* magnitude variation becomes, $BW_v \gg 2.9$Hz.

In practice, the attitude variation caused by wind is a narrow-band process. In Figure 5.9, it shows the measured yaw angle variation and its spectrum for part of the flight. The spectrum contains almost only low-frequency components, less than 0.05 Hz. In the case of slow magnitude variation during the synthetic aperture time, the effects will not cancel out during azimuth compression. Instead, the slow magnitude variation during the synthetic aperture time will have non-negligible effects on the azimuth pulse compression. For an extreme example, the antenna could be steered toward the scatterer while the platform is moving along the track, in a process known as spotlight SAR. This observing strategy has the effect of increasing the Doppler bandwidth hence improving the azimuth resolution.

In a detailed example, we can assume the case that the antenna phase center follows the ideal straight line track, but there are attitude variations during the flight.

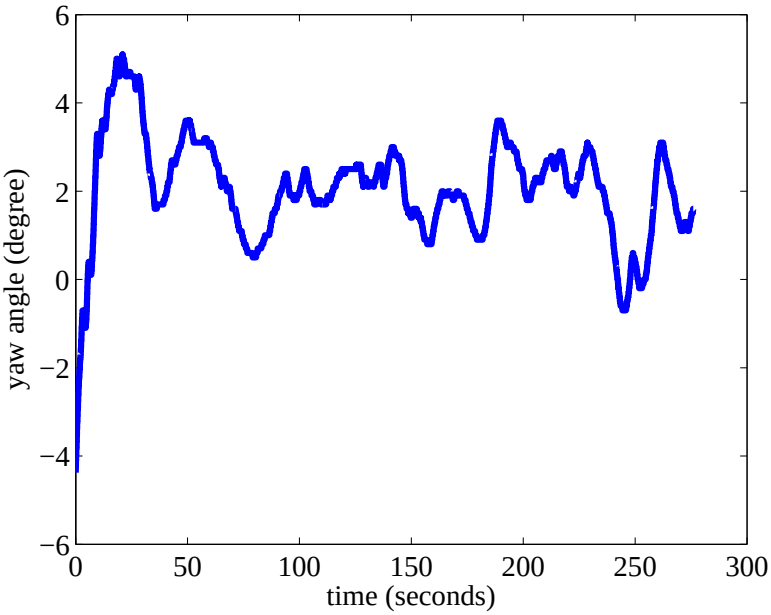

(a)

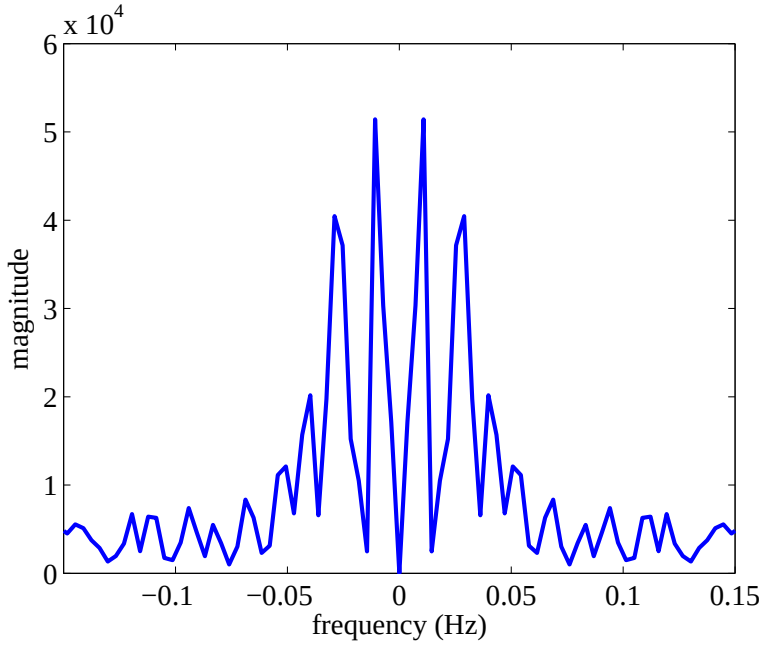

(b)

Figure 5.9: (a)Measured yaw angle versus time. (b) The spectrum of the yaw angle variation with DC offset removed.

In general, the received radar echo from a point scatterer can be written as a function of azimuth time, t, as

$$s(t) = a(t)e^{j\phi(t)} \tag{5.26}$$

where $a(t)$ is the magnitude, determined by the antenna pattern and the relative position of the point scatterer in the antenna pattern, and $\phi(t)$ is the phase due to the time delay between the antenna and the scatterer.

The azimuth compression using the matched filter in the time domain is expressed by the correlation

$$R(t) = \int a(\tau)e^{j\phi(\tau)}e^{-j\phi(\tau-t)}d\tau, \tag{5.27}$$

where the phase $\phi(t)$ is given by

$$\begin{aligned}\phi(t) &= \frac{2R(t)}{c} = \frac{2\sqrt{R_0^2 + v^2t^2}}{c} \\ &\approx \frac{2}{c}(R_0 + \frac{v^2t^2}{2R_0}).\end{aligned} \tag{5.28}$$

Here, the phase of the matched filter $\phi(t-\tau)$ is given by

$$\phi(\tau - t) \approx \frac{2}{c}(R_0 + \frac{v^2(\tau - t)^2}{2R_0}) \tag{5.29}$$

and thus the phase progression in the azimuth direction is

$$\begin{aligned}\phi(\tau) - \phi(\tau - t) &= \frac{v^2}{cR_0}(2\tau t - t^2) \\ &= \frac{2v^2}{cR_0}\tau t - \frac{v^2t^2}{cR_0},\end{aligned} \tag{5.30}$$

and (5.27) becomes

$$\begin{aligned}R(t) &= e^{-j\frac{v^2t^2}{cR_0}} \int a(\tau)e^{j\frac{2v^2}{cR_0}\tau t}d\tau \\ &= e^{-j\frac{v^2t^2}{cR_0}}\ A(f)|_{f=-\frac{v^2}{cR_0\pi}t}\,.\end{aligned} \tag{5.31}$$

It can be seen that the azimuth compression output, $R(t)$ equals the Fourier transform of the amplitude function, $a(t)$, with a linear translation between the frequency, f, and the azimuth time, t.

The amplitude function, $a(t)$, can be decomposed into two parts, one part,$a_0(t)$, corresponds to the nominal antenna pattern while the platform moves in an ideal straight-line trajectory, and the other part, $\Delta a(t)$, corresponds to the amplitude variation due to the platform attitude variation, $\Delta a(t)$, which gives

$$a(t) = a_0(t) + \Delta a(t). \tag{5.32}$$

Accordingly, the resulting correlation, $R(t)$, becomes

$$R(t) = e^{-j\frac{v^2t^2}{cR_0}} \left(A_0(f) + \Delta A(f)\right)\Big|_{f=-\frac{v^2t}{cR_0\pi}}, \tag{5.33}$$

where $\Delta A(f)$ is the Fourier transform of $\Delta a(t)$.

It can be seen that attitude variation has an effect of an offset to the desired azimuthal response. The precise form of the variation depends on the amplitude of the variation $\Delta a(t)$ and its frequency spectrum. Further, the amplitude of the variation, $\Delta a(t)$, has a nonlinear relation with the attitude parameters, such as yaw, pitch and roll angles, and the specific antenna pattern. For example, the amplitude variation of a narrow-beamwidth antenna pattern will be larger than that of a wide-beamwidth antenna pattern for a given attitude variation. This is illustrated in Figure 5.10.

5.2.3 Angular Motion Effect

The magnitude of the echoes from a scatterer is proportional to the antenna gain in the direction of the scatterer. Hence the signal envelope along the azimuth dimension follows the azimuth antenna beam pattern. In other words, the envelope is a transformation of the azimuth antenna beam pattern from a function of the azimuth angle to a function of time, as given in

$$f : g(\theta) \mapsto g(t), \tag{5.34}$$

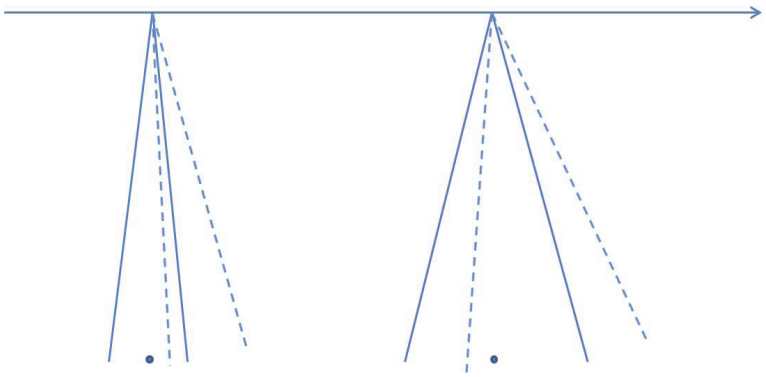

Figure 5.10: An illustration of the effects of attitude variation on the narrow and wide antenna beamwidth. The solid lines represent the original antenna beam, and the dashed lines represent the rotated antenna beam.

where f is the mapping from the antenna beam pattern, $g(\theta)$ to the signal envelope, $g(t)$. The mapping f is fulfilled through the mapping from the instantaneous time, t to the azimuth angle, θ, as in

$$\theta = \theta_0 + \omega t, \quad t \in [-\frac{T}{2}, \frac{T}{2}] \tag{5.35}$$

where θ_0 is the offset azimuth angle and ω is the angular velocity of the antenna beam relative to the scatterer in the azimuth dimension. An illustration diagram is shown in Figure 5.11, where the plot is simplified without loss of generality that the angular velocity is assumed to be constant. As a result, the mapping of the antenna beam pattern to the signal envelope is shown in Figure 5.12.

If there are additional angular motions of the platform, the mapped function, $g(t)$ in (5.34) will be in a different form which depends on the characteristics of the angular motion. An example of an additional yaw angle variation is shown in Figure 5.13. In this example the antenna is continuously squinted towards the scatterer, causing an additional angular motion. Effectively, this extra angular motion causes an increase to the angular velocity, ω, hence a decrease to the illumination time, T of

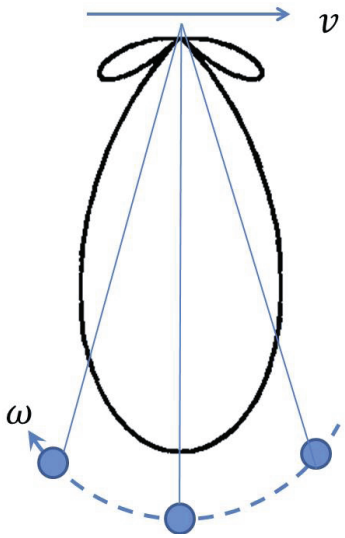

Figure 5.11: An illustration of the relative angular motion between the radar antenna and the scatterer with an angular velocity of ω. The range variation is ignored, it focuses on the angular variation. The radar antenna is moving right with a velocity of v.

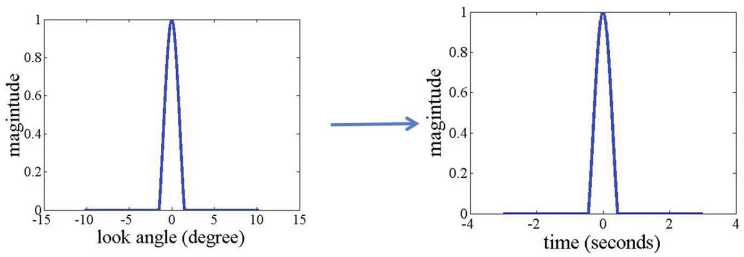

Figure 5.12: The antenna beam pattern (upper left) and the envelope of the radar echoes (bottom right). They share the same shape but with look angle mapping to time with a straight-line moving velocity of 60 m/s.

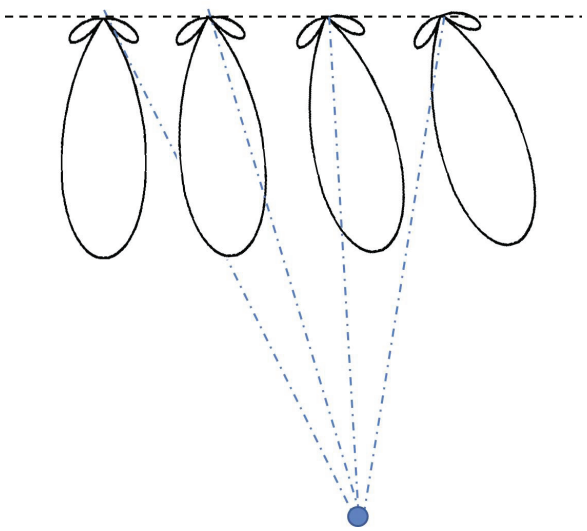

Figure 5.13: An illustration of the attitude variation of the antenna relative to a point scatterer. The antenna is continuously squinting forward, hence it causes an additional variation to the look angle of the scatterer.

the scatterer. Its effect on the point scatterer response will be analyzed in the next section.

In this section, we will discuss the effect of angular motion on the point scatterer response starting with the mathematical expression of the mapping function from the antenna pattern, $g(\theta)$ to the time-domain signal envelope, $g(t)$ through the angular motion.

A diagram of the radar look geometry is shown in Figure 5.14. The position of the antenna is a function of time, $x(t)$. Here only the one-dimensional case is considered for simplicity, but it can be extended to the 3-dimensional case without difficulty.

The look angle, θ_i, which is relative to the zero-Doppler direction, can be derived in terms of the instantaneous position of the antenna, $x(t)$, as in

$$\theta_i(t) = \text{atan}\left(\frac{x_0 - x(t)}{R_0}\right). \tag{5.36}$$

Further, the look angle relative to the main beam axis of the antenna is given by

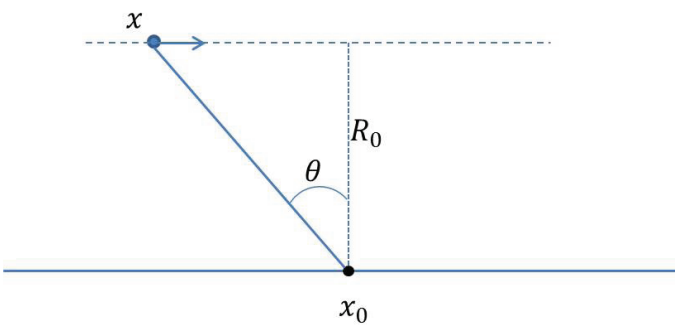

Figure 5.14: A diagram of the radar look geometry. A point scatterer is located at x_0, the radar antenna is located at x with a look angle of θ. The zero-Doppler range is denoted by R_0.

$$\theta_r(t) = \text{atan}\left(\frac{x_0 - x(t)}{R_0}\right) - \theta_0(t), \tag{5.37}$$

where θ_0 is the angle between the antenna main beam direction and the zero-Doppler direction. If θ_0 is a function of time, i.e., there is an additional motion due to the platform attitudes variation, the period during which the antenna beam illuminates the scatterer is either increased or decreased depending on the direction of the angular motion. The angular velocity is then given as

$$\omega = \frac{\partial \theta_r(t)}{\partial t} = -\frac{\cos^2\theta_i(t)}{R_0}\frac{\partial x(t)}{\partial t} - \frac{\partial \theta_0(t)}{\partial t}, \tag{5.38}$$

The additional angular motion, $\frac{\partial \theta_0}{\partial t}$, has two effects on the signal envelope. The first is the start and stop time of the signal envelope is changed because the time the antenna starts and stops illuminating the scatterer is changed. Therefore the signal envelope is time-shifted. The second effect is the duration or the width in time of the signal envelope is changed because the antenna beam is sweeping either faster or slower when it is illuminating the scatterer.

On the other hand, the phase history is not affected by the angular motion since it is determined by the distance between the radar phase center and the point scatterer. Then instantaneous Doppler frequency, which is the derivative of the phase history,

remains the same. However, since the signal envelope changes its position and width in time due to the above two effects of the angular motion, the Doppler bandwidth is different now. An illustration of the bandwidth decreasing is shown in Figure 5.15. It can be seen that the waveform in the bottom plot is narrower than that of the top plot, suggesting a decrease to Doppler bandwidth.

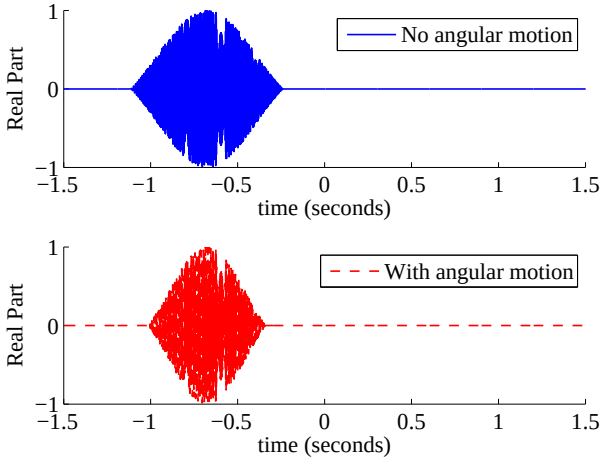

Figure 5.15: An illustration of Doppler bandwidth variation due to angular motion. The simulation is taken in the scene of Figure 5.13, the antenna beam is angularly moving towards a point scatterer with the rate of 1 degree/second. The 3 dB Doppler bandwidth is decreased from 441.84 Hz to 342.92 Hz, a 22.4% change in bandwidth, hence the along-track resolution of the point scatterer response also degrades by 22.4%.

The Doppler bandwidth is given by

$$B_D = \frac{2v}{\lambda}\left(\sin\theta_i(t_1) - \sin\theta_i(t_2)\right), \tag{5.39}$$

where t_1 and t_2 are the instantaneous time when the scatterer is illuminated by the antenna through its 3-dB beam directions and they are given by

$$\begin{aligned} \theta_i(t_1) &= \theta_0(t_1) + \frac{\theta_{3\text{dB}}}{2} \\ \theta_i(t_2) &= \theta_0(t_2) - \frac{\theta_{3\text{dB}}}{2}, \end{aligned} \tag{5.40}$$

where $\theta_{3\text{dB}}$ is the 3-dB beamwidth of the antenna. As in the case of the simulation result in Figure 5.15, the antenna is rotating towards the scatterer, then $\theta_0(t_1) < \theta_0(t_2)$, hence according to (5.39), by using some trigonometric identity, the expression of the Doppler bandwidth can be converted to

$$\begin{aligned} B_D &= \frac{4v}{\lambda}\cos\frac{\theta_0(t_1)+\theta_0(t_2)}{2}\sin\left(\frac{\theta_{3\text{dB}}}{2}-\frac{\theta_0(t_2)-\theta_0(t_1)}{2}\right) \\ &\approx \frac{4v}{\lambda}\cos\theta_0\sin\left(\frac{\theta_{3\text{dB}}+\theta_0(t_1)-\theta_0(t_2)}{2}\right). \end{aligned} \tag{5.41}$$

It can be seen from (5.41) that the Doppler bandwidth decreases when the antenna is squinting towards the scatterer, i.e., $\theta_0(t_1) < \theta_0(t_2)$, and it increases if the antenna is squinting away from the sacatterer, i.e., $\theta_0(t_1) > \theta_0(t_2)$. Hence the angular motion will cause non-uniform along-track resolutions across the image, because the antenna is squinting towards some scatterers but meanwhile squinting away from other scatterers.

5.2.4 Motion Effects for FMCW Radar

The major difference between pulsed radar and FMCW radar is in the duration of the transmitted pulses. In pulsed radar, the pulses are usually short, typically in microseconds. For example, the SAR in ERS-1/2 satellite has a pulse duration of $37.12\,\mu s$ while the PRF is $1640 - 1720\,\text{Hz}$. In FMCW radar, however, the pulses are transmitted and received continuously, and the duration of each pulse is in milliseconds.

This characteristic of FMCW radar has two main effects, the first is that the stop-and-go approximation is not valid anymore, the second is that the effect of the platform motion during one FMCW pulse cannot be neglected. Both of these effects have been studied before [18][30].

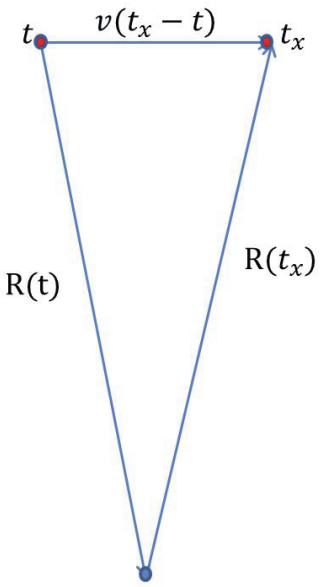

Figure 5.16: The diagram shows the time delay varies with time. t is the time the signal starts to transmit, and t_x is the time the echo gets back to the receiver.

One period of the signal is given by

$$s(t) = e^{j(\omega_0(t-t_m)+\frac{1}{2}\beta(t-t_m)^2+\phi_0)}, \quad t_m - \frac{T}{2} \leq t \leq t_m + \frac{T}{2}, \tag{5.42}$$

in which T is the period of the signal which is $\frac{1}{PRF}$, and t_m is the center time of the period. Suppose there is only one point scatterer at a zero Doppler range of R_0 at the time t_0. The instantaneous range from the radar to the scatterer is then given by

$$R(t) = \sqrt{R_0^2 + v^2(t-t_0)^2}, \tag{5.43}$$

where v is the speed of the platform, and T is the duration time of the pulse.

Since the radar phase center is moving while the radar is transmitting the signal and receiving the back-scattered echoes, the time delay of the between transmitting and receiving is varying with time, shown in Figure 5.16. The time and range in

Figure 5.16 satisfy the equation in

$$t_x - t = \frac{R(t) + R(t_x)}{c}, \tag{5.44}$$

where t is the time the signal starts to transmit, t_x is the time the echo gets back to the receiver, and c is the speed of light. The variable t_x can then be solved using (5.44) and (5.43), the result is shown in

$$t_x = \frac{c^2 t_R - v^2 t_0 \pm \sqrt{c^2 v^2 (t_0 - t_R)^2 + (c^2 - v^2) R_0^2}}{c^2 - v^2}, \tag{5.45}$$

where t_R is the time the transmitted signal reaching the scatterer, and is given by

$$t_R = t + \frac{R(t)}{c}. \tag{5.46}$$

Hence, when $c \gg v$, we will have

$$\begin{aligned} t_x &= \frac{t_R - (\frac{v}{c})^2 t_0 \pm \sqrt{(\frac{v}{c})^2 (t_0 - t_R)^2 + \frac{c^2 - v^2}{c^4} R_0^2}}{1 - (\frac{v}{c})^2} \\ &\approx t_R \pm \frac{1}{c} \sqrt{v^2 (t_0 - t_R)^2 + R_0^2} \\ &= t_R + \frac{R(t_R)}{c} \\ &\approx t + \frac{2R(t)}{c}. \end{aligned} \tag{5.47}$$

Hence the delay $\tau(t)$ which is $t_x - t$, can be approximated by

$$\tau(t) \approx \frac{2R(t)}{c}. \tag{5.48}$$

Therefore the received signal can be expressed as

$$\begin{aligned} g(t) &= s\big(t - \tau(t)\big) \\ &= e^{j(\omega_0 (t - t_m - \tau(t)) + \frac{1}{2}\beta (t - t_m - \tau(t))^2 + \phi_0)}. \end{aligned} \tag{5.49}$$

After the on-board de-chirping, the output signal is

$$\begin{aligned} f(t,t_m) &= s(t) \times g^*(t) \\ &= e^{j\left(\omega_0\tau(t)+\beta(t-t_m)\tau(t)-\frac{1}{2}\beta\tau^2(t)\right)}. \end{aligned} \tag{5.50}$$

In FMCW radar, the range compression is fulfilled by doing Fourier transform, and then the linear mapping from frequency to the slant range:

$$\begin{aligned} F(f,t_m) &= \int_{t_1}^{t_2} e^{j\left(\omega_0\tau(t)+\beta(t-t_m)\tau(t)-\frac{1}{2}\beta\tau^2(t)\right)} dt \\ &= \int_{t_1}^{t_2} e^{j2\frac{R(t)}{c}\left(\omega_0+\beta(t-t_m)-\beta\frac{R(t)}{c}\right)} dt \end{aligned} \tag{5.51}$$

However, there is no analytical expression for this Fourier transform, and the stationary phase method cannot be used here since the time-bandwidth product of the signal is small (< 10). Therefore, to analyze the integration, we need some degree of approximation for the phase of the integrand. If we take the Taylor expansion of $R(t)$ to the first order about $t = t_m$, the center of the signal, as shown in

$$\begin{aligned} R(t) &\approx R(t_m) + \left.\frac{dR}{dt}\right|_{t=t_m} (t-t_m) \\ &= r_m + v_{rm}(t-t_m), \end{aligned} \tag{5.52}$$

in which $r_m = R(t_m)$, and $v_{rm} = \left.\frac{dR}{dt}\right|_{t=t_m} = \frac{v^2(t_m-t_0)}{r_m}$ is the radial velocity at time t_m. Then the phase of the integrand in (5.51) can be approximated as

$$\begin{aligned} \phi_{int}(t) \approx{}& \frac{2\omega_0}{c}\left(r_m + v_{rm}(t-t_m)\right) + \frac{2\beta}{c}(t-t_m)\left(r_m + v_{rm}(t-t_m)\right) \\ &- \frac{2\beta}{c^2}\left(r_m + v_{rm}(t-t_m)\right)^2. \end{aligned} \tag{5.53}$$

Further simplification can be made to $\phi_{int}(t)$ in the limit of $t - t_m \to 0$, then

$$\phi_{int}(t) \approx \left(\frac{2\omega_0 r_m}{c} - \frac{2\beta r_m^2}{c^2}\right) + \left(\frac{2\beta r_m}{c} + \frac{2\omega_0 v_{rm}}{c} - \frac{4\beta r_m v_{rm}}{c^2}\right)(t-t_m). \tag{5.54}$$

From (5.54), it can be seen that when $v_{rm} = 0$, it reduces to the form corresponding to the stop-and-go approximation. The term $\frac{2\beta r_m}{c}$ is the beat frequency corresponding to the range of r_m, the term $\frac{2\omega_0 v_{rm}}{c}$ is the Doppler frequency corresponding to the magnitude of the radial velocity, v_{rm}, and the carrier frequency, ω_0. The third term, $\frac{4\beta r_m v_{rm}}{c^2}$, represents an extra Doppler shift corresponding to the beat signal, which is much smaller comparing to the Doppler shift due to RF carrier. If we let

$$\omega_{bm} = \frac{2\beta r_m}{c} \tag{5.55}$$

$$\omega_{dop}(v_{rm}) = \frac{2\omega_0 v_{rm}}{c} \tag{5.56}$$

$$\omega_{dop1}(v_{rm}) = \frac{4\beta r_m v_{rm}}{c^2} = \frac{2\omega_{bm} v_{rm}}{c}, \tag{5.57}$$

then $\phi_{int}(t)$ can be rewritten in the following form

$$\begin{aligned} \phi_{int}(t) &\approx \left(\frac{2\omega_0 r_m}{c} - \frac{2\beta r_m^2}{c^2}\right) + \Big(\omega_{bm} + \omega_{dop}(v_{rm}) - \omega_{dop1}(v_{rm})\Big)(t - t_m) \\ &\approx \left(\frac{2\omega_0 r_m}{c} - \frac{2\beta r_m^2}{c^2}\right) + \Big(\omega_{bm} + \omega_{dop}(v_{rm})\Big)(t - t_m). \end{aligned} \tag{5.58}$$

The phase given in (5.54) represents a single frequency signal. The phase at the peak of the spectrum in the frequency domain in (5.51) equals $\phi_{int}(t = 0)$. However, when we do the Discrete Fourier transform (DFT), the start time of the sequence is shifted from t_1 to $t = 0$, thus there will be a phase shift at the peak. In essence, the phase of the DFT is $\phi_{int}(t = t_1)$, using (5.52), we have

$$\begin{aligned} t_1 &= t_m - \frac{T}{2} + \tau(t_m - \frac{T}{2}) \\ &\approx t_m - \frac{T}{2} + \frac{2R(t_m - \frac{T}{2})}{c} \\ &\approx t_m - \frac{T}{2} + \frac{2}{c}\left(r_m - \frac{v_{rm}T}{2}\right). \end{aligned} \tag{5.59}$$

By substituting (5.59) into (5.58), we can get the phase at the peak after the DFT

$$\begin{aligned}\phi_{int}(t_1) &\approx \left(\frac{2\omega_0 r_m}{c} - \frac{\omega_{bm} r_m}{c}\right) + \left(\omega_{bm} + \omega_{dop}(v_{rm})\right)\left(-\frac{T}{2} + \frac{2r_m}{c} - \frac{v_{rm}}{c}T\right) \\ &= \left(\frac{2\omega_0 r_m}{c} - \frac{\omega_{bm} r_m}{c}\right) + \omega_{bm}\left(-\frac{T}{2} + \frac{2r_m}{c}\right) + \omega_{dop}\left(-\frac{T}{2} + \frac{2r_m}{c}\right) \\ &\quad - \frac{v_{rm}T}{c}\left(\omega_{bm} + \omega_{dop}\right) \\ &\approx \phi_0 + \omega_{dop}\left(-\frac{T}{2} + \frac{2r_m}{c}\right) \quad ,\end{aligned} \tag{5.60}$$

where

$$\phi_0 = \left(\frac{2\omega_0 r_m}{c} - \frac{\omega_{bm} r_m}{c}\right) + \omega_{bm}\left(-\frac{T}{2} + \frac{2r_m}{c}\right). \tag{5.61}$$

In (5.60), the term with $\frac{v_{rm}}{c}T$ is neglected since for typical system parameters, $\frac{v_{rm}}{c}T$, is much smaller than a cycle of the beat signal, ω_{bm}, and the Doppler frequency, ω_{dop}.

It can be seen from (5.60) that there is an additional phase added to the stop-and-go phase, ϕ_0. That phase is caused by the Doppler effect within the signal transmission and reception period. The added phase is proportional to the Doppler frequency which is a function of the radial velocity, v_{rm}. Therefore it is also a function of t_m, as in

$$\begin{aligned}\phi_{added}(t_m) \approx -\frac{\omega_{dop}T}{2} &= -\frac{\omega_0 T v_m}{c} \\ &= -\frac{\omega_0 T v^2}{c}\frac{t_m - t_0}{\sqrt{R_0^2 + v^2(t_m - t_0)^2}} \quad .\end{aligned} \tag{5.62}$$

Here the added phase, ϕ_{added}, is a nonlinear function of t_m, which can be simplified if $t_m - t_0$ is small, which means the aperture time is small, as

$$\begin{aligned}\phi_{added} &\approx -\frac{\omega_0 T v^2}{c}\frac{t_m - t_0}{R_0}\left(1 - \frac{v^2(t_m - t_0)^2}{2R_0^2}\right) \\ &= -\frac{\omega_0 T v^2}{c}\frac{t_m - t_0}{R_0} + \frac{\omega_0 T v^4}{c}\frac{(t_m - t_0)^3}{2R_0^3} \quad .\end{aligned} \tag{5.63}$$

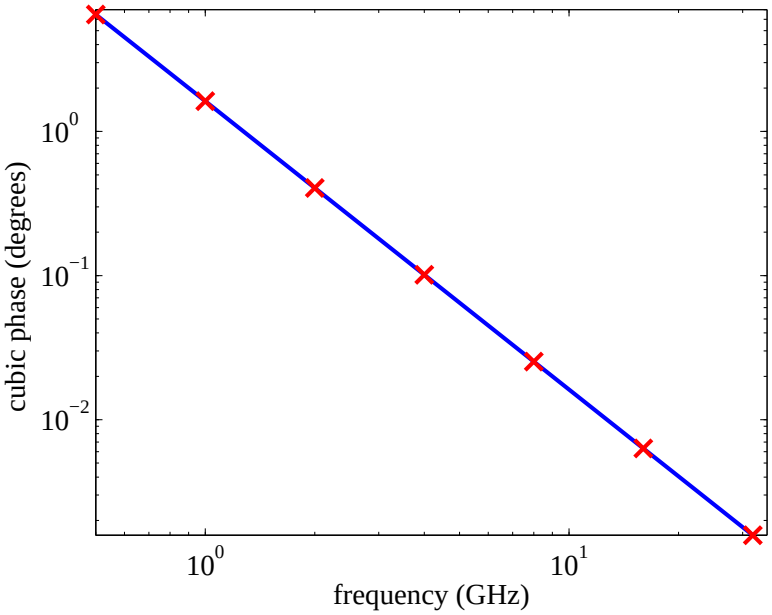

Figure 5.17: Calculated upper bound of the cubic phase term, with $T = 1$ms, $v = 100$m/s, $L_a = 0.5$m.

In (5.63), the first term on the right side is a linear phase with respect to t_m, the second term is a cubic function with respect to t_m, but can be bounded as

$$\begin{aligned} \left| \frac{\omega_0 T v^4}{c} \frac{(t_m - t_0)^3}{2R_0^3} \right| &\leq \frac{\omega_0 T v^4 T_a^3}{16 c R_0^3} \\ &\approx \frac{\pi T v \lambda^2}{8 c L_a^3} \quad , \end{aligned} \tag{5.64}$$

where T_a is the synthetic aperture length, and L_a is the along-track length of the antenna. Therefore, for a given antenna size, L_a and chirp length, and the period T, the upper bound of the cubic phase term is related to the carrier wavelength. It is plotted with some practical parameter values in Figure 5.17.

In this figure, it can be seen that the cubic phase term is small for most practical wavelengths, and thus its effect can be ignored. Hence, the added phase is given by the linear term

$$\phi_{added} \approx -\frac{\omega_0 T v^2}{c} \frac{t_m - t_0}{R_0} \quad . \tag{5.65}$$

The effect of the added linear phase, ϕ_{added}, on the azimuth compression can be interpreted then as a time shift of $\frac{T}{2}$, which corresponds to an along-track distance of $\frac{vT}{2}$. This phase will also introduce an additional phase after the compression, which is $\frac{\pi T^2 v^2}{2\lambda R_0}$, however, this is very small and can be neglected. For example, for a Ka-band airborne SAR working at 35 GHz, this term is less than 0.1 degree.

5.3 Motion Compensation

The effects of unwanted motion of radar platform on both the SAR magnitude and InSAR phase have been shown in the previous section. It is clear that these effects will induce errors in the topographic measurements, such as loss of image resolution and interferometric phase distortion. In order to improve the accuracy of the topographic measurements, these errors have to be mitigated with or without external motion data. This motion compensation procedure has been studied as early as 1960's [31, 32], not long after the invention of SAR. In this section, the compensation methods corresponding to three different scenarios will be discussed: i.)no motion data, ii.) perfect motion data, and iii.) noisy motion data. Usually, motion data is measured with an inertial measurement unit (IMU) carried by the platform. The IMU records the platform positions and attitude as time series, at a certain sampling rate, with the intention that the platform motion can be reconstructed from the samples.

5.3.1 Motion Compensation Methods

There are various SAR processing algorithms suitable for different SAR systems, similarly, there are different types of motion compensation methods designed for different SAR systems. For example, a time-domain two-step motion compensation algorithm was introduced in [33]. In this algorithm, the motion compensation is integrated with the chirp scailing SAR processing algorithm. The raw data goes through a first order motion compensation procedure by the multiplication of a phase

correction function, which is based on a reference range. The second order motion error correction is undertaken after the range compression, which corrects the range-dependent motion errors.

Motion compensation algorithms implementing in the frequency domain have been developed as well. In [34], a spectral domain multi-look technique was presented, which can be utilized to perform look-wise motion compensation. A similar frequency division method was proposed in [35] for wide beam SAR motion compensation. Topography-dependent motion compensation algorithms have been introduced in [36, 37]. In [36], a sub-aperture algorithm, which was first presented in [38], combined with a topography-dependent phase correction based on an external DEM, was demonstrated. In [37], a topography and aperture dependent algorithm was introduced, which incorporates the phase correction for each pixel of the SAR image efficiently by using the time-frequency correspondence between time-domain and frequency-domain SAR data. In this dissertation, the precise topography- and aperture-dependent motion compensation algorithm introduced in [37] will be utilized for its accuracy and efficiency. The algorithm will be described briefly in the next subsection for the completeness of this dissertation.

5.3.2 Precise Topography- and Aperture-Dependent Motion Compensation

As its name suggests, this algorithm has three characteristics: i.) it compensates the motion error for each pixel of the SAR image; ii.) it compensates the topography-dependent motion error. iii.) it takes into account the aspect angle dependency of the motion error.

The topography dependency of the motion error is caused by the change of look angle, as illustrated in Figure 5.18, where two point scatterers at the same range and different heights have different displacements in range dimension. The displacement

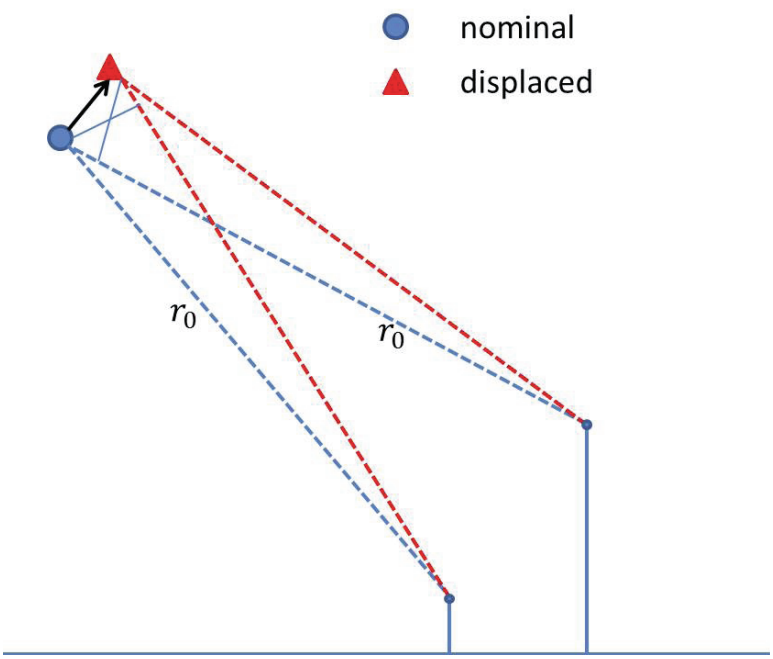

Figure 5.18: A diagram shows the topography dependency of the motion error.

in range induced by the topography can be calculated as

$$\begin{aligned}\delta\Delta r_0 = \sqrt{(H+\Delta z)^2 + (\sqrt{r_0^2 - H^2} + \Delta y)^2} \\ -\sqrt{(H-\Delta h+\Delta z)^2 + (\sqrt{r_0^2 - (H-\Delta h)^2} + \Delta y)^2},\end{aligned} \tag{5.66}$$

where H is the platform nominal height above the reference level, Δz is the vertical displacement from the nominal track, Δy is the horizontal displacement, and Δh is the scatterer height (topography) above the reference level.

The aperture dependency of the motion error can be easily understood from Figure 5.19, in which it shows that the displacement in range dimension depends on the particular position of the platform in the aperture. The aperture-dependent displacement is given as

$$\Delta r(r,x) = r_0\sqrt{(1+\frac{\Delta r_0}{r_0})^2 + tan^2\theta_{sq}(x)} - r_0\sqrt{1+tan^2\theta_{sq}} \approx \Delta r_0 cos\theta_{sq}(x), \tag{5.67}$$

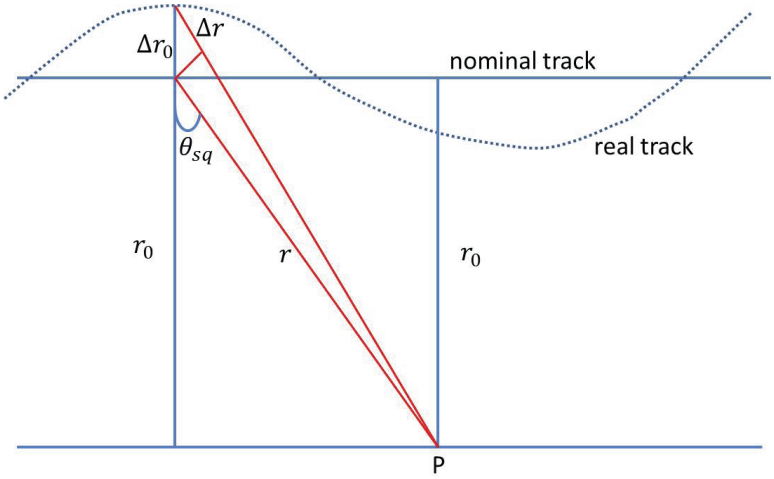

Figure 5.19: A diagram shows the aperture dependency of the motion error.

where $\Delta r(r, x)$ is the aperture dependent displacement in range, r_0 is the closest range for a given scatterer, and θ_{sq} is the squint angle from the antenna to the scatterer. A flow diagram of the algorithm is shown in Figure 5.20. The SAR data is processed with a certain block size, which is the number of range line, typically 16 or 32. The calculated phase error φ_{topo} is proportional to the displacement in (5.66) with a coefficient of $\frac{4\pi}{\lambda}$. The transform of the time-domain phase error $\varphi_{topo}(t_i)$ into the frequency-domain phase error $\varphi_{topo}(f)$ is accomplished through the relation

$$f = -\frac{2v^2}{\lambda} \cdot \frac{t_i}{\sqrt{r_0^2 + v^2 t_i^2}}, \tag{5.68}$$

where v is the forward velocity of the platform, and λ is the carrier wavelength.

5.3.3 Results

In this section the simulation result of the topography- and aperture-dependent motion compensation for a point scatterer is shown to illustrate the algorithm. The system parameters of the simulated radar systems is given in Table 5.2. The point scatterer is located at a ground range of 696 meters, with a height of 100 meters. The motion error is a sinusoidal function of time with a amplitude of 0.1 meter, as shown

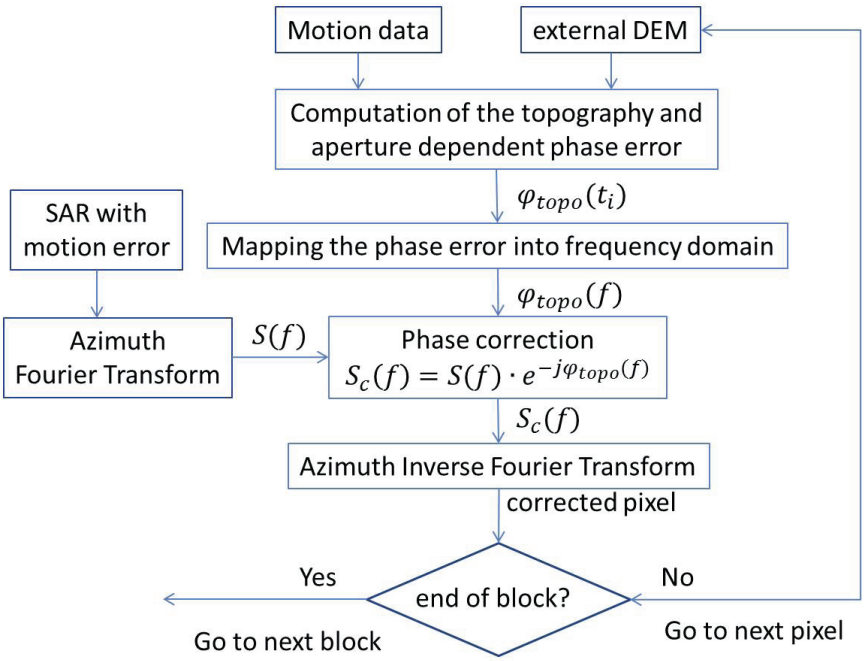

Figure 5.20: A flow diagram of the topography- and aperture-dependent motion compensation algorithm.

in Figure 5.21. The frequency of the motion error is 3 Hz, and the region in which the point scatterer is illuminated is marked by the two lines, which is determined by the beamwidth. It can be seen the displacement in the marked region is approximately linear because of its short duration comparing to the sinusoidal cycle. The simulation result of point spreading function without motion error is shown in Figure 5.22. After adding the motion error, the spreading function is shifted to the right by 2.0 meters, as shown as the dashed curve in Figure 5.23. This shift is due to the linear variation of displacement, which causes a linear phase shift in the frequency domain.

5.3.4 Error Analysis

In practice, the platform position is measured by a GPS receiver, which can provide a certain level of accuracy depending on the specific technology being used. A typical GPS system can achieve an accuracy of 15 meters, a typical differential GPS (DGPS) can achieve an accuracy of 3-5 meters, and a typical WAAS (Wide Area

parameter	value
Center Frequency	35.0 GHz
Bandwidth	100 MHz
Height	696 m
Beamwidth	1 degree
Look Angle	45 degree
Squint Angle	0 degree
PRF	1 KHz

Table 5.2: System parameters of the simulated radar system.

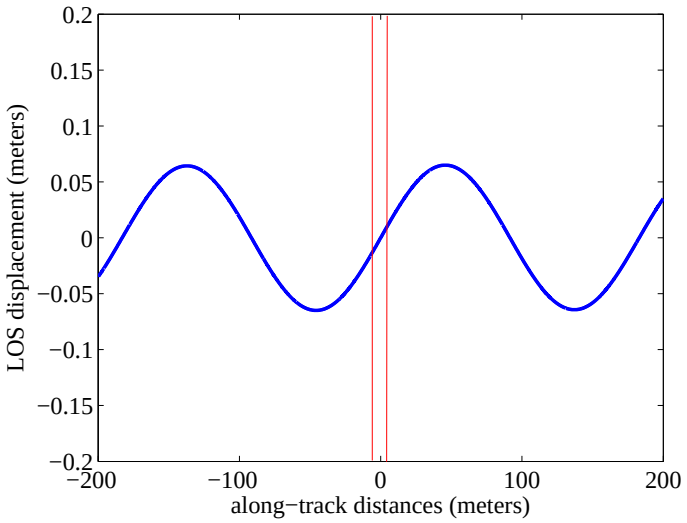

Figure 5.21: The line of sight displacements for the point scatterer when there is a motion variation of 1.0 meter in amplitude in the vertical dimension.

Augmentation System)-enabled GPS can achieve an accuracy of less than 3 meters. In this section, the effect of the measurement error on the motion compensation result is analyzed. It will serve as a guideline in the airborne synthetic aperture radar system design.

The range displacements, calculated from the measured platform positions (5.67), can be expressed as

$$\Delta r = \Delta r_0 + \Delta r_n, \tag{5.69}$$

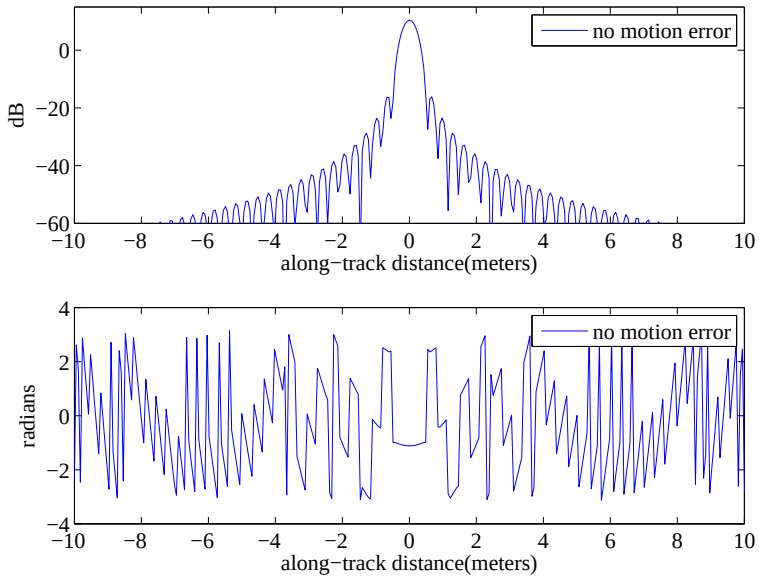

Figure 5.22: The simulation result of the point spreading function of a point scatterer in the case of no motion error in the platform trajectory.

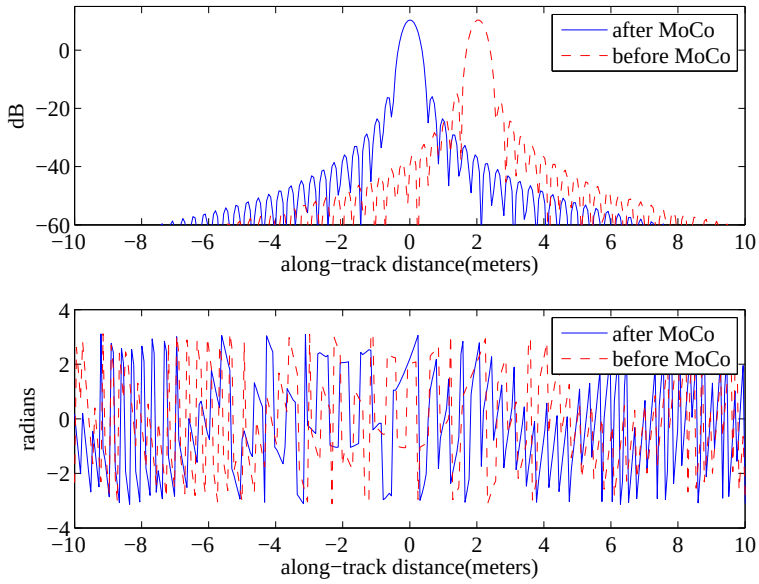

Figure 5.23: The simulation result of the point spreading function of a point scatterer when the platform trajectory is displaced from the ideal straight line.

where Δr_0 is the error free displacement, and Δr_n is the error term, which can be modeled as a stochastic process, and its characteristic depends on the specific GPS receiver being used. As a consequence, the calculated phase error can be decomposed into two parts as well, and then the phase correction term in Figure 5.20 can be rewritten as

$$\begin{aligned} & e^{-j\varphi_{topo}(f)} \\ =& e^{-j\frac{4\pi}{\lambda}(\Delta r_0+\Delta r_n)} \\ =& e^{-j\frac{4\pi}{\lambda}\Delta r_0} \cdot e^{-j\frac{4\pi}{\lambda}\Delta r_n}, \end{aligned} \tag{5.70}$$

in which the first term is the error free phase correction term, which will compensate the phase error correctly. The second term, however, corresponding to the measurement error in positions, will cause a degradation to the compensation result in time-domain, where the inverse Fourier transform of the error term convolves with the ideal compensation result. Since the impact of the error term on the image quality depends on the specific form of the error, and the error is stochastic in nature, it will be analyzed in three different categories.

5.3.4.1 Linear error

If the error of displacement Δr_n is linear, such as

$$\Delta r_n = K \cdot f, \tag{5.71}$$

where the coefficient K is a random number. The inverse Fourier transform of the error term then is given by

$$\begin{aligned} & \int e^{-j\frac{4\pi}{\lambda}Kf} \cdot e^{j2\pi ft}\, df \\ =& \int e^{j(-\frac{2K}{\lambda}+t)2\pi f}\, df \\ =& \delta(t-\frac{2K}{\lambda}). \end{aligned} \tag{5.72}$$

It shows the effect of the linear measurement error will be a shift in the along-track direction by an amount of $\frac{2K}{\lambda}$. The random number, K, can be determined following the procedure in [39]. Consider a deterministic sinusoidal displacement with a constant frequency, γ_0, and a constant phase, ξ_0,

$$\Delta r_n(f) = a_0 cos(2\pi\gamma_0 f - \xi_0), \tag{5.73}$$

If we take the Taylor expansion around $f = 0$, the linear term is given by

$$\Delta r_{nl}(f) = a_0 f \cdot 2\pi\gamma_0, \text{ for } \xi_0 = \pi/2. \tag{5.74}$$

Hence the point scatterer response is shift by the distance, l_s, where

$$l_s = \frac{2K}{\lambda} = \frac{4\pi}{\lambda} a_0\gamma_0. \tag{5.75}$$

It can be seen that the shift is proportional to the amplitude and frequency of the sinusoid and inversely proportional to the carrier wavelength. This is the shift due to the linear term of a constant frequency sinusoidal signal. In order to take all of the frequency components within the spectrum into account, the variance of the shift across the scene can be obtained by

$$\sigma_{ls}^2 = (\frac{4\pi}{\lambda})^2 \int_0^{1/f_D} G_d(\gamma)\gamma^2 \, d\gamma, \tag{5.76}$$

where $G_d(\gamma)$ is the power spectral density(PSD) of the displacement measurement error, and the upper limit of the integration is $1/f_D$, where f_D is the Doppler bandwidth since it is being processed in frequency domain.

5.3.4.2 High Frequency Error

Displacement errors with frequencies higher than $1/f_D$, as shown in [25, 39], may cause "paired echoes" and increase of the sidelobe level. One metric for the quality

of this motion compensation is the Integrated Sidelobe Ratio, or the ISLR, which is a measure of the system response outside of the main focus area of interest. The integrated sidelobe ratio can be express as

$$\text{ISLR} = \int_{1/f_D}^{\infty} G_d(\gamma)\,\gamma. \tag{5.77}$$

5.4 Angular Motion Compensation

5.4.1 Theory

The angular motion effects can be compensated if the look angle of the scatterer, $\theta_r(t)$ in (5.37) is known. In the case of an airborne radar, the typical angular motion is a slow dynamic process which has a correlation time much larger than the synthetic aperture time. Therefore the variation of the angular parameters during the synthetic aperture time can be approximated with a linear function, i.e., the angular velocity in (5.38) is a constant. In this case, the signal envelope, $g(t)$ is a stretched or a squeezed version of the nominal signal envelope, which is mapped from the antenna pattern without the additional angular motion, as shown in Figure 5.15.

The compensation of the angular motion is to convert the measured signal envelope, $a_m(t)$ to the desired signal envelope, $a_0(t)$, which is not affected by the additional angular motion, as illustrated in Figure 5.24. Similar to the compensation of the phase center motion, the compensation of the angular motion can be implemented pixel by pixel in the focused SAR image as well. For each pixel in the SAR image, the look angle of the scatterers in that pixel relative to the antenna main beam can be calculated for each pulse time according to (5.37). The flow chart of the angular motion compensation is shown in Figure 5.25. First in the SAR image a number of k adjacent pixels are chosen for the compensation. There are two reasons to use k pixels instead of one, one is that the response of a point scatterer in the SAR image has a finite number of pixels; the other is that the angular motions for the adjacent scatterers are the same under the condition that the angular motion is a slow dynamic process.

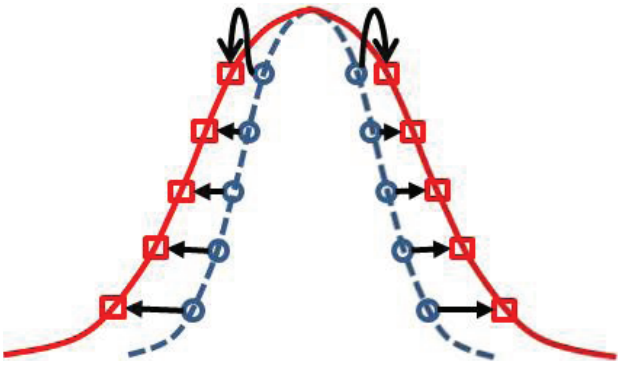

Figure 5.24: An illustration of angular motion compensation. Each sample (circle) of the measured signal envelope (dashed line) is replaced to to the desired time (square), hence the signal envelope is converted to the desired one (solid line).

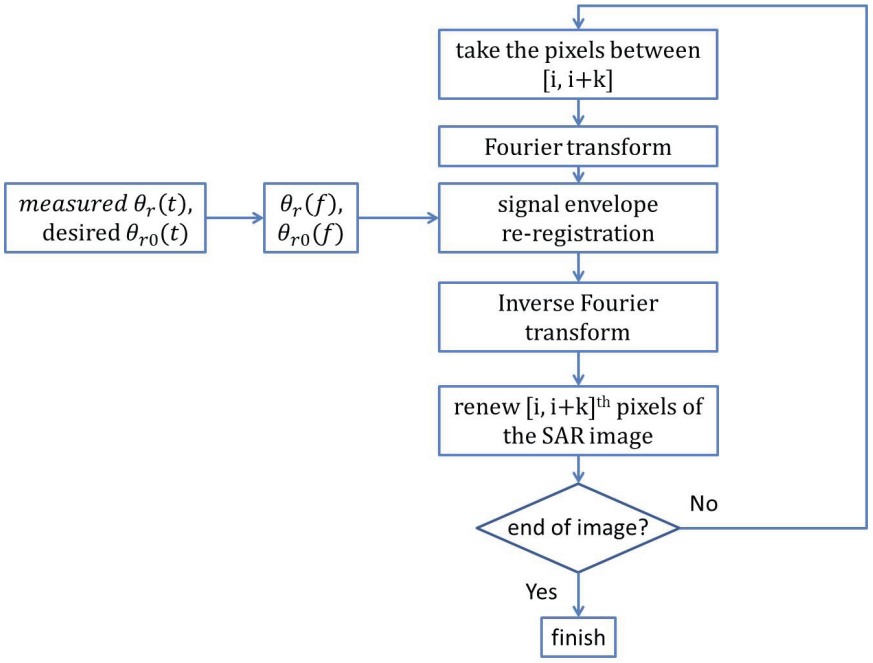

Figure 5.25: The flow chart of the angular motion compensation.

Next the time domain pixels are converted to the frequency domain through Fourier transform. The angular motion compensation is implemented in the frequency domain as the phase center motion compensation. In the frequency domain, the measured signal envelope, $A_m(f)$, needs to be converted to the desired signal envelope, $A_o(f)$. For a given frequency, f_1 the value of $A_o(f_1)$ has to be found from

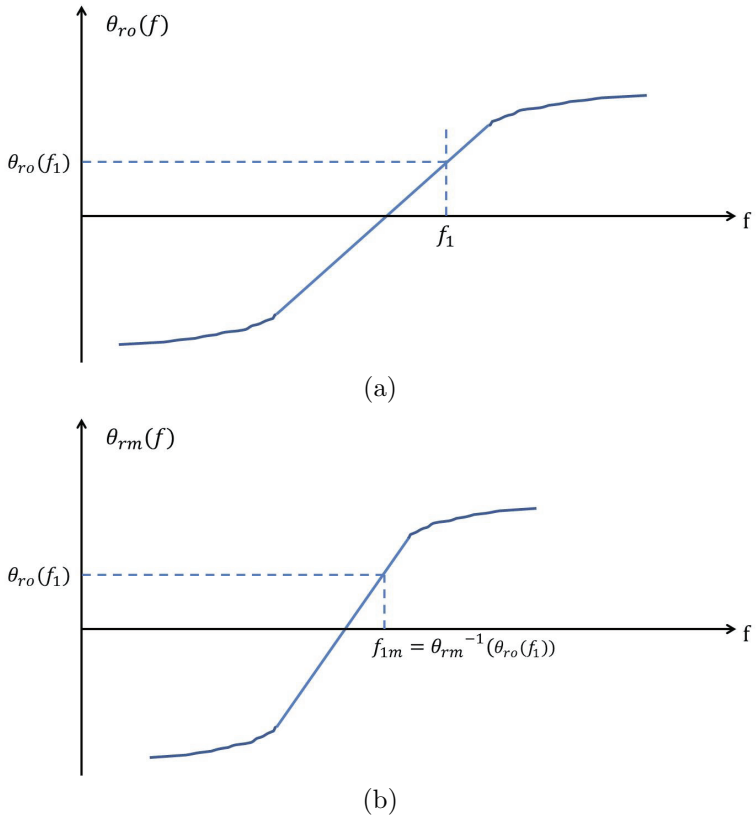

Figure 5.26: (a) The desired look angle $\theta_{ro}(f)$ in the frequency domain. The value of a look angle can be found for a given frequency, f_1. (b) The measured look angle $\theta_{rm}(f)$. The value of the frequency, f_{1m} can be derived for the desired look angle, $\theta_{ro}(f_1)$.

$A_m(f_{1m})$. If the desired look angle is $\theta_{ro}(f)$, which is the Fourier transform of the desired look angle, $\theta_{ro}(t)$, then the desired look angle at the frequency, f_1, is

$$\theta_1 = \theta_{ro}(f_1)\,, \tag{5.78}$$

as shown in Figure 5.26(a).

Since the measured look angle as a function of time as shown in (5.37) is known from the attitude measurements, its frequency domain translation, $\theta_{rm}(f)$ is known as well. Then the frequency at which the measured look angle equals to the desired look angle at frequency, f_1, can be derived as

$$f_{1m} = \theta_{rm}^{-1}(\theta_1)\,, \tag{5.79}$$

where $f = \theta_{rm}^{-1}(\theta)$ is the inverse function of $\theta = \theta_{rm}(f)$, as shown in Figure 5.26(b).

Then the value of desired signal envelope at frequency, f_1, is derived from

$$\begin{aligned} A_o(f_1) &= A_m(f_{1m}) \\ &= A_m(\theta_{rm}^{-1}(\theta_{ro}(f_1)))\,, \end{aligned} \tag{5.80}$$

where f_1 can be any frequency in the Doppler bandwidth as shown in Figure 5.27, then (5.80) can be written as

$$A_o(f) = A_m(\theta_{rm}^{-1}(\theta_{ro}(f)))\,. \tag{5.81}$$

5.4.2 Simulation

In this section a simulation is made for a two-dimensional case to verify the angular motion compensation algorithm proposed in the previous section. The algorithm has not been applied to measured Ka-band SAR data due to error of the IMU data. The radar and target geometry are shown in Figure 5.14. The radar platform and target parameters are summarized in Table 5.3. The antenna beam is squinting towards the positive x-axis direction. The simulated time-domain signal before doing the synthetic aperture processing is shown in Figure 5.28.

Then the time domain signal is focused with the matched filter in the frequency domain, and it is transformed back to the time domain as a synthetic aperture radar signal. Since the signal is focused, a narrow time window can be used to select the target within a certain period of time. Next the selected target signal is transformed to the frequency domain. For each frequency, f, the corresponding frequency, f_m

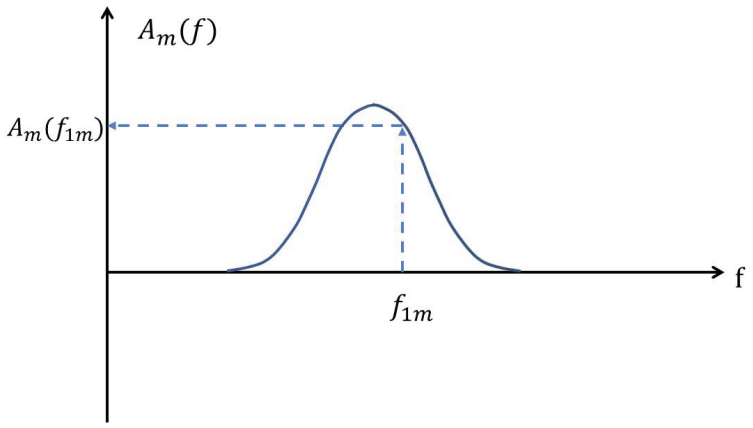

(a)

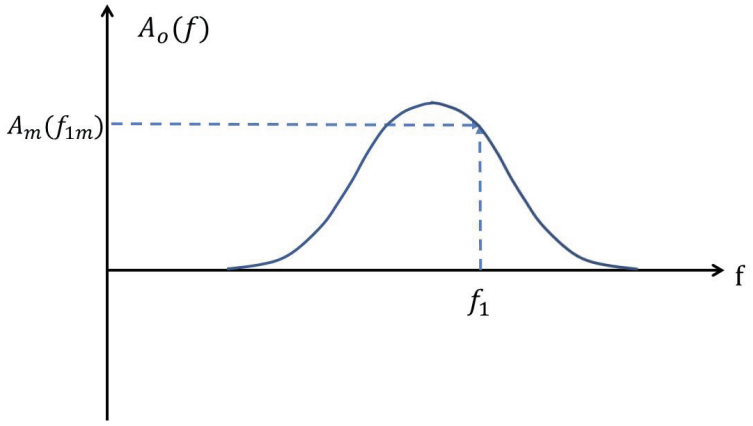

(b)

Figure 5.27: (a) The measured signal envelope, $A_m(f)$. The value of the signal envelope can be found for a given frequency, f_{1m}. (b) The desired signal envelope, $A_o(f)$, which is the result of the angular motion compensation.

is found such that the measured look angle, θ at the frequency, f_m is the desired look angle at the frequency, f. Then the magnitude of the target spectrum at the frequency, f_m is mapped to the frequency, f. Hence the desired magnitude, which is the magnitude without the angular motion, can be reconstructed. The signal phase can be extrapolated from the measured phase. After the frequency domain signal is compensated, it is converted to the time domain. The results are shown in Figure 5.29.

It can be seen from Figure 5.29(a) that the magnitude of the compensated signal matches the ideal signal without angular motion very well within the 3 dB Doppler

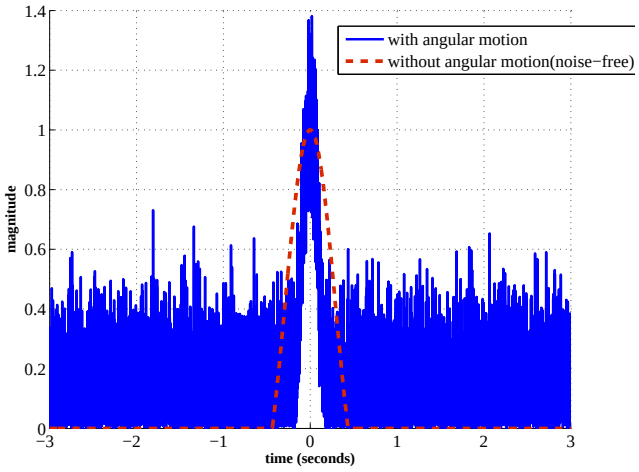

(a)

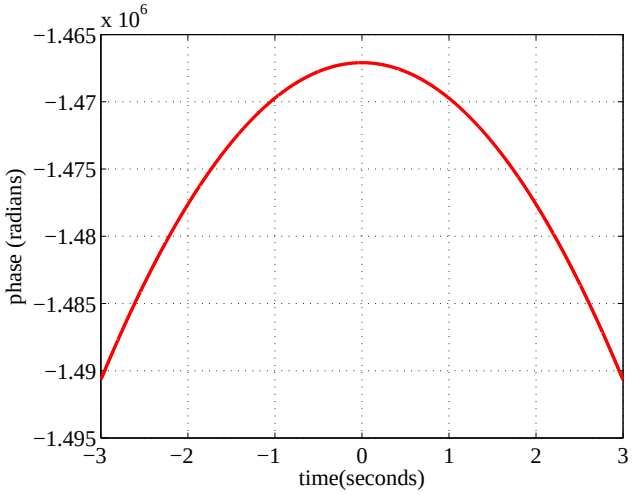

(b)

Figure 5.28: (a)The signal magnitude in the time domain. (b)The signal phase in the time domain. (c) The look angle of the target relative to the antenna main beam.

Parameter	Transmitter
platform height	1000 m
target location	(0,0)
beamwidth	1.5 deg
carrier frequency	35.0 GHz
platform velocity	60 m/s
yaw rate	5 deg/s
SNR	15 dB

Table 5.3: The radar platform and target parameters in the angular motion compensation simulation.

bandwidth. It has larger sidelobes beyond the 3 dB Doppler bandwidth since it is mapped from the measured target signal, which has a larger sidelobes due to the noise. From Figure 5.29(b), it can be seen that the compensated signal is focused to a narrower region since the signal Doppler bandwidth has been expanded.

The results shown in Figure 5.29 is for only one target. If there are more than one target within the time window and they have comparable radar cross section (RCS), then the performance of the angular compensation algorithm will be degraded. An example of two target with the same RCS is shown in Figure 5.30. The two targets are separated by 0.3 meter. It can be seen that the ideal signal spectrum has three lobes due to the interfering between the two targets. However, the measured signal spectrum has only one narrow lobe, hence the compensated signal spectrum can only have one lobe. As a consequence, the compensated signal in the time domain only has one target, but with better resolution and SNR than the uncompensated one.

If there is a dominant target, i.e., its RCS is much greater than the other targets, the angular compensation algorithm will focus the received signal to the dominant target, as shown in Figure 5.31, where the two targets are separated by 0.3 meter and has a RCS ratio of 20 dB.

As a summary, the angular motion compensation algorithm proposed in this section can perfectly compensate for the angular motion effect in the single target

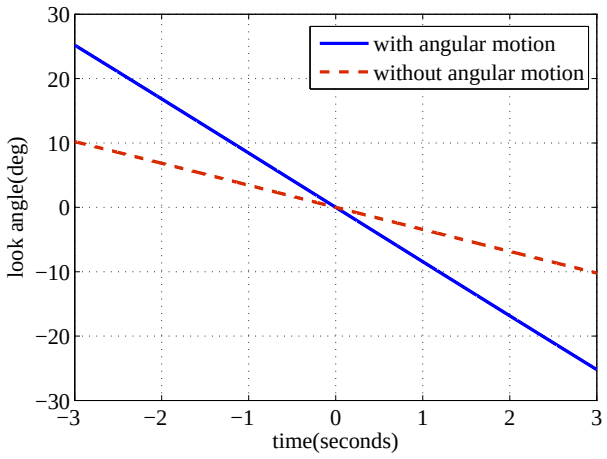

(c)

Figure 5.28: Continued. a)The signal magnitude in time-domain. (b)The signal phase in time-domain. (c) The look angle of the target relative to the antenna main beam.

.

case. In the case of multiple targets in one time window, the algorithm can not recover all the targets, it can instead reconstruct one of the targets but with increased signal to noise ratio. The dominant target can be reconstructed successfully. Since this algorithm iterates for every Doppler frequency bin, its efficiency depends on the number of samples in the Doppler frequency domain. One strategy to boost the efficiency is to only implement the angular motion compensation algorithm over the targets whose Doppler bandwidth has been decreased due to the angular motion.

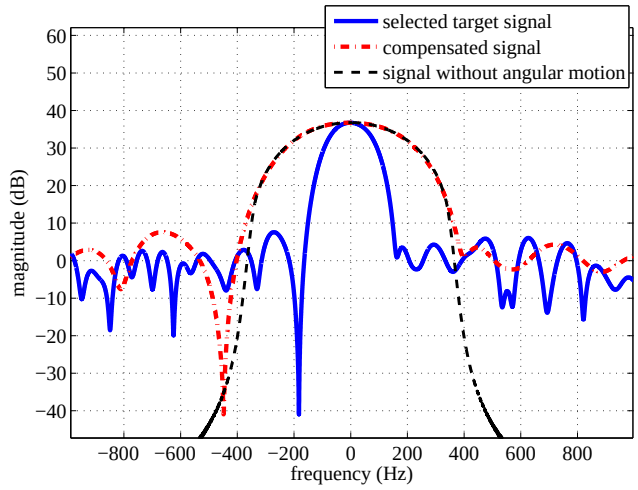

(a)

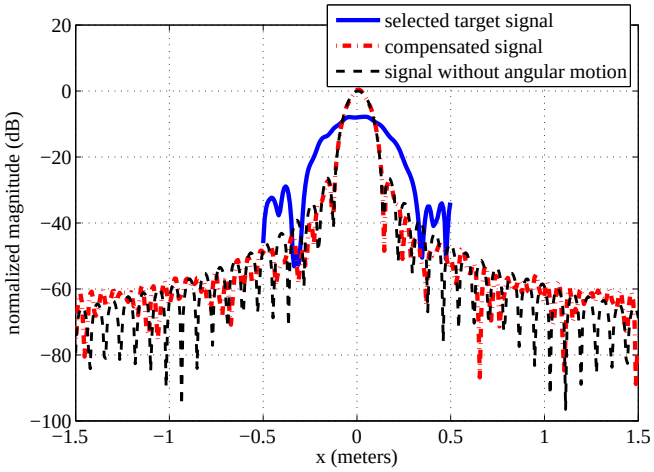

(b)

Figure 5.29: (a)The signal magnitude in the frequency domain. (b)The compensated signal in the time domain.

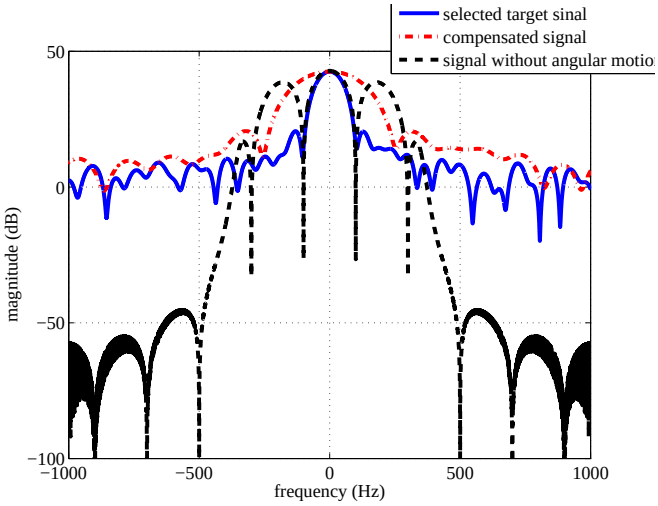

(a)

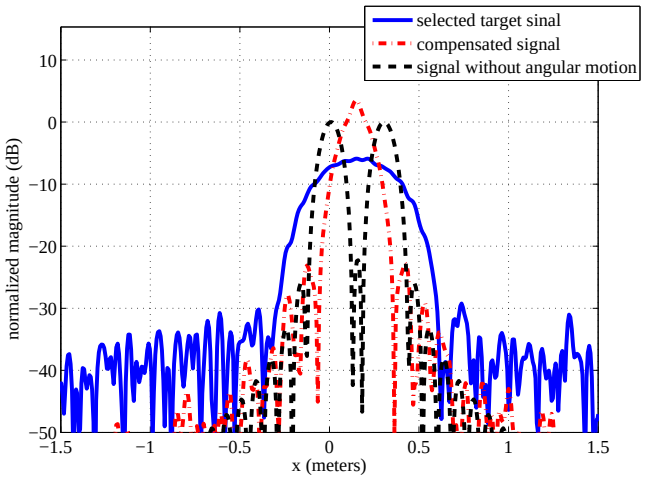

(b)

Figure 5.30: (a)The signal magnitude in the frequency domain. (b)The compensated signal in the time domain.

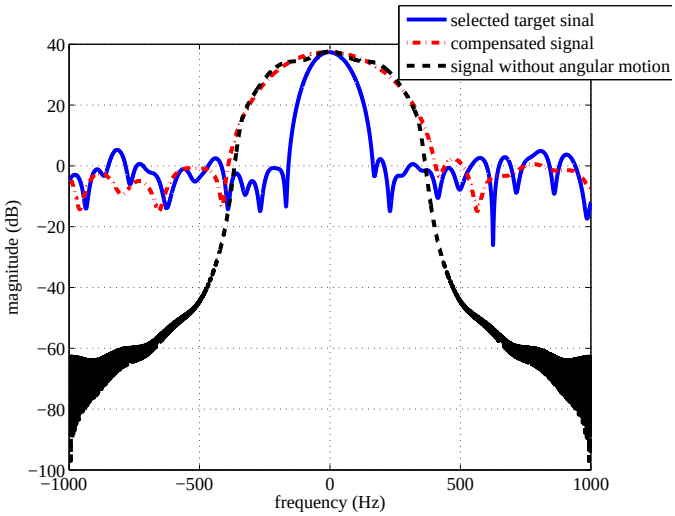

(a)

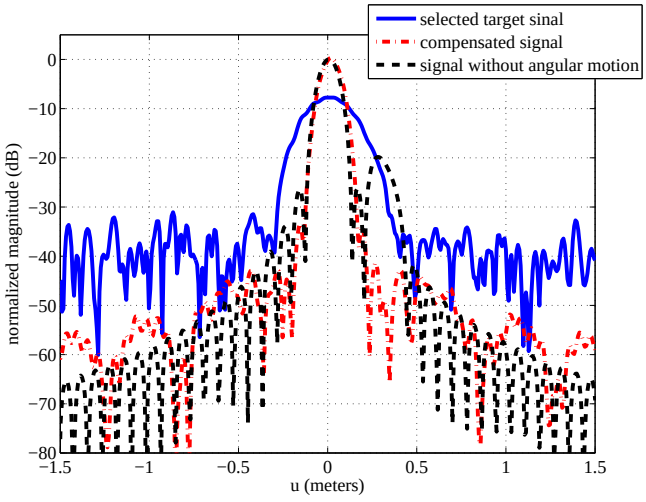

(b)

Figure 5.31: (a)The signal magnitude in the frequency domain. (b)The compensated signal in the time domain.

CHAPTER 6

INTERFEROMETRIC PROCESSING

6.1 Introduction

Interferometric SAR (InSAR) utilizes two or more receiving channels to sample the backscattering field at different spatial locations. Hence at least two complex SAR images are generated for each of the channels. A correlation map between these channels is produced and used to infer the topographic information. Depending on the direction in which the antennas are separated, the interferometry can be either along-track or cross-track. The interferometric SAR can also be divided into two types based on the number of flights of data collection over the same area. One is the single-pass InSAR, which has more than one antenna receiving at the same time on the platform. The other is the repeat-pass InSAR, which has only one receiving antenna but flies over the same area and transmits and collects radar echoes multiple times.

In this dissertation, the case of a single-pass InSAR is considered. A single-pass interferometer is not affected by temporal decorrelation and does not need multiple flights to form an interferometric mapping of the ground targets. A diagram of interferometric SAR is shown in Figure 6.1. Put simply, interferometric SAR estimates the arrival direction of the scattering waves or the look angle θ, by means using the additional path length of a signal arriving at one antenna with respect to another,

$$\theta \approx \alpha + \sin^{-1}\Big(\frac{\Delta R}{B}\Big). \tag{6.1}$$

Once known, the topography can be determined from θ, with other parameters known about the observing system, as in

$$h = H - R_1 \cos\theta. \tag{6.2}$$

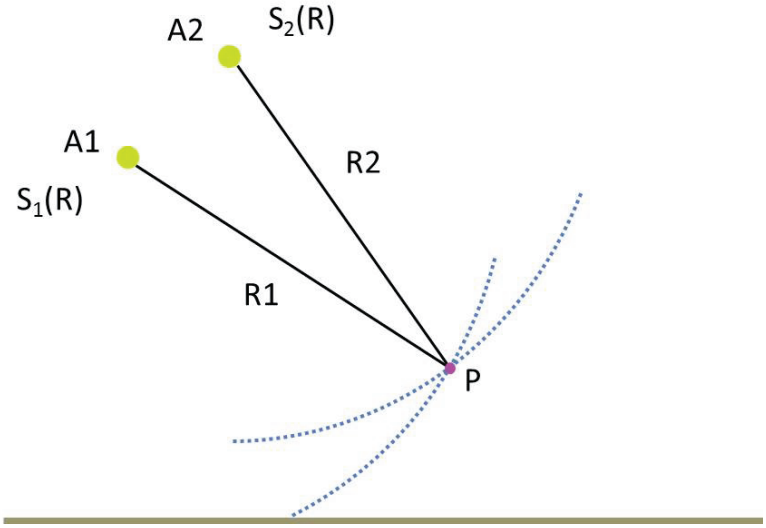

(a)

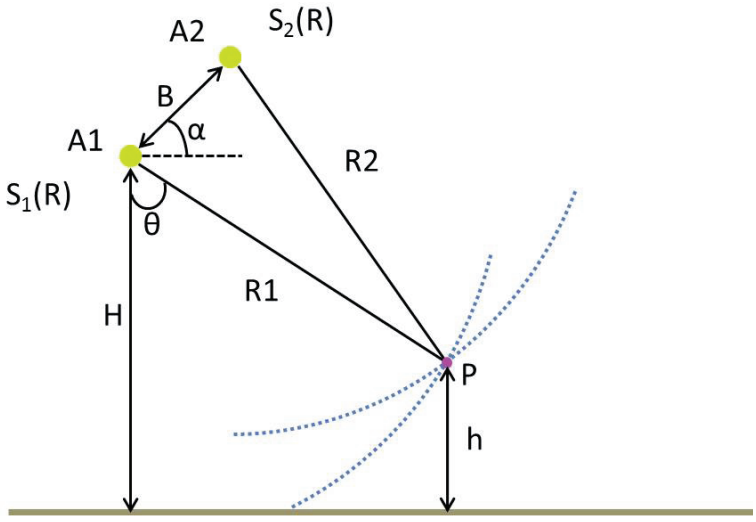

(b)

Figure 6.1: Diagram of radar cross-track interferometry.

6.2 Correlation Estimation

A fundamental quantity in SAR interferometry is the correlation. The correlation is calculated on a pixel by pixel basis, with each pixel being an aggregation of the single-look pixels (highest resolution) that make up the SAR image. Here, each pixel is of the correlation is computed by

$$\gamma = \frac{E[z_1 z_2^*]}{\sqrt{E[|z_1|^2]}\sqrt{E[|z_2|^2]}} \ , \tag{6.3}$$

where the field observed at each pixel is treated as a zero-mean complex random variable z, and z_1 and z_2 are the random variables for the two channels, respectively. (6.3) can be seen as a normalized inner product of two random vectors. When the two vectors are constant vectors, then the magnitude of correlation will be one.

In practice, the expectation in (6.3) can be computed from the sample average of the neighboring pixels under the assumption that the random process is ergodic in the neighborhood of the pixel [40]. The estimator is given as

$$\hat{\gamma} = \frac{\sum_{i=1}^{L} z_{1i}\, z_{2i}^*}{\sqrt{\sum_{i=1}^{L} |z_{1i}|^2}\sqrt{\sum_{i=1}^{L} |z_{2i}|^2}} = |\hat{\gamma}| e^{j\phi_{\hat{\gamma}}}. \tag{6.4}$$

The magnitude of correlation is an indication of the level of the correlation between the two channels. Decorrelation can be caused by thermal noise, slight differences in look angles to the scatterer, temporal variations of the targets, or spatial variation over the averaging region. In the case of higher correlation, the error of the interferometric phase will be smaller.

6.2.1 Statistics of Correlation and Interferometric Phase

The probability density function of the correlation for a given number of looks is given by [40],

$$P_L(|\hat{\gamma}|; |\gamma|) = 2(L-1)(1-|\gamma|^2)^L |\hat{\gamma}| (1-|\hat{\gamma}|^2)^{L-2} \times {}_2F_1(L, L; 1; |\gamma|^2 |\hat{\gamma}|^2) \ , \tag{6.5}$$

where ${}_2F_1(\cdot)$ is the hypergeometric function and L is the number of looks. The expectation of $|\hat{\gamma}|$ is formed by

$$E_L(|\hat{\gamma}|;|\gamma|) = \frac{\Gamma(L)\Gamma(1+1/2)}{\Gamma(L+1/2)} \times {}_3F_2(3/2, L, L; L+1/2; 1; |\gamma|^2) \times (1-|\gamma|^2)^L, \quad (6.6)$$

in which ${}_3F_2(\cdot)$ is the generalized hypergeometric function. It can be seen that the expectation of the magnitude of $\hat{\gamma}$ depends on the true value of correlation magnitude $|\gamma|$ and the number of looks, L. A simulation of the mean value of $|\hat{\gamma}|$ is shown in Figure 6.2(a), and its standard deviation is shown in Figure 6.2(b). It can be seen that the magnitude of the correlation estimation $E[|\hat{\gamma}|]$ is biased upward. To improve the measurement accuracy of the correlation, more looks can be used at the expense of resolution in the final InSAR image. This assumes a stationary process across the pixels being averaged and may be unlikely if L is large.

The results of estimation of the correlation for the UMass Ka-band InSAR with $L = 50$ is shown in Figure 6.3(a). It can be seen that the correlation magnitude is about 0.4 in the near range and decreasing toward zero in the far range where the signal-to-noise ratio (SNR) is much lower. The generally low correlation results from the low SNR which is a direct effect of the low transmitting power of the radar less than 30 dBm.

Generally, the estimation of correlation phase is unbiased. However, due to phase wrapping it could be a biased estimator if the true value phase is not zero and the magnitude of correlation is low or the number of looks is small or if there is an external signal in the data, such as signal leakage within the radar electronics. Multi-looking is necessary to decrease the bias in such cases. The probability density function of the phase for a certain number of looks L is given by [41]

$$P_L(\phi_{\hat{\gamma}}) = \frac{(1-|\gamma|^2)^L \Gamma(L+1/2)\beta}{2\sqrt{\pi}\Gamma(L)(1-\beta^2)^{(L+1/2)}} + \frac{(1-|\gamma|^2)^L}{2\pi} {}_2F_1(L, 1; 1/2; \beta^2), \quad |\gamma| < 1 \quad (6.7)$$

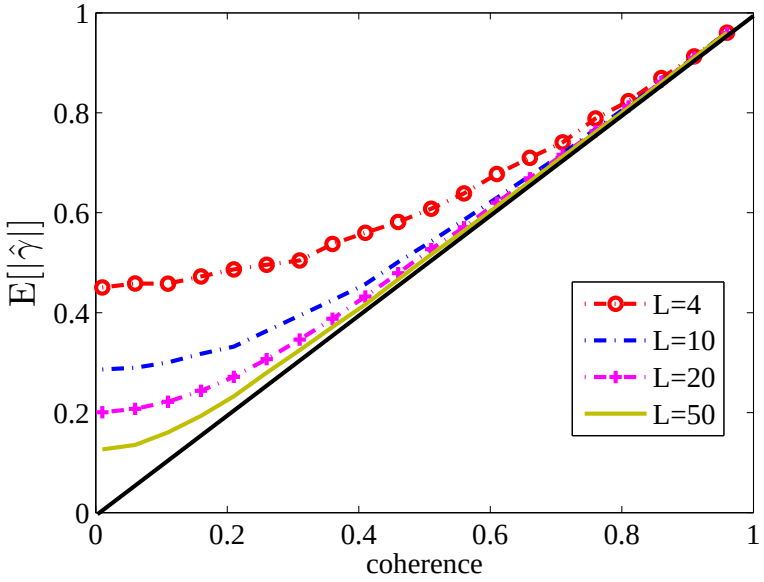

(a)

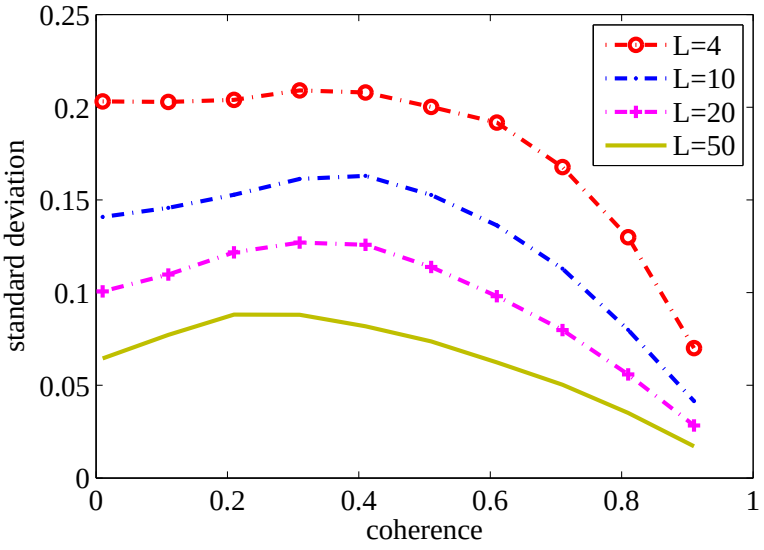

(b)

Figure 6.2: Simulation result of magnitude of correlation versus true correlation value and number of looks..

where $\beta = |\gamma| cos(\phi - \phi_\gamma)$ and ϕ_γ is the expected differential phase.

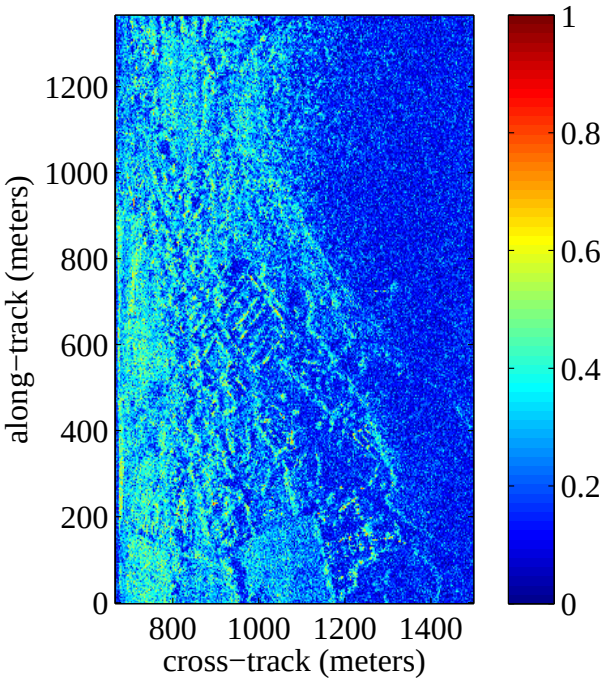

(a)

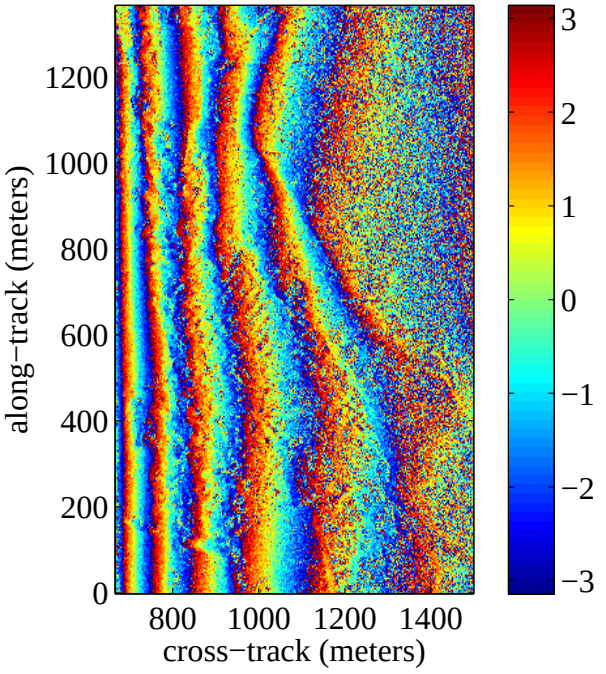

(b)

Figure 6.3: The slant range images of estimated correlation magnitude and phase with $L = 50$. The platform height is 696 meter.

The probability density functions for different number of looks with $\phi_\gamma = 0$ degrees are plotted in Figure 6.4, which are nearly Gaussian for a large number of looks (e.g. $L > 10$). The simulation results of the correlation phase $\phi_{\hat{\gamma}}$ are shown in Figure 6.5.

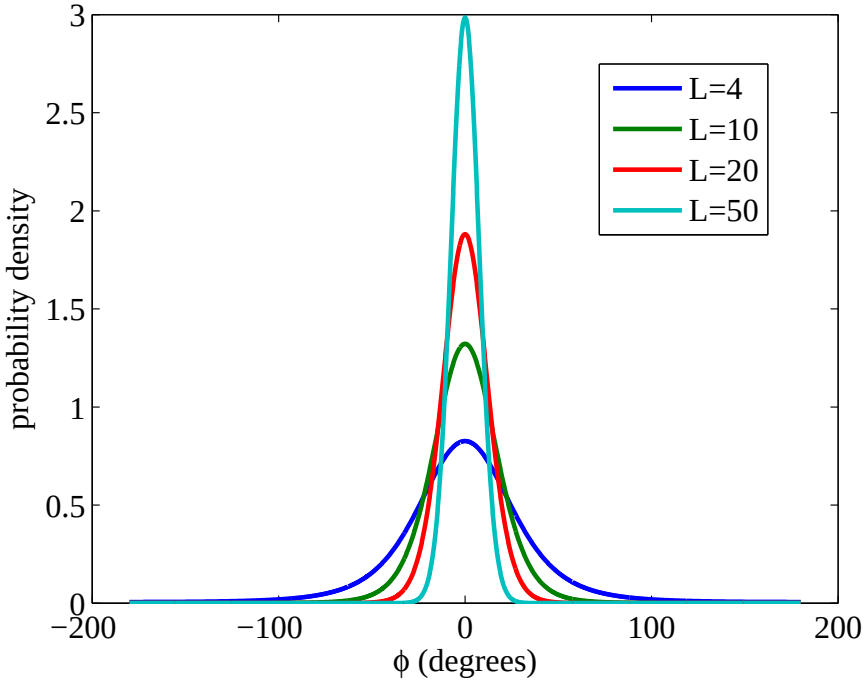

Figure 6.4: Probability density function of multi-looking interferometric phase for correlation=0.6.

The mean and the standard deviation of the estimated phase can be calculated from the pdf of $\phi_{\hat{\gamma}}$ from (6.7) as well, as illustrated in Figure 6.6. It can be seen that the calculation results are in agreement with the simulation results. When the correlation is 0.2, the standard deviation of the interferometric phase for $L = 50$ is 38 degrees, which corresponds to a little more than one-tenth of a wavelength ($\lambda_c = 8.6$mm) of the differential path length for the target reaching one antenna with respect to the other.

6.3 Topography Measurement

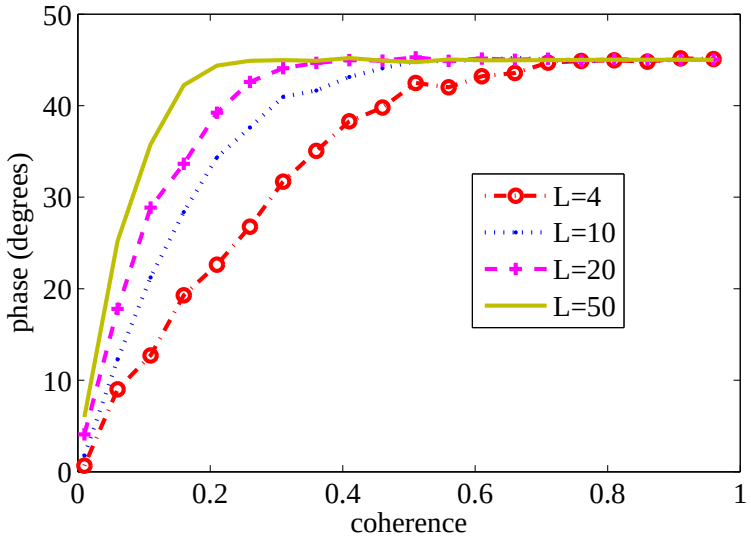

(a)

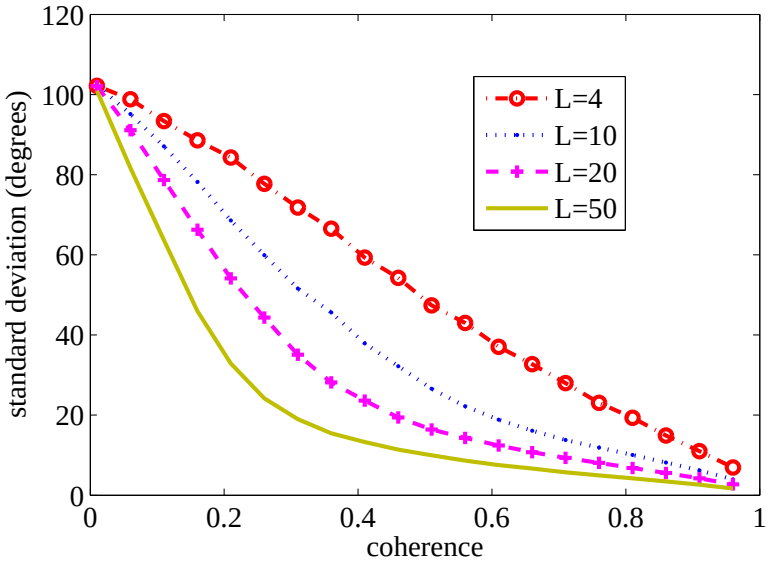

(b)

Figure 6.5: Simulation results of correlation phase, (a)mean value and (b)standard deviation. The true value of phase is 45°.

6.3.1 Flat Earth Phase and Height Ambiguity

The mapping from the interferometric phase, ϕ_γ, to the ground topography is given by

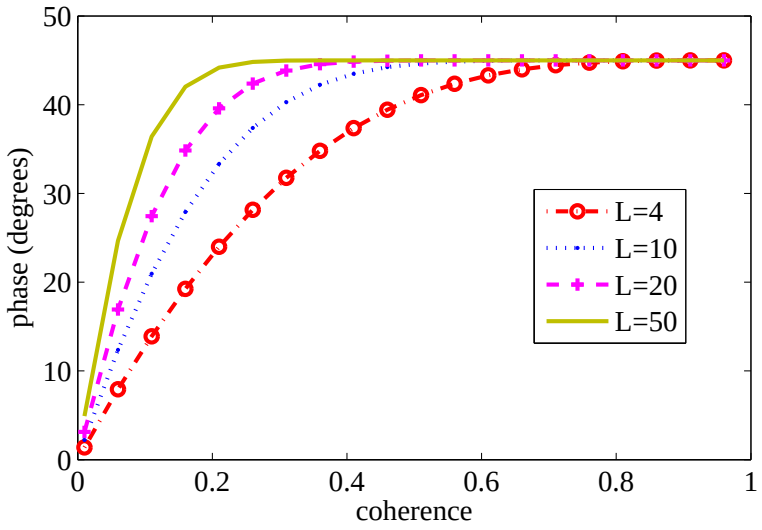

(a)

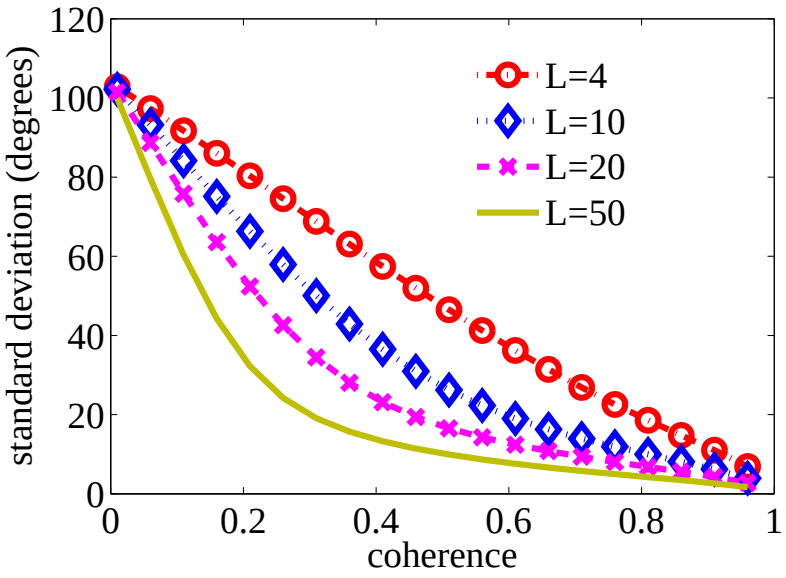

(b)

Figure 6.6: Calculation results of correlation phase based on its probability density function, (a)The mean value and (b)The standard deviation. The true value of phase is 45°.

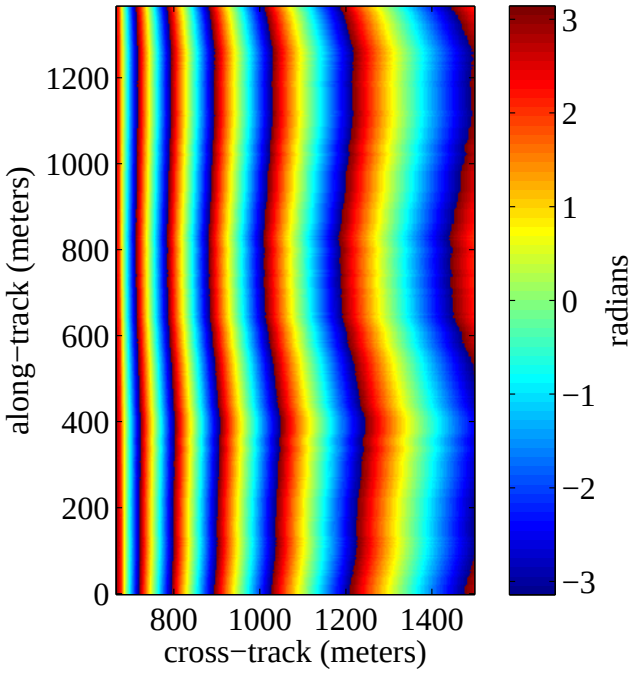

Figure 6.7: The flat earth interferometric phase for the same scene shown in Figure 6.3.

$$h = H - R_1 \cos\left(\alpha + \sin^{-1}\left(\frac{c\,\phi}{2\pi f_0 B}\right)\right). \tag{6.8}$$

In order to determine the topography, there are two steps that must be performed prior to this calculation. That is, to i.) remove the flat earth phase, and ii.)perform phase unwrapping if necessary.

The flat earth phase is the phase change with the radar swath due to the change of look angle θ, even in the absence of topographic relief. An example of the flat earth phase is shown in Figure 6.7. The variation of the color strips in the along-track direction is caused by the platform motion. It shows that this effect is more distinguishable in the far range.

The existence of topographic relief will distort the flat earth phase, as shown in Figure 6.3. The effect of existence of topographic relief is illustrated in Figure 6.8. Hence the measured differential phase can be divided into two parts, one is the flat

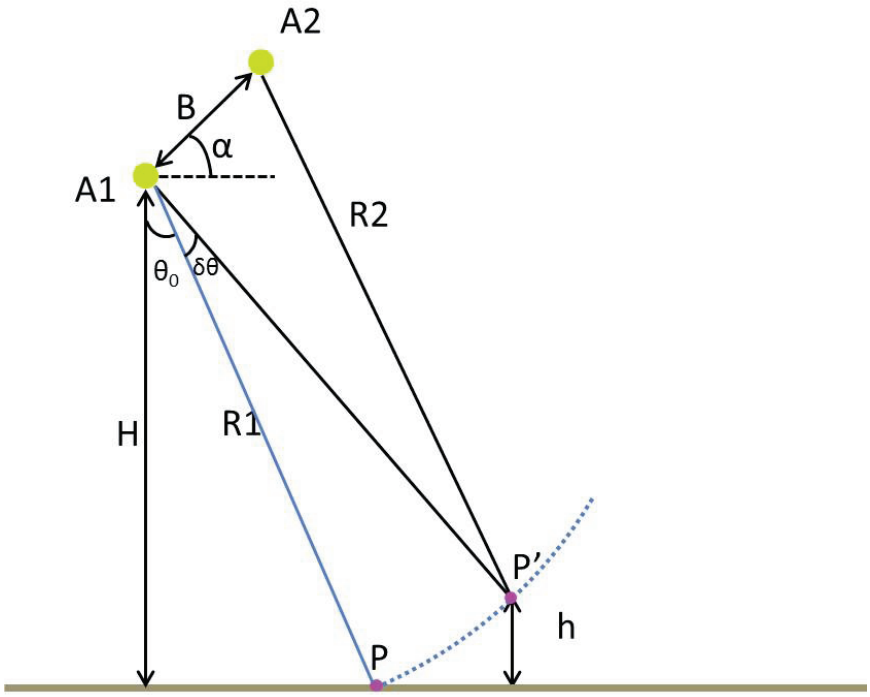

Figure 6.8: The effect of topographic relief to the look angle θ. The look angle is θ_0 if there is no topographic relief (target P), and it changes by $\delta\theta$ for the same range if the topographic relief presents (target $P^{'}$).

earth phase, and the other is the distortion phase from the known topographic relief.

The differential phase, ϕ, versus the look angle, θ, if there is a topographic relief can be approximated from (2.40) and (2.43), as in

$$\begin{aligned} \phi &= -\frac{2\pi}{\lambda_c} B\sin(\theta_0 + \delta\theta - \alpha) \\ &\simeq -\frac{2\pi}{\lambda_c} B\sin(\theta_0 - \alpha) - \frac{2\pi}{\lambda_c} B\cos(\theta_0 - \alpha)\delta\theta \,. \end{aligned} \tag{6.9}$$

The first term in (6.9) is the flat earth phase and the second term is the distortion phase caused by the topographic relief. After subtracting the flat earth phase from the measured phase ϕ, the remaining phase is called the flattened interferogram, given by

$$\begin{aligned}\phi_{flat} =& -\frac{2\pi}{\lambda_c} B\cos(\theta_0 - \alpha)\delta\theta \\ \simeq& -\frac{2\pi}{\lambda_c} B\cos(\theta_0 - \alpha)\frac{h}{R_1 \sin\theta_0} \\ =& k_z h \quad ,\end{aligned} \tag{6.10}$$

where k_z is the interferometric phase sensitivity to topography, by $k_z = \frac{\partial\phi}{\partial z}$, and given by

$$k_z = -\frac{2\pi B\cos(\theta_0 - \alpha)}{\lambda_c R_1 \sin\theta_0} \quad . \tag{6.11}$$

Since the measured phase lies between $[-\pi\,, \pi]$, the linear relation between the flattened phase, ϕ_{flat}, and the topographic relief, h, only holds for a period of 2π, thus having the potential of causing a height ambiguity. This height ambiguity, h_{amb}, corresponding to a 2π radians change in phase and is given by

$$h_{amb} = \frac{2\pi}{k_z} = \frac{\lambda_c R_1 \sin\theta_0}{B\cos(\theta_0 - \alpha)}. \tag{6.12}$$

In the absence of a known digital elevation model, a process of phase unwrapping in two dimensions is needed, a process which can be computationally expensive and prone to error.

6.3.2 Using an external DEM

The above procedure of removing the flat earth phase and phase unwrapping can be avoided by using a digital elevation model (DEM) from an external source. An illustration of using an external DEM is shown in Figure 6.9. The external DEM could be taken with different technologies, such as ground surveys, LIDAR, photogrammetry or InSAR-derived topography obtained from different missions. (e.g. the Shuttle Radar Topography Mission, SRTM[42].)

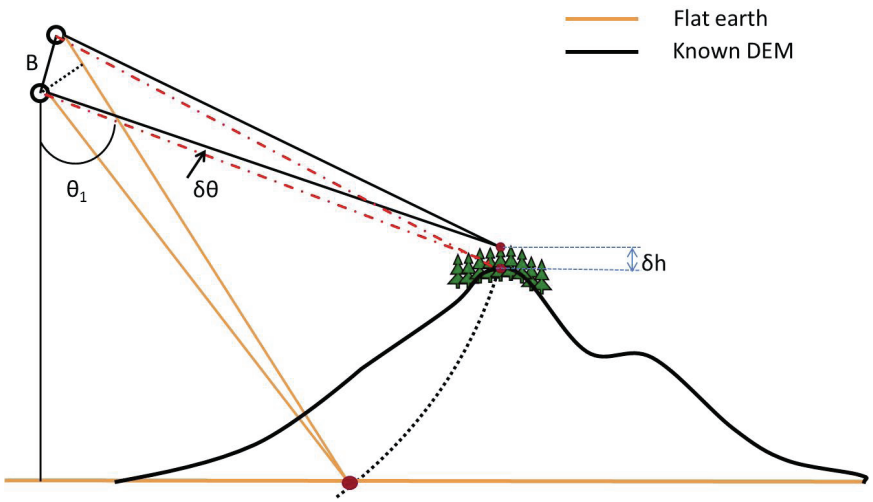

Figure 6.9: Illustration of the process of subtracting the known DEM.

It is generally expected that the change of look angle from the known DEM to the measured DEM can be small. Similar to (6.9), the measured phase ϕ can be written as

$$\phi \simeq -\frac{2\pi}{\lambda_c} B\sin(\theta_1 - \alpha) - \frac{2\pi}{\lambda_c} B\cos(\theta_1 - \alpha)\delta\theta\,, \tag{6.13}$$

where the first term is the phase corresponding to the external DEM, and the second term is the differential phase between the measured topography and the external DEM. By subtracting the phase of the external DEM from the total measured interferometric phase, ϕ, which is is caused by a small change in the look angle, $\delta\theta$, the remaining differential phase relates to the differential height between the two DEMs as

$$\begin{aligned} \delta\phi \simeq & -\frac{2\pi}{\lambda_c} B\cos(\theta_1 - \alpha)\frac{\delta h}{R_1 \sin\theta_1} \\ = & k_z \delta h \quad . \end{aligned} \tag{6.14}$$

In such a case, there will be no need for the phase unwrapping as long as $\delta\phi$ lies in the range $[-\pi, \pi]$.

The height ambiguity of the UMass Ka-band InSAR system described by Table 4.1 is given in Figure 6.10. This figure shows that this method works better in the far range where the height ambiguity is larger, but it will work in the near range as well in the case that δh is not very large.

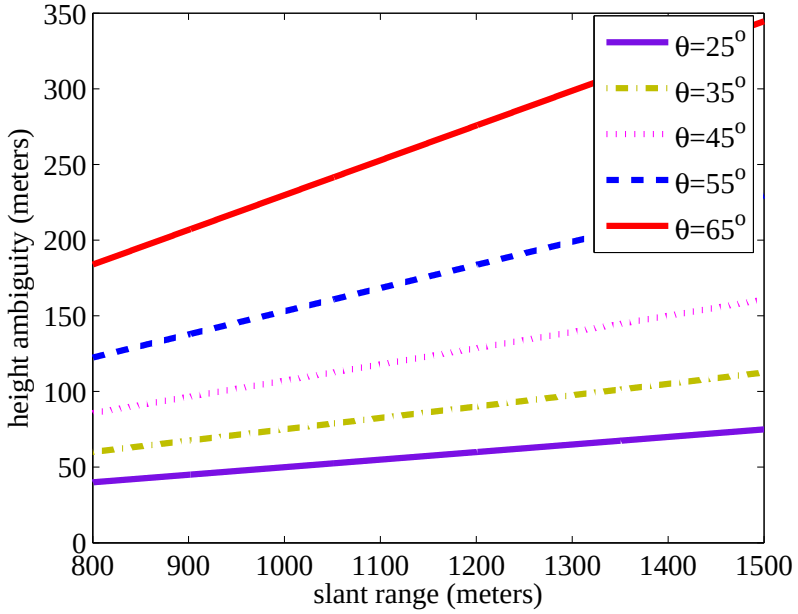

Figure 6.10: The height ambiguity of the Umass Ka-band InSAR as a function of slant range for different look angles.

6.3.2.1 The external DEM

The external DEM used in this dissertation was obtained from MassGIS, the Massachusetts Office of Geographic Information [43]. This digital elevation model is produced from the the digital terrain model (DTM) point elevation files, which are obtained from an analytical stereo plotter. The accuracy of the DEM, according to [43], is ±1.5 meters. The spacing of the grid points are 5 meters by 5 meters.

6.3.3 Geo-registration

In the previous section, the phase of an external DEM was subtracted from the measured phase, it was accomplished in the geodetic map coordination since the

available DEMs are usually in the this format. Hence, geo-registration is a necessary procedure for interferometric processing.

Geo-registration is a mapping procedure from the radar image pixels to the geodetic map pixels. Every pixel in the radar image may be mapped to more than one pixel in the geodetic map depending on the beamwidth and the resolution of the map. A flowchart of the geo-registration steps is shown in Figure 6.11.

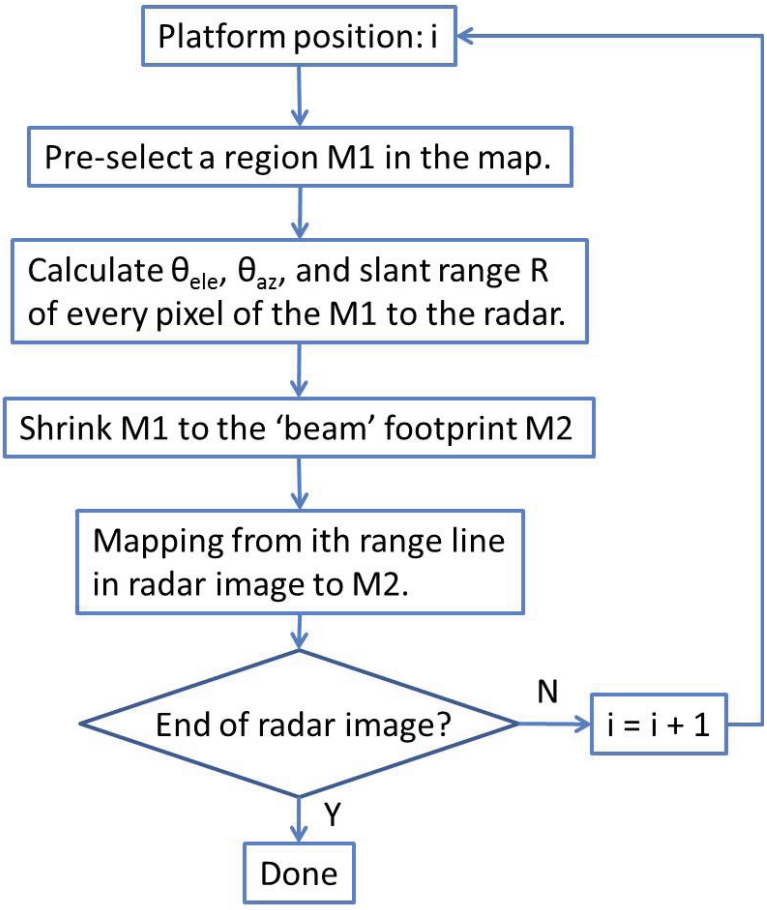

Figure 6.11: The flowchart of geo-registration.

For each platform position i, a region $M1$ in the map is selected. The region $M1$ is larger than the radar beam footprint.

Since the three-dimensional coordinates (x, y, z) of each pixel in the map are known from the external DEM, the elevation angle, θ_{ele}, the azimuth angle, θ_{az}, and the slant range, R_p, from each pixel in $M1$ to the radar can be calculated.

Based on the estimations of the angles θ_{ele}, θ_{az}, the slant range, R_p , the antenna azimuth beamwidth θ_{bw}, and the antenna pointing direction θ_{ant} (which is derived from Doppler centroid estimation), each pixel in $M1$ can be determined whether it lies within the beam footprint. Hence the pre-selected region $M1$ now reduces to the region $M2$ which represents the radar beam footprint. It should be noted that unlike a real aperture radar, the beam footprint of a SAR has a constant width, ΔX in the azimuth direction since it only depends on the antenna length. The pixels in $M2$ need to simultaneously satisfy the following conditions:

$$\begin{aligned} r_{min} \leq R_p \leq r_{max} \\ |\theta_{az} - \theta_{ant}| \leq \theta_{bw} \\ |\theta_{az} - \theta_{ant}| \cdot R_p \leq \Delta \mathrm{X} \quad , \end{aligned} \tag{6.15}$$

where r_{min} and r_{max} is the minimum and maximum slant range within the beam footprint, θ_{az} is azimuth angle with respect to a reference direction (e.g. the true North), θ_{ant} is the azimuth angle of the antenna boresight, θ_{bw} is the azimuth antenna beamwidth. The first equation sets the limits of the slant range, the second equation sets the spanning angles in the azimuth dimension, and the third equation defines the azimuth resolution, ΔX.

Next the i^{th} range line in the radar image can be mapped to $M2$ based on the range R_p of its pixels. A diagram of the geo-registration steps is shown in Figure 6.12. Once completed for a particular range line, and the above steps are repeated until the entire radar image is mapped.

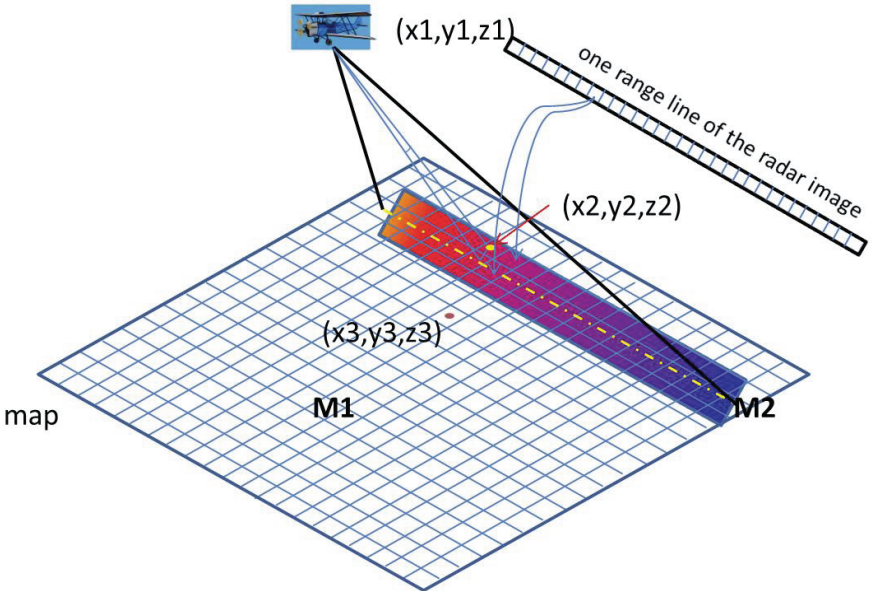

Figure 6.12: Illustration of geo-registration process.

6.3.4 The Final DEM

The final DEM is the result of the summation of the differential DEM, δh, given by (6.14), and the external DEM. The resolution of an external DEM is coarse, typically on the order of tens of meters, which means it needs to be interpolated to get same spatial sampling rate as the SAR image. An example of the resulting differential DEM and the final DEM are shown in Figure 6.13(b) and Figure 6.13(c), where it can be seen that the resolution is significantly improved.

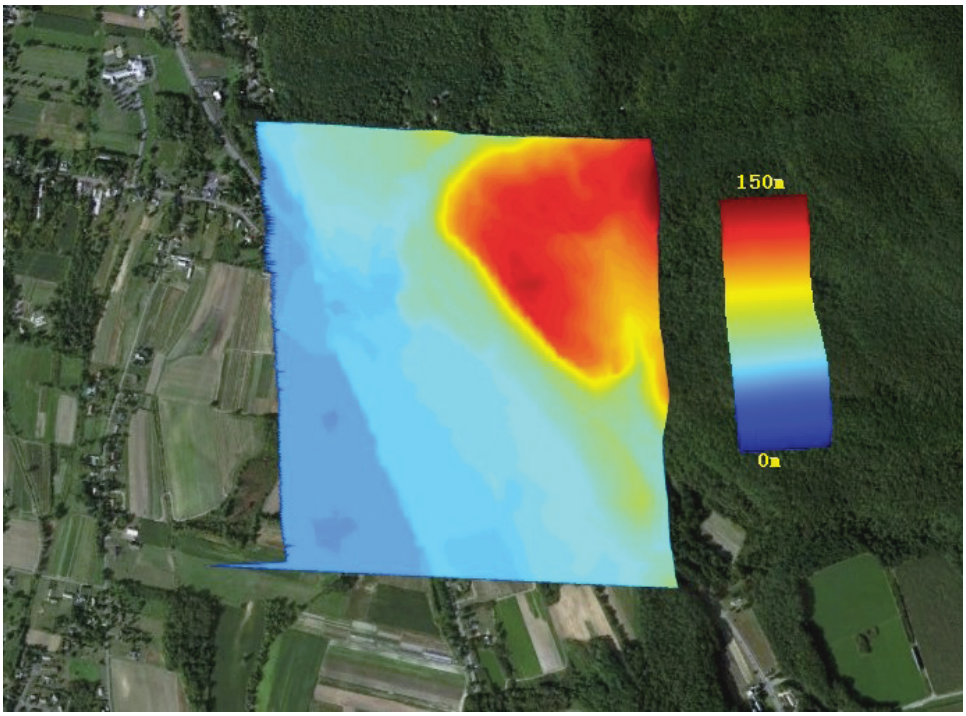

(a)

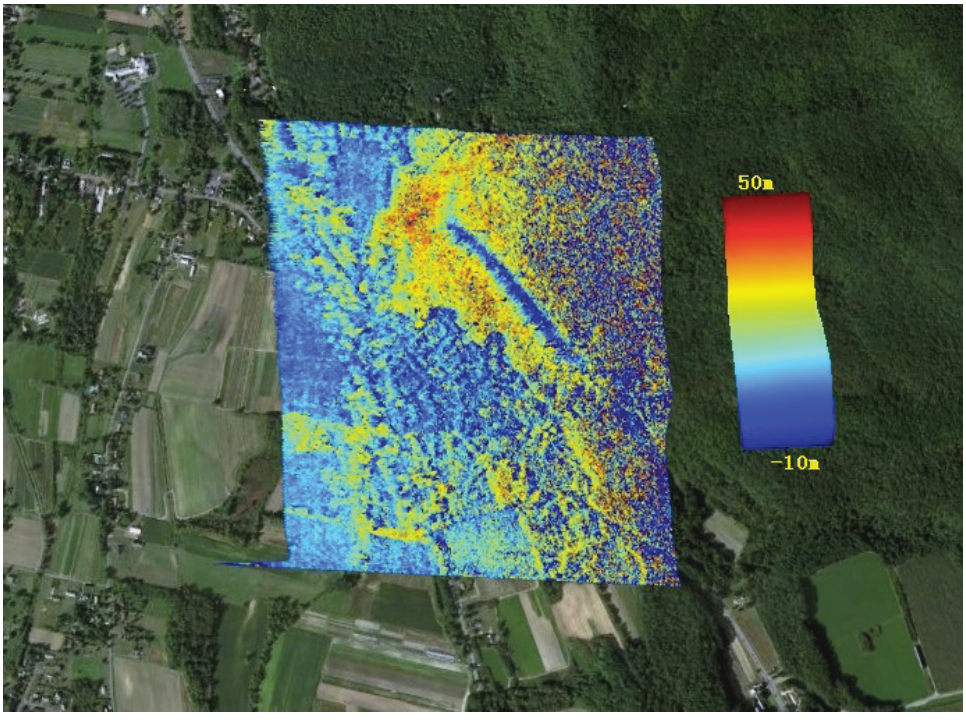

(b)

Figure 6.13: (a) The known DEM. (b) The differential DEM. (c) The final DEM, the colormap is wrapped by every 50 meters

.

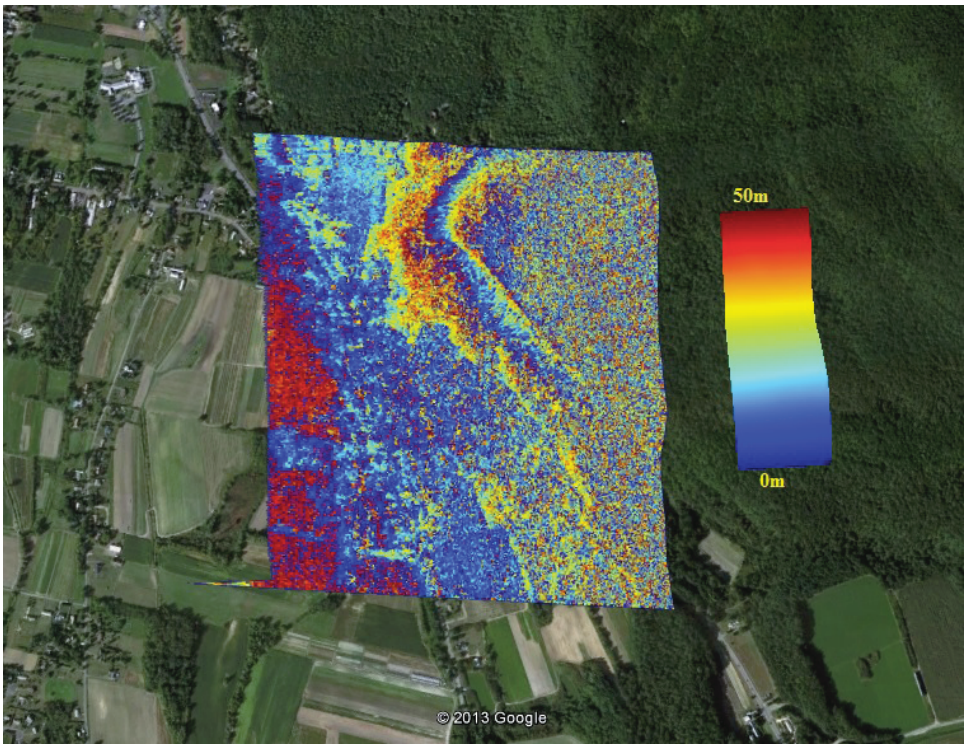

(c)

Figure 6.13: Continued. (a) The known DEM. (b) The differential DEM. (c) The final DEM, the colormap is wrapped by every 50 meters

.

CHAPTER 7

CONCLUSION AND FUTURE WORK

This dissertation aimed to investigate the motion compensation algorithm for the airborne radar and to investigate the capability of topographic measurement of the 35 GHz airborne interferometric radar designed by the Microwave Remote Sensing Laboratory at University of Massachusetts Amherst.

In chapter 3, the short-term and long-term phase stability of the radar receiver was characterized. The SAR processing procedures were described in detail in chapter 4. The image blurring issue in the range dimension was solved through a phase error model. The result of estimation suggests that the blurring was caused by a high frequency phase error. The frequency of the phase error is about 10 kHz, which matches the 15-meter distance between the real scatterer response and the "ghost" response for a bright scatterer. After correcting for the phase error, the image resolution and contrast was enhanced to the extent that it can be further processed to generate the map of topographic height.

Following the phase error correction, the radar data was processed both in range and along-track dimension, and the single-look complex SAR images and multi-look SAR images are generated. The imaging ability of the Ka-band FMCW radar system was demonstrated. To increase the processing accuracy, the Doppler centroid was estimated as a two-dimensional map.

In chapter 5, the analysis of motion effects on the SAR images was carried out and was followed by the motion compensation procedures for the UMass Ka-band system. The error analysis of the motion compensation has also been done. Since

the GPS employed on the airborne platform can only provide sub-meter accuracy, a large error is expected in the motion compensation result.

The interferometric processing result was shown in chapter 6. The map of topographic height was generated in the form of "strip map" with the aid of an external DEM. This becomes one of the few reported terrain height at Ka-band, which can be utilized in a variety of applications. From the simulated curve in Figure 6.5, the standard deviation of the interferometric phase is about 20° for typical scenes and it varies for different scatterers. The 20° phase error translates to a height error of 5.6 meters. The horizontal resolution for this result is 5.1 meters in range and 6.3 meters in along-track dimension. In the future research, corner reflectors could be deployed such that the SAR image quality and topographic height accuracy in different ranges can be evaluated in a point scatterer response level.

The motion effects on the SAR interferometry have been investigated. Both translational and rotational motion effects on the measured topographic height have been discussed. It shows from the analysis that the induced error in topographic height is comparable to that induced by decorrelation. Finally, the error sources in the topographic measurement are summarized in the Appendix.

7.1 Unique Contributions

In this dissertation, the following unique contributions have been made,

(1) A solution to a cross-track image blurring issue in the SAR imaging system.

The image blurring issue which occurs in the range dimension has made it difficult for further processing. The blurring not only smear the magnitude image, but also corrupting the phase. Therefore it is difficult to retrieve any useful information from the blurred interferometric SAR image.

To solve this issue, a phase error model, which connects the blurring to a phase error in the radar raw data, is built. Specifically, the phase error should have a

form of high frequency according to the observation of the blurred image. The Phase Gradient Algorithm (PGA), which is originally used in autofocus of azimuth data, is utilized to estimate the phase error directly from the radar raw data. The blurred images are de-blurred after the correction of the phase error in the radar raw data. Hence, the subsequent SAR and interferometric processing can be proceeded without being affected by the phase error.

(2) Analysis of the effects of attitude variation on the SAR image and propose a novel attitude motion compensation method.

In processing the airborne SAR data, motion effects have to be evaluated and properly compensated for based on the measured motion data. As far as the knowledge of the author, in the existing literature, only the effect of the trajectory deviation on the signal phase history was discussed. However, the effect of angular motion on the signal amplitude is seldom considered, since the antenna pattern was assumed to be wide such that the amplitude variation can be ignored. In this dissertation, the effect of angular motion is analyzed, and a compensation method for angular motion is proposed.

Since the attitude deviation is typically a slow process comparing to the synthetic aperture time, the attitude deviation can be linearized during an aperture time. Hence its effect on signal amplitude is found to be a change in signal Doppler bandwidth, which determines the azimuth resolution of the output SAR image.

In this dissertation, The effect of attitude deviation is compensated for in the frequency domain by a correction factor which depends on the measured attitude parameters. Through attitude motion compensation, the image quality can be further improved in terms of resolution and signal-to-noise ratio.

(3) Produce a strip map of the reflectivity at 35 GHz and the topographic height for an area in western Massachusetts.

The imaging capability of the UMass airborne Ka-band InSAR system, both the reflectivity imaging and interferometric imaging capability, are demonstrated through a sequence of signal processing steps starting from the radar raw data. As a result, a strip map of areas in western Massachusetts, in the format of reflectivity and topographic height, was generated. As far as the knowledge of the author, there are only two other reported single-pass Ka-band interferometry result in the literature. Being the only airborne Ka-band InSAR employing the FMCW architecture, the produced dataset is valuable for research within the remote sensing community in many areas, to name a few, forest remote sensing, urban remote sensing, and the radar hardware and software platform will provide a low-cost solution to the future imaging application in the 35 GHz frequency range. In addition, the signal processing software can be easily adapted to a FMCW radar operating with a different carrier frequency.

7.2 Future Work

In the future, certain work can be done to improve the performance of the radar system by the improvement of the signal processing and motion compensation algorithm.

First of all, the source causing the phase error and image blurring is still not clear, however, based on several facts it should come from the aircraft, e.g., the power supply: i.) a UMass S-band airborne system has a similar blurring issue; ii.) the lab bench test of the radar system with a 100-meter cable simulating a distant scatterer does not show the blurry phenomenon in the target response. It will be useful to narrow down the possible sources by taking measurement on the airplane in the future research.

Second, the radar system can increase its transmit power to get better signal-to-noise ratio, hence better topography measurement accuracy. Currently, the transmitted power is less than 30 dBm,

Third, the SAR processing programme can be implemented in more efficient way, such as written in C++, hence achieve the real-time imaging capability. An integrated motion compensation algorithm, which combines both the GPS and the IMU data, can be developed in the future to improve the compensation result.

Fourth, the current collected Ka-band data and future collected data can be utilized in remote sensing application, such as dynamic differential topography monitoring, for example, the forest change and ground deformation monitoring.

APPENDIX

ERROR SOURCES IN AIRBORNE SAR INTERFEROMETRY

In the previous chapters, the measurement procedures of topography using a Ka-band airborne FMCW InSAR has been presented. This is the first single-pass topography result at this frequency and with an FMCW radar. As a light weight and low cost radar, the FMCW radar has its advantage of simplified RF electronics with respect to a pulsed radar, and its ease of integration with an airborne platform.

In this chapter, some aspects of the FMCW radar will be discussed from a system design point of view. The translation from the airborne FMCW radar system parameters to topographic height errors will be discussed, and thus can serve as a guideline of airborne FMCW radar system design.

A.1 Error Sources of Topography Measurement

The first specification of the topographic height will be the height uncertainty and offsets, in another word, the error of the topography measurements. In this section, the error sources for the estimation of topographic height will be discussed.

A.1.1 Decorrelation

As shown in Chapter 6, the decorrelation between the two interferometric channels will increase the variance of the interferometric phase. The different sources of decorrelation have been studied in [44]. Generally, the causes include decorrelation due to thermal noise (SNR), geometric decorrelation and temporal decorrelation. In the case of this single-pass Ka-band InSAR, there is no temporal decorrelation,

hence the decorrelation is dominated by the thermal noise decorrelation and geometrical decorrelation. Geometric decorrelation refers to slight differences in the viewing geometry of the InSAR such that the scatterer response is not precisely the same for the two antennas of the interferometric system. This geometric decorrelation can be broken down into surface decorrelation and volume decorrelation terms. The amount of surface decorrelation can be calculated according to

$$\rho_{surface} = 1 - \frac{2B_{\perp}R_y \cos\theta}{\lambda r}, \tag{A.1}$$

which is derived in [44] while assuming uniformly distributed and uncorrelated scatterers, where $B_{\perp}$ is the vertical baseline length, R_y is the ground range resolution, and θ is the off-nadir look angle. It can be seen from Equation (A.1) that surface decorrelation depends on the vertical baseline to wavelength ratio (electrical length), the range to ground range resolution ratio and the look angle. For the Ka-band radar, its slant range resolution is 1.5 meters, the baseline length is 8.0 centimeters, and the carrier wavelength is 0.86 centimeters. Hence the amount of surface correlation varies with the off-nadir angle, and its values for several different off-nadir angles are plotted in Figure A.1. It shows that amount of surface decorrelation for the Ka-band radar is less than 5%, which is due to the very small difference in viewing geometry for the two antennas that make up the interferometric baseline.

Figure A.2 shows images of the correlation magnitude in the form of "strip maps" made by the Ka-band InSAR as it passes over the terrain. It can be seen that the correlation is relatively low. A more quantitative assessment of the correlation magnitude is illustrated by the histogram shown in Figure A.3.

From the above simulation of surface decorrelation, it is evident that the decorrelation is the result of thermal and volume decorrelation. The amount of thermal noise decorrelation can be calculated from the estimated signal-to-noise ratio (SNR).

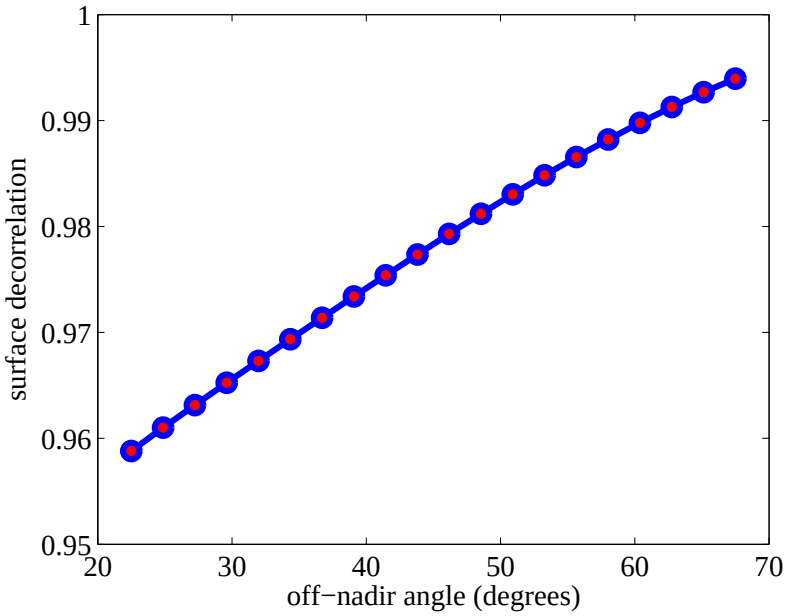

Figure A.1: The amount of surface decorrelation as a function of off-nadir angle.

To estimate SNR, a single look complex (SLC) SAR image is first divided into multiple two-dimensional blocks, just as in the estimation of Doppler centroid in Section 4.4. Each block is then transformed to the Doppler frequency domain through a one-dimensional Fourier transform along the azimuth dimension. Within each block the square of the magnitude are averaged along the range dimension resulting in a one-dimensional waveform along the azimuth dimension. This waveform is an averaged power spectrum, which can be decomposed into two components, one is the signal power and the other is the noise power, as shown in

$$\begin{aligned} & < |v_s e^{j\phi_s} + v_n e^{j\phi_n}|^2 > \\ = & < v_s^2 + v_n^2 + 2 v_s v_n \cos(\phi_n - \phi_s) > \\ = & < v_s^2 > + < v_n^2 >, \end{aligned} \tag{A.2}$$

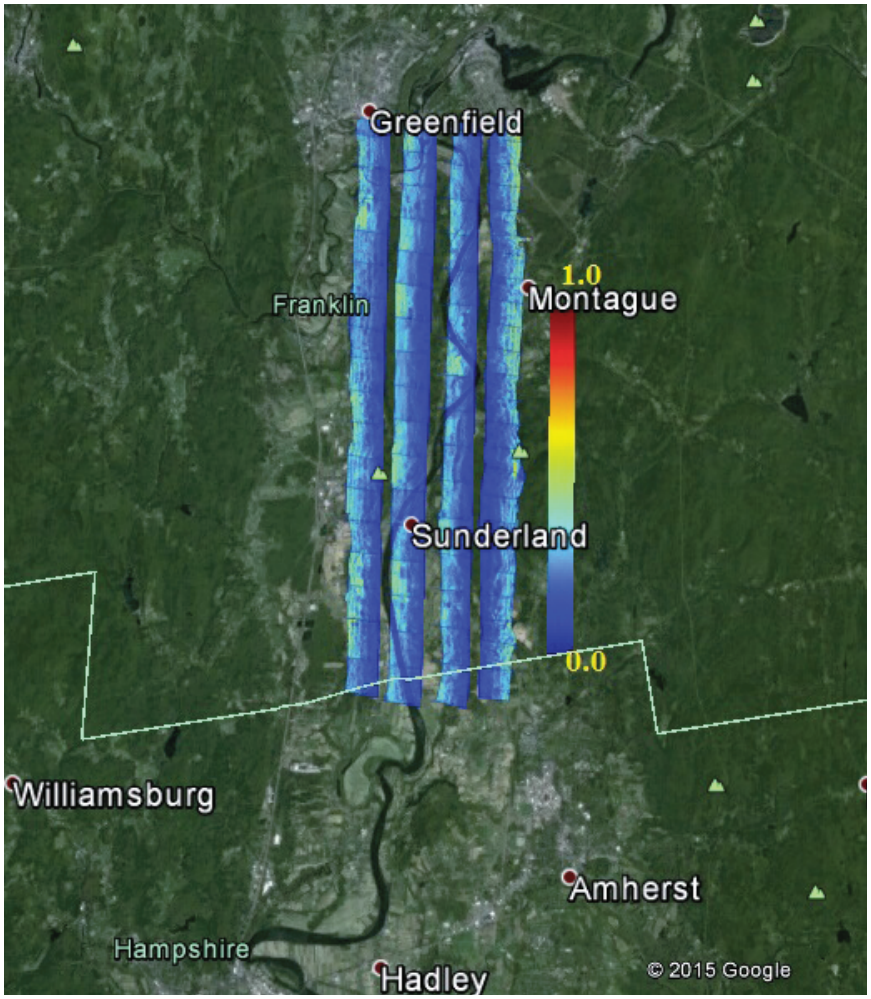

Figure A.2: The stripmaps of the correlation magnitude. The color scale is from 0 to 1.

where the signal, v_s, and the noise, v_n, are assumed to be independent random variables, v_s is stationary and ergodic in the range direction, and <> is the sample average along range dimension. An example of the signal is shown in Figure A.4.

To continue, the frequency domain data is fitted to a smooth curve whose shape is determined by the antenna pattern along the azimuth direction. The minimum of the fitted curve is used as the estimation of the noise power, since the signal power is zero at the minimum which corresponds to a null of the azimuth antenna pattern, since the shape of the Doppler spectrum follows the antenna pattern along the azimuth

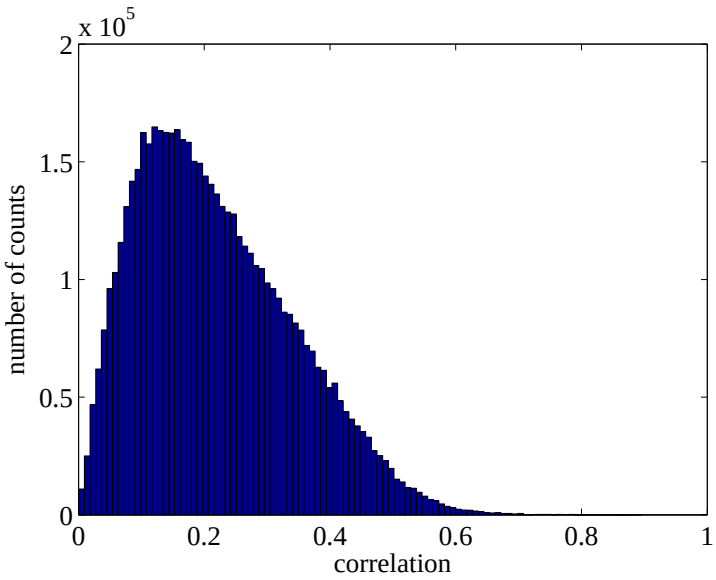

Figure A.3: The histogram of the correlation magnitude.

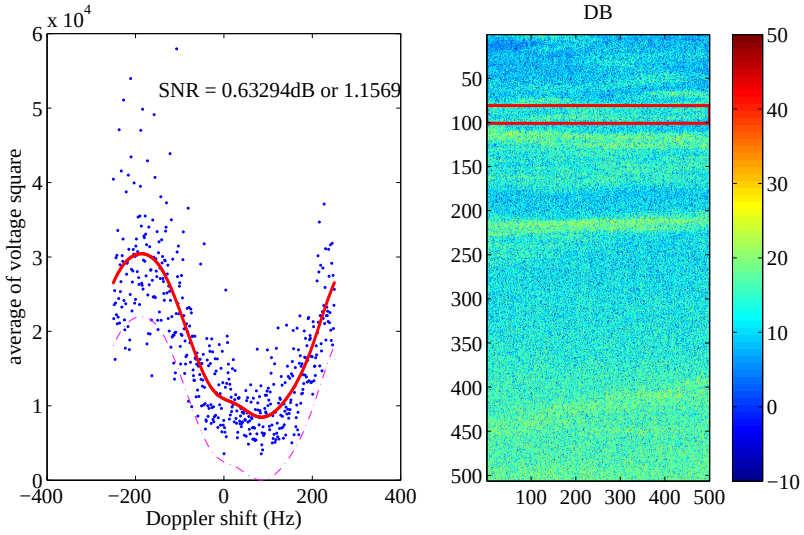

Figure A.4: Example of SNR estimation. The left figure shows the averaged power(dots). The dashed line shows the signal power after subtracting the noise power. The right figure shows the original SLC block.

direction. A second example in Figure A.5 shows an estimation of a lower SNR region.

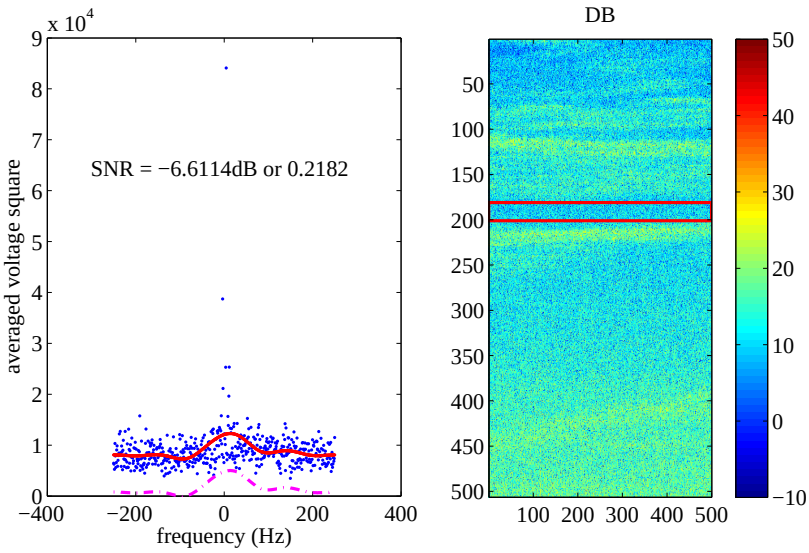

Figure A.5: Example of SNR estimation of a lower SNR region. The left figure shows the averaged power(dots). The dashed line shows the signal power after subtracting the noise power. The right figure shows the original SLC block.

An example of the estimated SNR comparing with the multi-looked (25 pixels in azimuth, 2 pixels in range) SAR image is given in Figure A.6. The thermal correlation corresponding to the estimated SNR in Figure A.6 is shown in Figure A.7, together with the calculated correlation of the same scene. It can be seen that the estimated correlation is generally larger than the actual calculated one in the near- and mid-range. This suggests that the decorrelation in these ranges is not only caused by the thermal decorrelation but also the volume decorrelation.

This can be seen in a illustrated example, where the amount of volume decorrelation is derived from the estimated total correlation and the estimated thermal correlation calculated from the SNR, as shown in Figure A.8. Since the error of the derived volume decorrelation is coupled with the error of the SNR estimation, the error of the volume decorrelation is large if the SNR is small, as given in

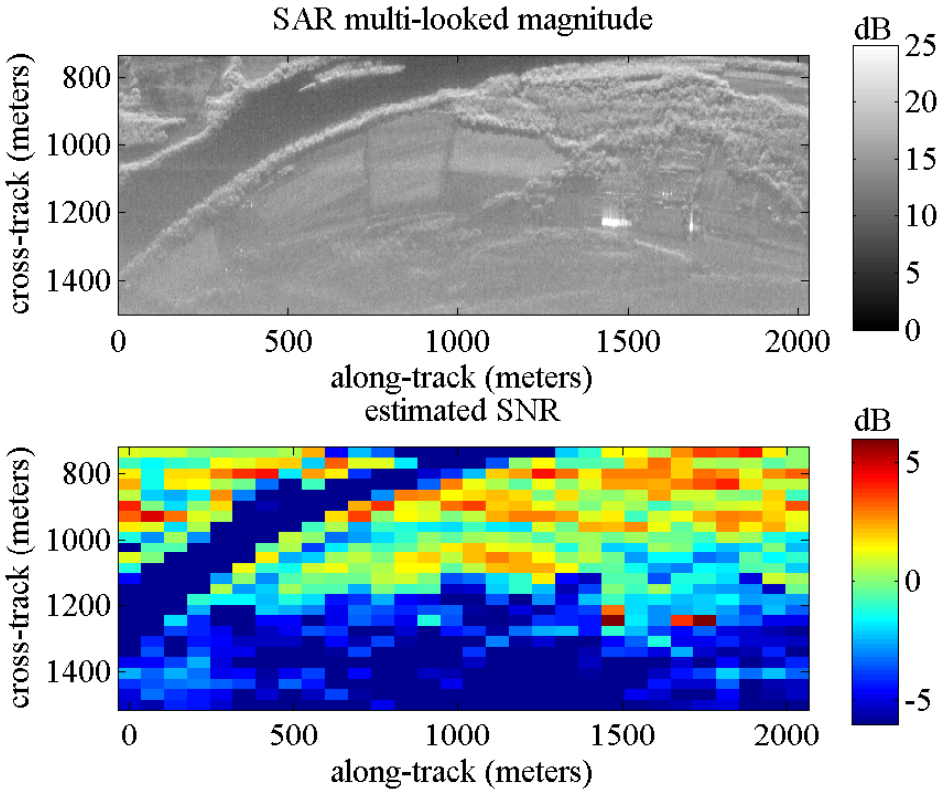

Figure A.6: An example of estimated SNR compared with the multi-looked SAR image.

$$\begin{aligned} \gamma_{vol} &= \frac{\gamma_{tot}}{\gamma_{th} + \Delta_\gamma} \\ &\approx \frac{\gamma_{tot}}{\gamma_{th}} \left(1 - \frac{\Delta_\gamma}{\gamma_{th}} + (\frac{\Delta_\gamma}{\gamma_{th}})^2 \right), \end{aligned} \tag{A.3}$$

where Δ_γ is the error in the estimated thermal correlation. For the scatterers whose thermal noise decorrelation, γ_{th}, is small, the error term in the bracket, $\Delta_\gamma/\gamma_{th}$ and its square could be significant. Hence the pixels with a low SNR, most of the masked pixels are from water region, shadows and far-range pixels, in the top image of Figure A.8 is masked to remove the effect of having a large uncertainty. Compared to the optical image from Google Earth in Figure A.9, it can be seen that volume decorrelation occurs mostly in vegetated regions with trees and crops.

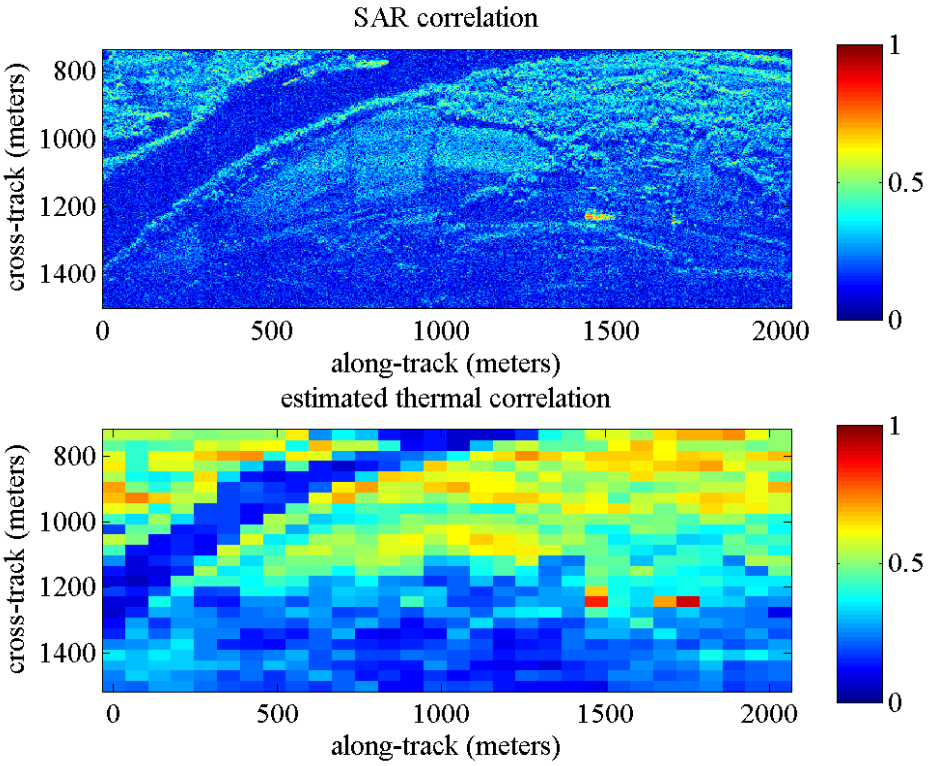

Figure A.7: The estimated thermal correlation corresponding to the estimated SNR in Figure A.6.

A.1.2 Platform Motion

As shown in [25], the effects of trajectory deviation is an aliasing of the complex SAR image along the azimuth dimension. The complex value of each pixel is the result of the sum of adjacent pixels, as shown in

$$\begin{aligned} z'_{1i} &= \sum_{k=-N}^{N} \alpha_k z_{1(i+k)} \\ z'_{2i} &= \sum_{k=-N}^{N} \alpha_l z_{2(i+k)}, \end{aligned} \tag{A.4}$$

where, z' represents the complex pixel values of channel 1 and 2 with the effect of aliasing, z represents the original complex pixel values without any aliasing, and N is the total number of aliased adjacent pixels in one direction. The real-valued

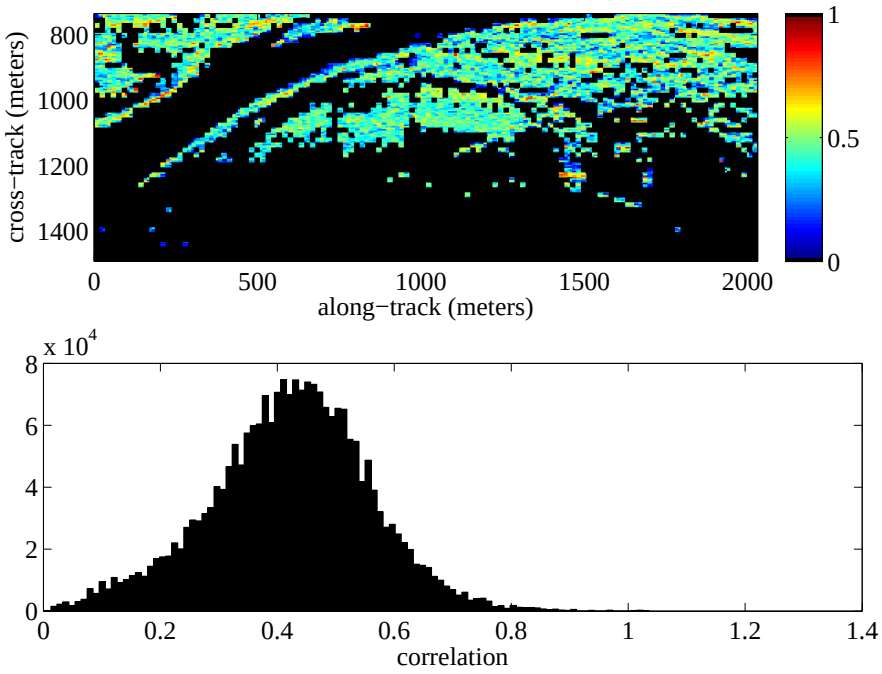

Figure A.8: (Top) The derived volume decorrelation from the total decorrelation and the calculated thermal decorrelation. The area where the SNR lower than 1 is set to black since the error is large in this region. (Bottom) The histogram of derived volume decorrelation.

Figure A.9: The Google earth image shows the different types of terrain.

coefficient, α_k, is 1 when $k = 0$, and is less than 1 otherwise. Hence the correlation between the two channels becomes

$$
\begin{aligned}
z'_{1i} z'^{*}_{2i} &= \left(\sum_{k=-N}^{N} \alpha_k z_{1(i+k)} \right) \left(\sum_{l=-N}^{N} \alpha_l z_{2(i+l)} \right)^{*} \\
&= \sum_{k=-N}^{N} \sum_{l=-N}^{N} \alpha_k \alpha_l z_{1(i+k)} z^{*}_{2(i+l)} \\
&= \sum_{k=-N}^{N} |\alpha_k|^2 z_{1(i+k)} z^{*}_{2(i+k)} + \sum_{k=-N}^{N} \sum_{\substack{l=-N \\ k \neq l}}^{N} \alpha_k \alpha_l z_{1(i+k)} z^{*}_{2(i+l)}.
\end{aligned}
\tag{A.5}
$$

It can be seen from (A.5) that the correlation affected by an aliasing is a sum of correlations of adjacent pixels between channel 1 and channel 2. A diagram illustrating the correlation for the case $N = 1$ in shown in Figure A.10. The correlation can be decomposed into two parts, one is the sum of correlations between corresponding pixels from each channel, another is the sum of inter-correlations. For a stationary

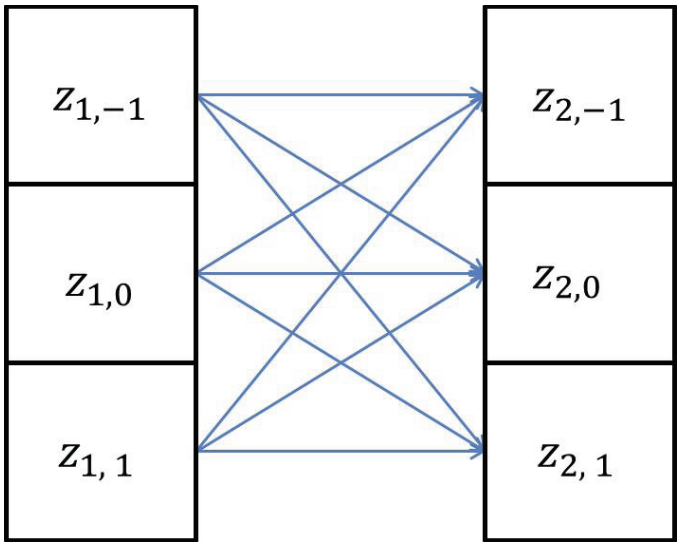

Figure A.10: A diagram illustrates the correlation with aliasing.

scene, the terms in the first sum in (A.5) will be in phase. The inter-correlation terms in the second sum appear in pairs, as shown in

$$
\begin{aligned}
&\alpha_k\alpha_l z_{1(i+k)} z^*_{2(i+l)} + \alpha_l\alpha_k z_{1(i+l)} z^*_{2(i+k)} \\
=&\alpha_k\alpha_l \left(|z_{1(i+k)}||z_{2(i+l)}| e^{j(\phi_{1k}-\phi_{2l})} + |z_{1(i+l)}||z_{2(i+k)}| e^{j(\phi_{1l}-\phi_{2k})} \right) \\
=&\alpha_k\alpha_l \left(|z_{1(i+k)}||z_{2(i+l)}| e^{j(\phi_{1k}-\phi_{1l}+\Delta\Phi_l)} + |z_{1(i+l)}||z_{2(i+k)}| e^{j(\phi_{1l}-\phi_{1k}+\Delta\Phi_k)} \right),
\end{aligned}
\tag{A.6}
$$

where $\Delta\Phi_k$ and $\Delta\Phi_l$ are the interferometric phase of the k^{th} and l^{th} pixels. They are independent random variables but have the same probability density function according to the stationary scene assumption. The sum in Equation A.6 is a complex random variable, and its mean is in phase with the first sum. This can be derived from the probability density function of the interferometric phase given by (6.7). Since the pdf of the $\Delta\Phi_k$ and $\Delta\Phi_l$ with the true phase $\phi_\gamma = 0$ is an even function, the expectation of $e^{j\Phi_k}$, which is the Fourier transform of their pdf, is a real number, as in

$$
\begin{aligned}
< e^{j\Phi_k} > \Big|_{\phi_\gamma=0} &= \int e^{j\phi_k} f_{\Phi_k}(\phi_k) d\phi_k \\
&= \mathcal{F}[f_{\Phi_k}(\phi_k)]\Big|_{\omega_1}.
\end{aligned}
\tag{A.7}
$$

Hence when the pdf is not centered at $\phi_\gamma = 0$, the result in (A.7) will be phase shifted, as in

$$
\begin{aligned}
< e^{j\Phi_k} > \Big|_{\phi_\gamma\neq 0} &= \int e^{j\phi_k} f_{\Phi_k}(\phi_k) d\phi_k \\
&= \mathcal{F}[f_{\Phi_k}(\phi_k)]\Big|_{\omega_1} e^{j\phi_\gamma} = b e^{j\phi_\gamma}.
\end{aligned}
\tag{A.8}
$$

Then the expectation of the pair in (A.6) can be derived, as given by

$$
\begin{aligned}
&< \alpha_k\alpha_l z_{1(i+k)} z^*_{2(i+l)} + \alpha_l\alpha_k z_{1(i+l)} z^*_{2(i+k)} > \\
=&\alpha_k\alpha_l (< |z_{1(i+k)}| >< |z_{2(i+l)}| >< e^{j(\phi_{1k}-\phi_{1l}+\Delta\Phi_l)} > \\
&+ < |z_{1(i+l)}| >< |z_{2(i+k)}| >< e^{j(\phi_{1l}-\phi_{1k}+\Delta\Phi_k)} >) \\
=&2\alpha_k\alpha_l\, \sigma^2\, b \cos(\phi_{1k}-\phi_{1l}) e^{j\phi_\gamma}.
\end{aligned}
\tag{A.9}
$$

It indicates by (A.9) that the inter-correlation will not bias the interferometric phase. When estimating the correlation, many adjacent pixels are added up as in

$$\begin{aligned}\hat{\gamma} &= \frac{\sum_i z_{1i}^{'} z_{2i}^{'*}}{\sqrt{\sum |z_{1i}^{'}|^2 \sum |z_{2i}^{'}|^2}} \\ &= \frac{\sum_i \left(\sum_{k=-N}^{N} |\alpha_k|^2 z_{1(i+k)} z_{2(i+k)}^{*} + \sum_{k=-N}^{N} \sum_{\substack{l=-N \\ k \neq l}}^{N} \alpha_k \alpha_l z_{1(i+k)} z_{2(i+l)}^{*} \right)}{\sqrt{\sum |z_{1i}^{'}|^2 \sum |z_{2i}^{'}|^2}} \\ &\approx \frac{\sum_i a_i z_{1i} z_{2i}^{*} + \sum_i \sum_{\substack{j \\ i \neq j}} b_{ij} z_{1i} z_{2j}^{*}}{\sqrt{\sum |z_{1i}^{'}|^2 \sum |z_{2i}^{'}|^2}},\end{aligned} \tag{A.10}$$

where the prime sign of $z_{1i}^{'}$ and $z_{2i}^{'}$ means the complex value with aliasing. The last line is obtained by combing the terms, and the approximation is for those boundary pixels.

When the scene is not stationary, the sum of the inter-correlations will have a bias effect on the overall correlation. The amount of bias depends on the terrain topography.

A.2 Considerations in Radar System Design

To get an accurate measurement of the terrain topography with a certain spatial resolution and coverage, it is not only important to refine the processing algorithms, but also important to design the InSAR system carefully. Given the specifications of the outputs, the sets of system design variables can be derived, as shown in the diagram in Figure A.11. The most challenge to the processing procedure comes from the platform motion, the ability of the motion compensation routine determines the requirements of the Inertial Measurement Unit. Beyond that, all the efforts have to be put into the InSAR system design.

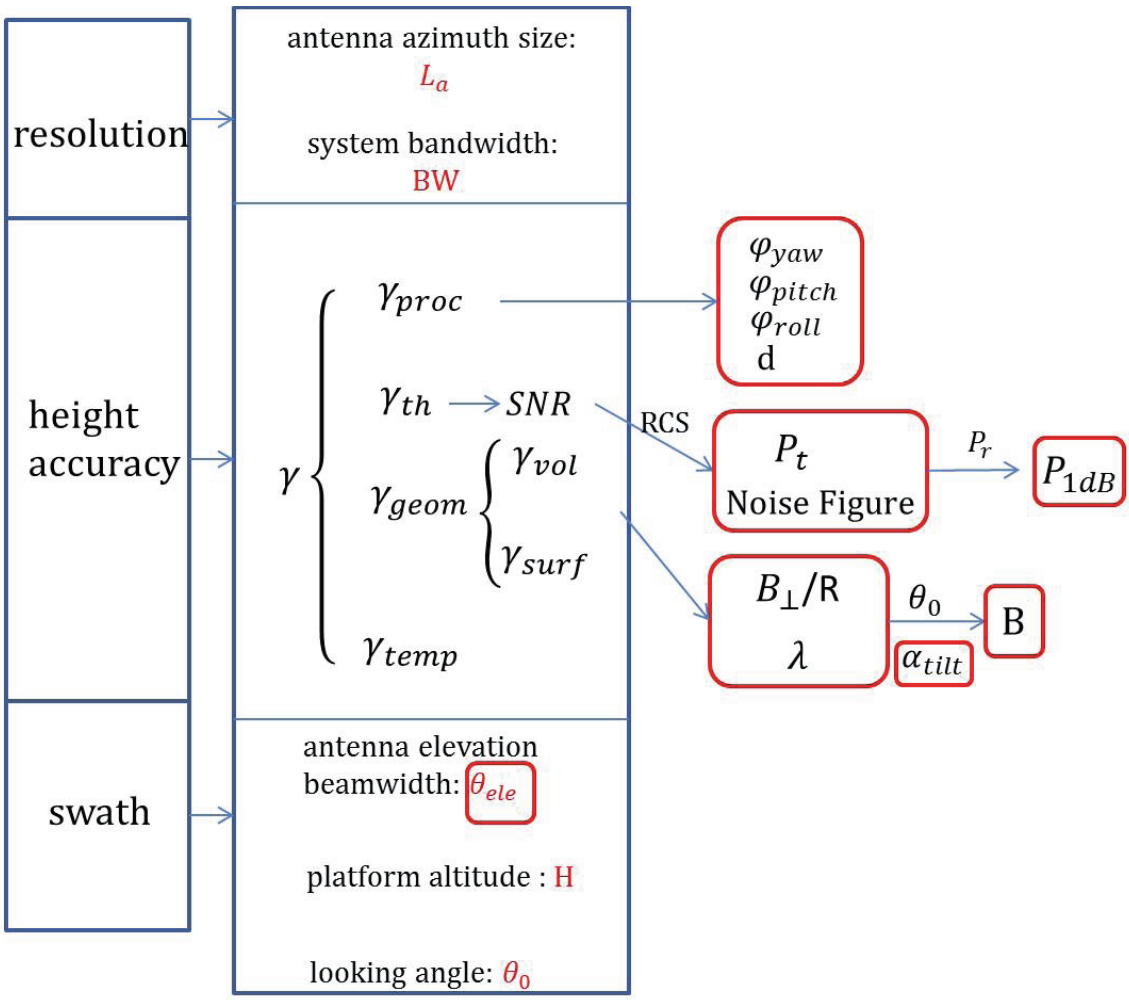

Figure A.11: A diagram illustrates the InSAR system design considerations.

BIBLIOGRAPHY

[1] F. M. Henderson, A. J. Lewis, *et al.*, *Principles and applications of imaging radar. Manual of remote sensing, volume 2.* John Wiley and sons, 1998.

[2] A. Sardar, "The evolution of space-borne imaging radar systems: a chronological history," *Canadian journal of remote sensing*, vol. 23, no. 3, pp. 276–280, 1997.

[3] H. J. Zwally, R. A. Bindschadler, A. C. Brenner, J. A. Major, and J. G. Marsh, "Growth of greenland ice sheet: Measurement," *Science*, vol. 246, no. 4937, pp. 1587–1589, 1989.

[4] C. M. Birkett, "Contribution of the topex nasa radar altimeter to the global monitoring of large rivers and wetlands," *Water Resources Research*, vol. 34, no. 5, pp. 1223–1239, 1998.

[5] P. R. Wolf and B. A. Dewitt, *Elements of Photogrammetry: with applications in GIS*, vol. 3. McGraw-Hill New York, 2000.

[6] D. Massonnet and K. L. Feigl, "Radar interferometry and its application to changes in the earth's surface," *Reviews of geophysics*, vol. 36, no. 4, pp. 441–500, 1998.

[7] P. A. Rosen, S. Hensley, I. R. Joughin, F. K. Li, S. N. Madsen, E. Rodriguez, and R. M. Goldstein, "Synthetic aperture radar interferometry," *Proceedings of the IEEE*, vol. 88, no. 3, pp. 333–382, 2000.

[8] W. M. Brown and L. J. Porcello, "An introduction to synthetic-aperture radar," *Spectrum, IEEE*, vol. 6, no. 9, pp. 52–62, 1969.

[9] G. Born, J. Dunne, and D. Lame, "Seasat mission overview," *Science*, vol. 204, no. 4400, pp. 1405–1406, 1979.

[10] J. F. Vesecky and R. H. Stewart, "The observation of ocean surface phenomena using imagery from the seasat synthetic aperture radar: An assessment," *Journal of Geophysical Research: Oceans*, vol. 87, no. C5, pp. 3397–3430, 1982.

[11] "Synthetic aperture radar (sar) satellites." `https://www.unavco.org/instrumentation/geophysical/imaging/sar-satellites/sar-satellites.html`.

[12] L. C. Graham, "Synthetic interferometer radar for topographic mapping," *Proceedings of the IEEE*, vol. 62, no. 6, pp. 763–768, 1974.

[13] C. Magnard, E. Meier, D. Small, H. Essen, and T. Brehm, "Processing of memphis millimeter wave multi-baseline insar data," in *Geoscience and Remote Sensing Symposium (IGARSS), 2010 IEEE International*, pp. 4302–4305, IEEE, 2010.

[14] X. Wu, S. Hensley, E. Rodriguez, D. Moller, R. Muellerschoen, and T. Michel, "Near nadir ka-band sar interferometry: Swot airborne experiment," in *Geoscience and Remote Sensing Symposium (IGARSS), 2011 IEEE International*, pp. 2681–2684, IEEE, 2011.

[15] R. Fjortoft, J.-M. Gaudin, N. Pourthie, J.-C. Lalaurie, A. Mallet, J.-F. Nouvel, J. Martinot-Lagarde, H. Oriot, P. Borderies, C. Ruiz, *et al.*, "Karin on swot: Characteristics of near-nadir ka-band interferometric sar imagery," *Geoscience and Remote Sensing, IEEE Transactions on*, vol. 52, no. 4, pp. 2172–2185, 2014.

[16] "Mission science." `http://swot.jpl.nasa.gov/science/technology/`.

[17] M. A. Richards, J. Scheer, and W. A. Holm, *Principles of modern radar: basic principles*. SciTech Pub., 2010.

[18] A. Meta, P. Hoogeboom, and L. P. Ligthart, "Signal processing for fmcw sar," *Geoscience and Remote Sensing, IEEE Transactions on*, vol. 45, no. 11, pp. 3519–3532, 2007.

[19] H. K. Vedantham, "Design and development of a ka-band interferometer for cryospheric applications," *Masters Theses*, p. 220, 2009.

[20] R. B. Schrock, "Integration and measurements of a ka-band interferometric radar in an airborne platform," 2013.

[21] P. Siqueira, M. Tope, H. Vedantham, E. Insanic, and K. Srinivasan, "The design and characterization of a ku-and ka-band downconverter for spaceborne interferometric radar," in *NASA Earth Science Technology Conference, College Park, MD*, 2008.

[22] I. G. Cumming, F. H. Wong, U. of British Columbia, and M. Dettwiler, *Digital signal processing of synthetic aperture radar data: algorithms and implementation*. Artech House Norwood, 2004.

[23] D. Wahl, P. Eichel, D. Ghiglia, and C. Jakowatz Jr, "Phase gradient autofocus-a robust tool for high resolution sar phase correction," *Aerospace and Electronic Systems, IEEE Transactions on*, vol. 30, no. 3, pp. 827–835, 1994.

[24] A. Papoulis, *Signal analysis*, vol. 191. McGraw-Hill, 1978.

[25] G. Fornaro, "Trajectory deviations in airborne sar: analysis and compensation," *Aerospace and Electronic Systems, IEEE Transactions on*, vol. 35, no. 3, pp. 997–1009, 1999.

[26] G. Fornaro, G. Franceschetti, and S. Perna, "Motion compensation errors: effects on the accuracy of airborne sar images," *Aerospace and Electronic Systems, IEEE Transactions on*, vol. 41, no. 4, pp. 1338–1352, 2005.

[27] J. R. Moreira, "A new method of aircraft motion error extraction from radar raw data for real time motion," *IEEE Transactions on Geoscience and Remote Sensing*, vol. 28, no. 4, p. 620, 1990.

[28] T. Isernia, V. Pascazio, R. Pierri, and G. Schirinzi, "Synthetic aperture radar imaging from phase-corrupted data," in *Radar, Sonar and Navigation, IEE Proceedings-*, vol. 143, pp. 268–274, IET, 1996.

[29] K. A. de Macedo, C. Wimmer, and J. R. Moreira, "Highly accurate and precise airborne single-pass interferometry for DEM generation over challenging terrain," in *2014 IEEE Geoscience and Remote Sensing Symposium*, pp. 394–397, IEEE, 2014.

[30] E. C. Zaugg and D. G. Long, "Theory and application of motion compensation for lfm-cw sar," *Geoscience and Remote Sensing, IEEE Transactions on*, vol. 46, no. 10, pp. 2990–2998, 2008.

[31] W. M. Brown, "Synthetic aperture radar," *Aerospace and Electronic Systems, IEEE Transactions on*, no. 2, pp. 217–229, 1967.

[32] J. Mims and J. Farrell, "Synthetic aperture imaging with maneuvers," *Aerospace and Electronic Systems, IEEE Transactions on*, no. 4, pp. 410–418, 1972.

[33] A. Moreira and Y. Huang, "Airborne sar processing of highly squinted data using a chirp scaling approach with integrated motion compensation," *Geoscience and Remote Sensing, IEEE Transactions on*, vol. 32, no. 5, pp. 1029–1040, 1994.

[34] R. Scheiber and V. Bothale, "Interferometric multi-look techniques for sar data," in *Geoscience and Remote Sensing Symposium, 2002. IGARSS'02. 2002 IEEE International*, vol. 1, pp. 173–175, IEEE, 2002.

[35] X. Zheng, W. Yu, and Z. Li, "A novel algorithm for wide beam sar motion compensation based on frequency division," in *2006 IEEE International Symposium on Geoscience and Remote Sensing*, 2006.

[36] P. Prats, A. Reigber, and J. J. Mallorqui, "Topography-dependent motion compensation for repeat-pass interferometric sar systems," *Geoscience and Remote Sensing Letters, IEEE*, vol. 2, no. 2, pp. 206–210, 2005.

[37] K. C. de Macedo and R. Scheiber, "Precise topography-and aperture-dependent motion compensation for airborne sar," *Geoscience and Remote Sensing Letters, IEEE*, vol. 2, no. 2, pp. 172–176, 2005.

[38] A. Potsis, A. Reigber, J. Mittermayer, A. Moreira, and N. Uzunoglou, "Sub-aperture algorithm for motion compensation improvement in wide-beam sar data processing," *Electronics Letters*, vol. 37, no. 23, pp. 1405–1407, 2001.

[39] S. Buckreuss, "Motion errors in an airborne synthetic aperture radar system," *European Transactions on Telecommunications*, vol. 2, no. 6, pp. 655–664, 1991.

[40] R. Touzi, A. Lopes, J. Bruniquel, and P. W. Vachon, "Coherence estimation for sar imagery," *Geoscience and Remote Sensing, IEEE Transactions on*, vol. 37, no. 1, pp. 135–149, 1999.

[41] J. Lee, K. Hoppel, S. Mango, and A. Miller, "Intensity and phase statistics of multi-look polarimetric sar imagery," in *Geoscience and Remote Sensing Symposium, 1993. IGARSS'93. Better Understanding of Earth Environment., International*, pp. 813–816, IEEE, 1993.

[42] T. G. Farr, P. A. Rosen, E. Caro, R. Crippen, R. Duren, S. Hensley, M. Kobrick, M. Paller, E. Rodriguez, L. Roth, *et al.*, "The shuttle radar topography mission," *Reviews of geophysics*, vol. 45, no. 2, 2007.

[43] "Office of geographic information." `http://www.mass.gov/anf/research-and-tech/it-serv-and-support/application-serv/office-of-geographic-information-massgis/`.

[44] H. A. Zebker and J. Villasenor, "Decorrelation in interferometric radar echoes," *Geoscience and Remote Sensing, IEEE Transactions on*, vol. 30, no. 5, pp. 950–959, 1992.